A Numerical Simulation Study for the Effect of Static and Rotating Magnetic Fields in Liquid Phase Diffusion Growth of Si_xGe_{1-x} Single Crystals

by

Emine Yildiz

B.Eng., Yildiz Technical University, 2000

A Thesis Submitted in Partial Fulfillment of the
Requirements for the Degree of

MASTER OF APPLIED SCIENCE

in the Department of Mechanical Engineering

A Numerical Simulation Study for the Effect of Static and Rotating Magnetic Fields in Liquid Phase Diffusion Growth of Si_xGe_{1-x} Single Crystals

by

Emine Yildiz

B.Eng., Yildiz Technical University, 2000

Supervisory Committee

Dr. Sadik Dost (Department of Mechanical Engineering)

Supervisor

Dr. Afzal Suleman (Department of Mechanical Engineering)

Departmental Member

Dr. Matthew Moffitt (Department of Chemistry)

Outside Member

Supervisory Committee

Dr. Sadik Dost (Department of Mechanical Engineering)

Supervisor

Dr. Afzal Suleman (Department of Mechanical Engineering)

Departmental Member

Dr. Matthew Moffitt (Department of Chemistry)

Outside Member

ABSTRACT

High quality semiconductor single crystals are the driving force behind today's rapidly growing electronic and communication industry. However, the growth of desired high quality crystals is difficult mainly due to the generation of defects and impurities in the grown crystal, and the segregation of species and strong convection in the liquid solution during growth. To minimize these undesirable effects, and to control segregation and convection, the use of magnetic fields (stationary, rotating, or traveling) has been widely considered. Static magnetic fields have been used to improve the quality of crystals by suppressing convection (Natural and/or Marangoni) and controlling the directional solidification and segregation of species. Rotating magnetic fields (RMF), on the other hand, have been used to obtain better mixing in the melt, better control for the heat and mass transport characteristics of the system and also for the shape of the growth interface.

The objective of this thesis is to investigate the feasibility of using applied static vertical and rotating magnetic fields in Liquid Phase Diffusion (LPD) growth of Si_xGe_{1-x} single crystals. To this end, a three-dimensional numerical simulation model was developed to study the heat, mass and momentum transfer characteristics of the *Si-Ge* solution under

magnetic fields. The governing equations describing the fluid flow, heat and mass transport are solved numerically using the finite volume-based CFX software package of AEA Technology. In the simulation model, several complex user-defined subroutines have been developed to move the grid, to solve the scalar electric-charge balance equation for the electric potential distribution, and to include the magnetic body force terms. In addition, a command file is produced to define the physical properties of the solution and surrounding solids, and the numerical methods used, model topology, convergence criteria, and equation solvers.

The results obtained from this study reveal that the use of a static vertical magnetic field is effective in suppressing natural convection. A magnetic field intensity of 0.3 Tesla is sufficient to provide significant suppression in the liquid *Si-Ge* solution. However, the static magnetic field does not provide the expected improvement on the growth interface shape. The use of RMF is, on the other hand, effective in creating a good mixing in the solution leading to more homogenous *Si-Ge* liquid. In addition, RMF is also very beneficial for creating a radially uniform solute distribution, thus flattening the growth interface for a stable growth.

TABLE OF CONTENTS

LIST OF FIGURES

LIST OF TABLES

NOMENCLATURE

Symbol	Description	Units
$\mathbf{B}$	Magnetic field vector	Tesla
B	Absolute value of magnetic induction	Tesla
c_o	Reference mass fraction of solute	kg/kg
c_1	Mass fraction of solute	kg/kg
c_{di}^{L}	Mass fraction of silicon in liquid phase on the dissolution interface	kg/kg
c_{eq}^{L}	Equilibrium mass fraction of silicon in liquid phase	kg/kg
c_{eq}^{S}	Equilibrium mass fraction of silicon in solid phase	kg/kg
c_{gi}^{L}	Mass fraction of silicon in liquid phase at the growth interface	kg/kg
c_{gi}^{S}	Mass fraction of silicon in solid phase at the growth interface	kg/kg
$\Delta c = c_1 - c_o$	Characteristic concentration	kg/kg
$D_{L,Si}$	Diffusion coefficient of silicon in the liquid solution	m^2/s
$\mathbf{E}$	Electric field vector	Volt/m
$\mathbf{f}_{st}^{M}$	Magnetic body force (Lorentz force) per unit volume due to a stationary magnetic field	N/m^3
$f_{st,r}^{M}$	Magnetic body force component for the stationary magnetic field in radial direction	N/m^3
$f_{st,\varphi}^{M}$	Magnetic body force component for the stationary magnetic field in azimuthal direction	N/m^3

$\mathbf{f}_{rot}^{M}$	Magnetic body force per unit volume due to a rotating magnetic field	N/m^3
$f_{rot,r}^{M}$	Magnetic body force component for the rotating magnetic field in radial direction	N/m^3
$f_{rot,\varphi}^{M}$	Magnetic body force component for the rotating magnetic field in azimuthal direction	N/m^3
$f_{rot,z}^{M}$	Magnetic body force component for the rotating magnetic field in axial direction	N/m^3
g	Gravity	m/s^2
h	Modified heat transfer coefficient	$J/m^2.s.K$
$\mathbf{j}$	Current density	A/m^2
k_L	Thermal conductivity of the liquid phase	W/m.K
k_S	Thermal conductivity of the solid phase	W/m.K
l_o	Characteristic length (radius of growth zone)	m
n	Unit normal direction	
p	Pressure	N/m^2
r	Radial coordinate direction	m
z	Axial coordinate direction	m
T_o	Reference temperature	K
T_1	Reference temperature	K
T	Absolute temperature	K
T_L	Temperature of the liquid at the growth interface	K
T_S	Temperature of the solid at the growth interface	K
$\Delta T = T_1 - T_o$	Characteristic temperature	K
$T_f(z)$	Ambient temperature inside the furnace	K
u_g	Growth velocity	m/s
$\mathbf{v}=(v_r, v_\varphi, v_z)$	Velocity vector and its components in the cylindrical coordinate	m/s

$x_{(i)}\,(i = r, \varphi, z)$	Position vector	m
a_L, b_L, c_L, d_L	Phase diagram constants in the liquid phase	$1/K^3, 1/K^2, 1/K$
a_S, b_S	Phase diagram constant in the solid phase	K, K
Greek		
β_C	Solutal expansion coefficient	1/wt.Si%
β_T	Thermal expansion coefficient	1/K
ϕ	Scalar electric potential for the vertical magnetic field	Volt
Φ_1, Φ_2	Scalar electric potential components for the rotating magnetic field	Volt
γ_L	Specific heat for the liquid phase	J/kg.K
γ_S	Specific heat for the solid phase	J/kg.K
η	Magnetic diffusivity	m^2/s
φ	Azimuthal coordinate direction	------
κ	Thermal diffusivity	m^2/s
μ	Viscosity	kg/m.s
μ_o	Magnetic permeability of the vacuum	N/A^2
ρ_L	Density of liquid phases	kg/m^3
ρ_S	Density of solid phases	kg/m^3
σ_L	Electrical conductivity of the liquid solution	$1/\Omega.m$
υ	Kinematic viscosity of the liquid solution	m^2/s
ω_B	Angular frequency of the rotating magnetic field	1/s
Dimensionless numbers		
Gr_T	Thermal Grashof Number	
Gr_c	Solutal Grashof Number	
Ha	Hartmann number	
Pr	Prandtl Number	

Ra_T	Thermal Rayleigh Number
Re_m	Magnetic Reynolds Number
Re_ω	Rotating Reynolds Number
Sc	Schmidt Number
Ta_m	Magnetic Taylor Number

ACKNOWLEDGEMENT

I would like to take this opportunity to express my appreciation to those who helped me complete this thesis.

First of all, I owe many thanks to my supervisor, Dr. Sadik Dost for his guidance, advice and encouragement. His constant support made this work possible.

I would like to thank all my professors, colleagues and friends especially Mrs. Sema Dost in the department of mechanical engineering, University of Victoria, for the encouragement and friendship during the period of my study.

Most of all, I would like to thank my beloved husband and son who have been a great support and inspiration for me. Without the love, motivation and patience they provided for me, I would not be able to complete this thesis.

Special thanks to my parents, brothers and the sister for their constant support during my study.

DEDICATION

Dedicated to my parents, my husband Mehmet Yildiz and my son Emir Berk

CHAPTER 1

INTRODUCTION

1.1 Motivation

SiGe is one of the most important semiconductor materials with many potential applications in the electronics and communication industry. Because of *SiGe*'s low-manufacturing cost and adjustable electronic properties, it has become the material of choice for optoelectronic and microelectronic devices such as integrated circuits, low-power radio-frequency (RF) chips, heterojunction bipolar transistors (HBT), solar cells, and photo detectors [1,2,3]. Different growth techniques such as Molecular Beam Epitaxy (MBE), Chemical Vapor Deposition, and Liquid Phase Epitaxy (LPE) have been used in the production of *SiGe* single crystals for the above mentioned applications; however, in general, these techniques produce crystals in the form of thin films grown on a silicon substrate. Since the lattice parameter of the silicon substrate is smaller than that of the *SiGe* alloy and pure germanium, misfit dislocations are produced in the grown crystals [4, 5, 6]. Such defects affect the quality of crystals significantly. Therefore, the use of *SiGe* as a seed (substrate) can be considered as a solution for the lattice mismatch problem.

In this direction, Liquid Phase Diffusion (LPD) growth technique was utilized and a number of Si_xGe_{1-x} crystals have been grown for the purpose of producing seed (substrate) crystals with the desired compositions [7]. However, the previous numerical study on the LPD growth of Si_xGe_{1-x} revealed that during the initial stage of the growth process a strong natural convection develops in the liquid solution [7]. This was due to the radial thermal gradients existing in the system. An uncontrolled convection in the

solution may give rise to non-uniform transport of species towards the growth interface. This in turn results in local variations in the growth velocity, leading to non-uniform growth and also possibly low angle grain boundaries or polycrystalline structures in the grown crystals. In addition, due to the thermal characteristic of the LPD growth system, the initially obtained growth interface is reported to be concave (to the liquid) [8]. In crystal growth, a flat or a slightly convex interface is generally desired to prevent inclusions in the grown single crystals.

In order to suppress convection and control fluid flow in crystal growth, one of the options is the use of a microgravity environment [9, 10, 11]. However, the use of such a platform is very expensive and such an opportunity is rarely available. A feasible option that is easily accessible and relatively inexpensive is the application of magnetic fields. Both static and rotating magnetic fields have been used widely in crystal growth to control convection and fluid flow. In this direction, this theoretical work was conducted to study the feasibility of using applied static vertical and rotating magnetic fields in the Liquid Phase Diffusion growth of $Si_x\ Ge_{1-x}$ single crystals.

1.2 Research Objectives

The main focus of this thesis is to investigate the feasibility of applied static vertical and rotating magnetic fields in the Liquid Phase Diffusion growth of Si_xGe_{1-x} single crystals. A further goal is to find the appropriate magnetic field type and intensity levels for the present LPD system.

1.3 Scope of Thesis

This thesis consists of seven chapters. The first chapter is devoted to the objectives and the motivation behind this work. The second chapter gives brief introduction on some of the crystal growth techniques, and presents the literature survey investigating the use of static and rotating magnetic fields in crystal growth. The LPD growth system and growth

mechanism are briefly introduced in Chapter 3. Chapter 4 focuses on the mathematical model developed for the LPD growth of $Si_x\ Ge_{1-x}$ single crystals under static vertical and rotating magnetic fields. Three-dimensional numerical model of the present system and the simulation results are given in Chapter 5 and Chapter 6, respectively. Concluding remarks are presented in Chapter 7.

CHAPTER 2

MAGNETOHYDRODYNAMICS CONTROL OF CRYSTAL GROWTH

Magnetohydrodynamics (MHD) is a branch of science that deals with the interaction of a magnetic field with an electrically conducting liquid. It is of importance in many engineering applications such as material processing and crystal growth. The use of MHD methods in metallurgy dates back to the 1930s and has been mainly for electromagnetic molding, stirring of alloys and controlling the melt flow in continuous casting of steel [12, 13]. However, the use of MHD in semiconductor crystal growth is only two decades old and still under investigation. It is used in crystal growth primarily for damping of different types of convections, and stirring the melt*. The purpose of using a static magnetic field is to suppress the thermosolutal convection occurring in the melt. A rotating magnetic field is applied to generate forced-convection, thereby homogenizing the growth melt. Both play a significant role on improving the growth process conditions and the quality of the grown crystals.

In this chapter, in order to provide the reader with some insight, we will briefly introduce some of the crystal growth techniques and then we will present a short summary of the studies in the literature related to the application of static and rotating magnetic fields.

---

* Note that throughout the thesis, the terms "solution", "melt", and "liquid" all refer to the growth liquid. The word "melt" is used to refer to "growth liquid" in the melt growth techniques while the term "solution" is used in solution growth techniques.

2.1 Crystal Growth Techniques

2.1.1 Vertical Bridgman Technique (VB)

Bridgman method (normal freezing) is a unidirectional solidification process. In this technique, the solidification direction can be vertical or horizontal. If the direction is vertical, the process is called vertical Bridgman. In this method, single crystals can be grown using seeded or unseeded ampoules. The growth process can be summarized as follows: the charge material is placed into the crucible or ampoule and sealed under a vacuum. Then, the charge material is melted. If the growth is unseeded, the crucible acts as a seed material and nucleation starts from the tip of the container. The growth can be achieved by either moving of the crucible in a static temperature field or moving a temperature field while keeping the crucible stationary. Figure 2.1 shows schematic representation of the VB system [14].

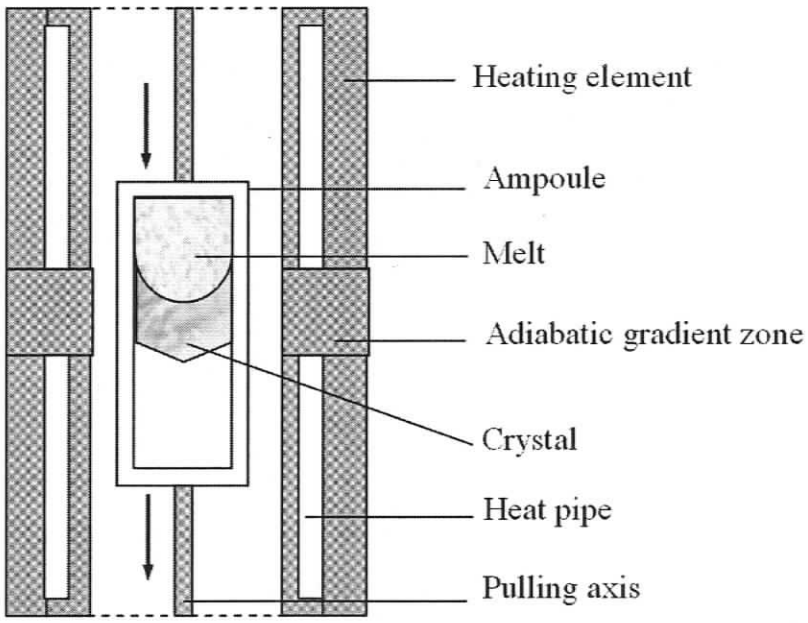

Figure 2. 1 - Schematic diagram of a VB furnace

The Vertical Bridgman technique is one of the most inexpensive growth methods. It is widely used in the growth of *SiGe* single crystals. For Vertical Bridgman growth, magnetic field application is of a great importance. Especially an axial magnetic field has been investigated both experimentally and numerically to minimize the buoyancy convection in the melt [15, 16, 17].

2.1.2 Crystal Pulling (Czochralski, Cz)

The crystal pulling process (known as Czochralski method) is the most common commercial crystal growth technique, and today more than 90% of the commercial crystals are grown by Cz. The size of the crystals grown by Cz has reached about 300mm in diameters and about one meter in length [18].

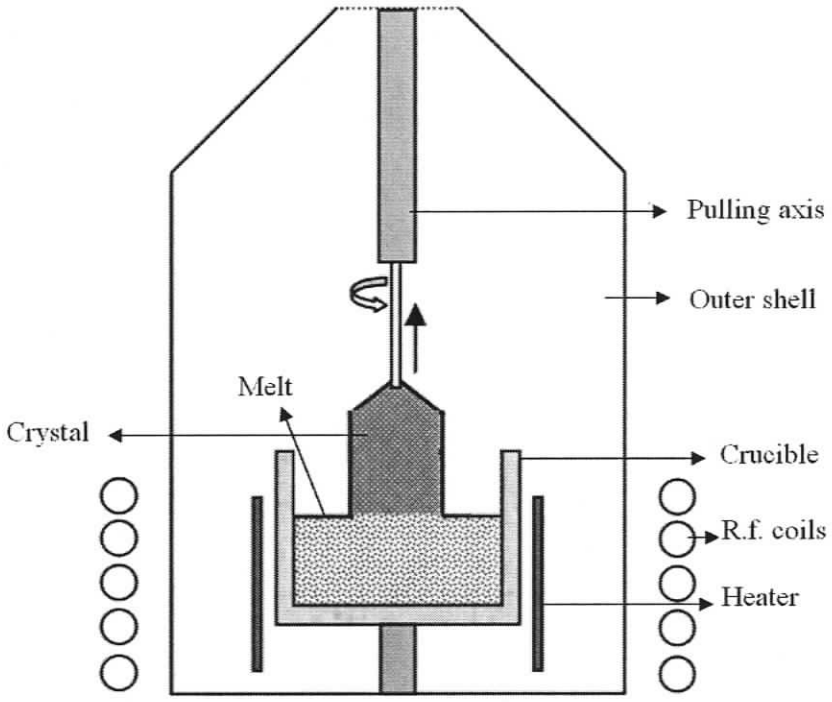

Figure 2. 2– A representative figure for Cz method

In this process, first, the charge material in a quartz crucible is heated to above melting temperature in an argon or Helium atmosphere. Either radio frequency (RF) or resistance heating is used during the process. A single crystal seed of the material to be grown is

partially dipped into the melt. Next, crystal growth process is initiated by pulling the seed slowly at a predetermined rate. As the seed is pulled from the melt, a layer of molten material drawn by the seed cools gradually and takes the same crystalline structure of the seed. The growth continues until attaining the desired length. Figure 2.2 represents the schematic diagram of a Cz growth system. Different types of magnetic fields such as vertical, rotating and cusp are used in Cz process to control the interface shape, melt convection and oxygen concentration [19, 20, 21].

2.1.3 Floating Zone Technique (FZ)

The Floating Zone (FZ) technique is used to grow single crystals of high purity and low dislocation for high power applications. Since it is a crucible free growth technique, dislocations, contaminations and structural defects due to a crucible are avoided. The FZ process requires a vacuum environment and delicate control to minimize the instabilities associated with thermocapillary and buoyancy convections. In addition, the size of the crystal to be grown is limited by the size of the liquid bridge between the seed and feed materials due to the effect of gravity. Therefore, in FZ, application of a magnetic field is almost essential to suppress the convection and to control heat and mass transport during growth. The principles of the FZ process are as follows: a polycrystalline feed material (in the form of rod) is set at the top of a seed crystal rod and lowered through an electromagnetic coil. The coil's magnetic field induces an electric field in the rod, heating and melting the interface between the rod and the seed. In this process, the rods are rotated in opposite directions to produce uniform mixing of in the melt. Single-crystal is formed at the interface, growing upward as the coils are slowly raised [22, 23, 24]. The Fz process is illustrated in Figure 2.3.

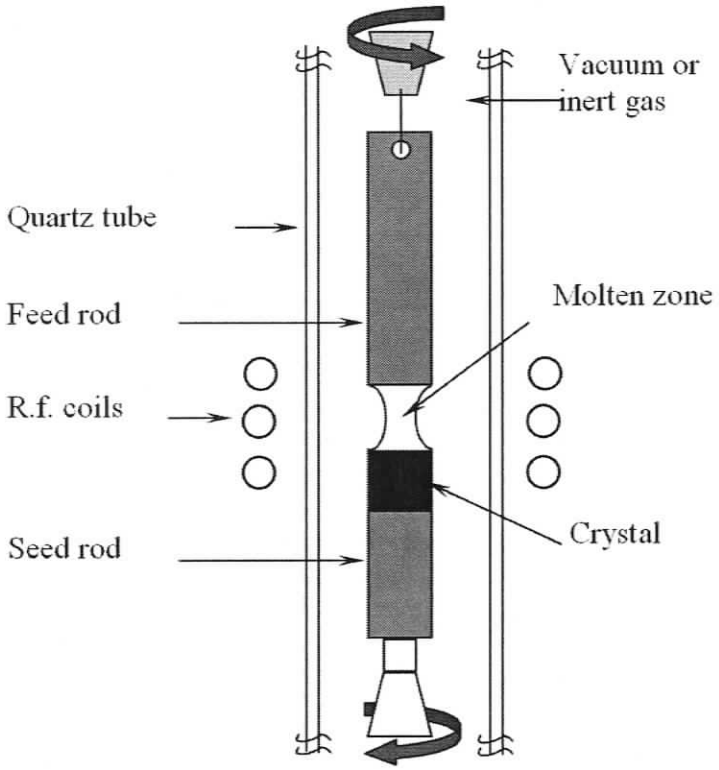

Figure 2. 3- A schematic representation of the floating zone process

2.1.4 Liquid Phase Epitaxy (LPE)

Liquid Phase Epitaxy is a solution growth technique and plays a very important role in the electronics industry since the crystalline layers grown by this method are generally pure, thus devices containing crystals grown by LPE have higher performance. There are several approaches used in Liquid Phase Epitaxy namely, tipping, dipping and sliding. Among those, the horizontal sliding is the most extensively used technique. The growth process of horizontal sliding is as follows: The growth solution (consisting of solvent and solute) and the substrate are located in the boat separately. Then, the furnace is heated to a growth temperature. As the solution is cooled very slowly, it becomes saturated at some temperature known as the liquidus temperature, T_L. On further cooling, the solution becomes supersaturated and the introduction of a seed crystal or substrate initiates

epitaxial growth. Figure 2.4 represents the sliding boat technique [25]. The vertical magnetic field is mostly used in LPE to suppress the buoyancy induced convection [26].

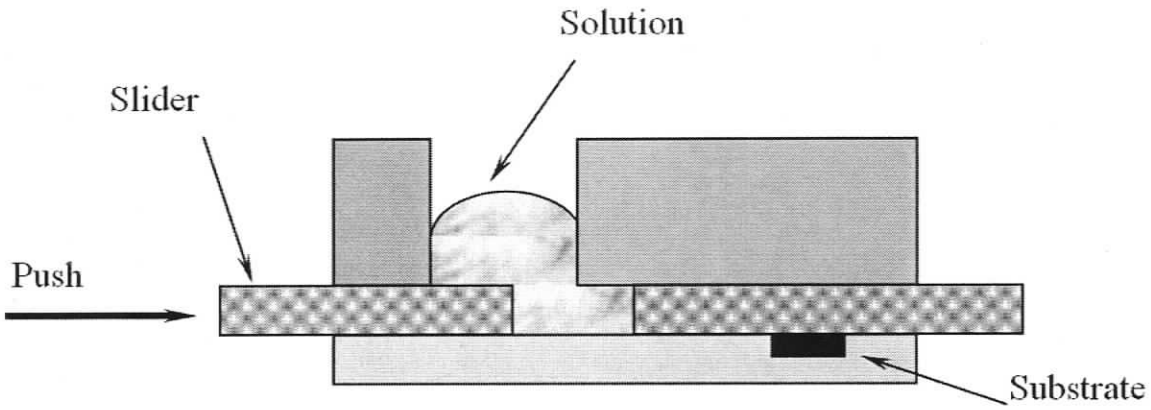

Figure 2. 4- A schematic representation of the LPE sliding boat technique

2.1.5 Liquid Phase Electro Epitaxy (LPEE)

LPEE is one of the recent crystal growth techniques used to produce uniform and low dislocation density epitaxial layers of III-V compounds semiconductors. This technique is performed by passing an electric current from the substrate-solution-source system while the temperature of the whole furnace is kept constant. In LPEE, the electric current initiates and maintains growth due to the Peltier effect at the solution- substrate interface and the electromigration in the solution. In this technique, the current also stabilizes the compositional fluctuations and homogenizes the composition distribution along the growth direction. Figure 2.5 represents the LPEE growth system. In LPEE, the higher electric current densities are used in order to reach higher growth rates which results in strong convection in the flow. Therefore, steady magnetic field is applied to the LPEE system to damp the convection thus obtain a stable growth [27, 28, 29].

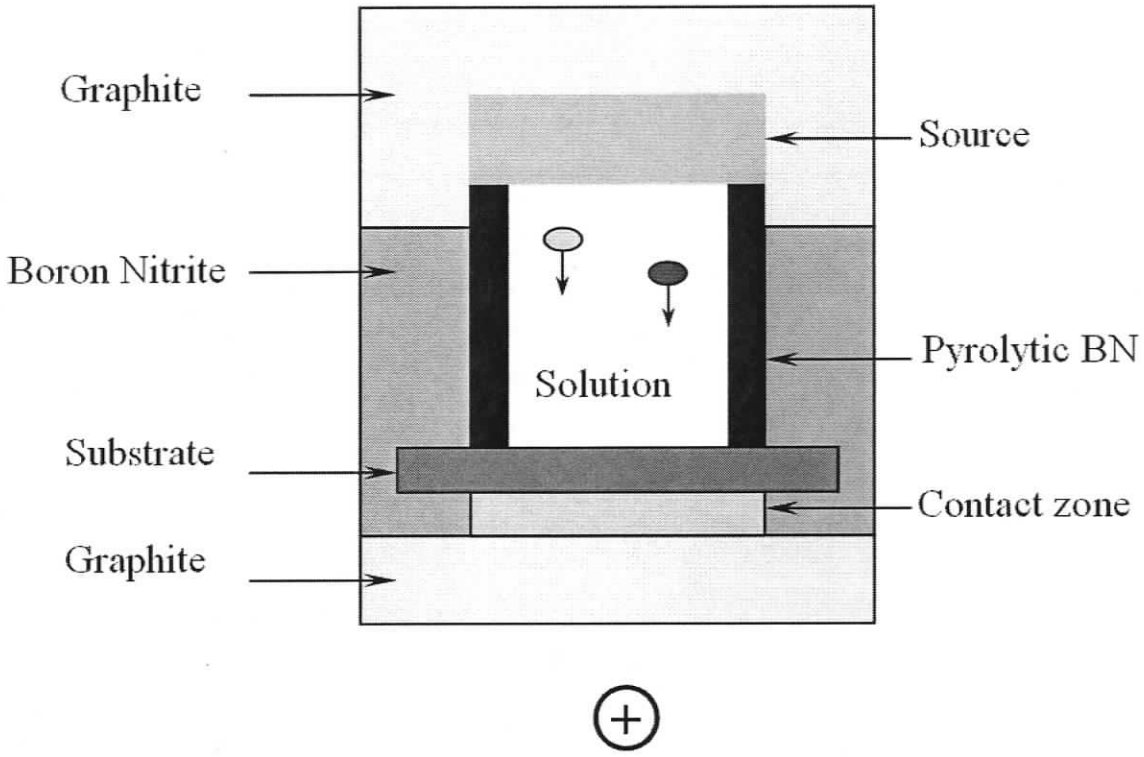

Figure 2. 5- A schematic representation of the LPEE growth system

2.1.6 Traveling Heater Method (THM)

Among the solution growth techniques, THM has the advantage of growing a large single crystal. In this technique, the growth process can be realized by moving either the heater while keeping the charge stationary or moving the charge material while the heater is kept still (see Figure 2. 6). With the THM technique, single and poly-crystals can be grown at a temperature far below their melting points due to the solvent used in the solution. Therefore, it has been applied to the growth of a wide range of materials such as silicon, *CdTe*, *GaP* and *ZnO*. In this method, however, the convective flow in the solution can be very strong due to the high temperature gradient used. Therefore, magnetic fields are used in THM to suppress the natural convection in the solution [30, 31, 32].

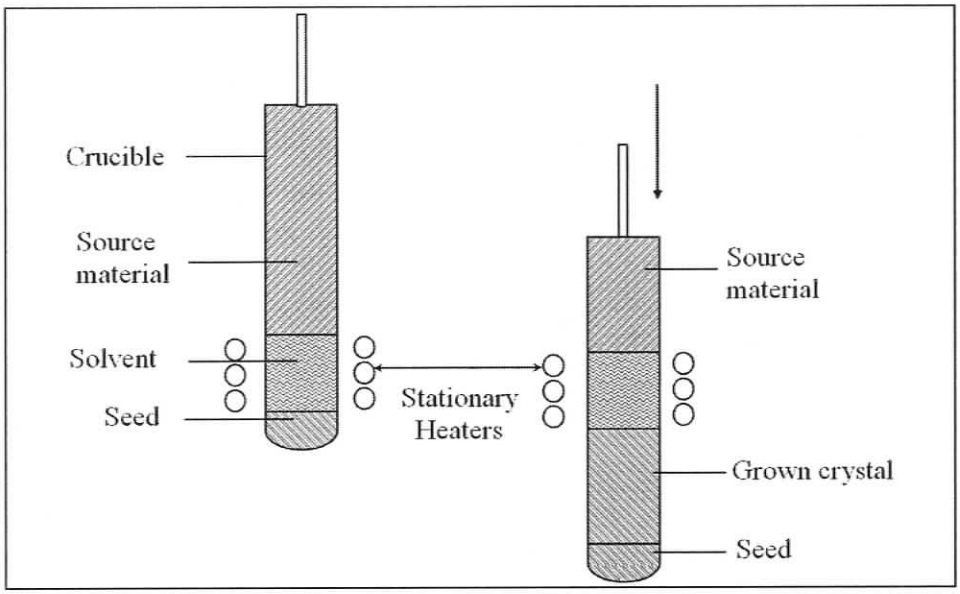

Figure 2. 6- A Representative figure for the THM method

2.2 Literature Review

2.2.1 Application of a Static Vertical Magnetic Field in Crystal Growth

The use of a static magnetic field has been an effective way to improve the quality of crystals by suppressing convection (Natural or Marangoni), thereby controlling the directional solidification and segregation of species in metallic liquids. Most metallic liquids are good electric conductors, and when a steady magnetic field interacts with the liquid, a Lorenz force acts on the moving species of the liquid. The components of this magnetic body force suppress the flow in the liquid. There are many numerical and experimental studies in which the application of static magnetic field is used effectively to stabilize both the flow and temperature fields in the liquid solution.

For instance, the Traveling Heater Method (THM) has been used by many crystal growers to grow binary and ternary semiconductors such as *GaAs, CdTe*, *CdZnTe* and *InGaSb*. However, high temperature gradients used in the THM result in strong convection in the solution which consequently affects the quality of the grown crystals.

A recent numerical investigation by *S. Dost et al.* [30] shows the effect of a static magnetic field on the growth of *CdTe* single crystals by the THM. The study revealed that the application of a magnetic field level of 0.8 Tesla suppresses convection significantly, while enhancing compositional non-uniformity in the solution.

Y. Wang et al. carried out an experimental study on the THM growth of *CdZnTe* crystals from a Te-solution under a static magnetic field. The *CdZnTe* crystals grown without magnetic field had a hill-like interface shape due to low thermal conductivity of the *CdTe* substrate. In their study, a static magnetic field with the induction of 3.0 Tesla was found to be beneficial to improve the growth interface shape and to suppress convection thus reducing defects in the grown *CdZnTe* crystals [31].

The experimental study on the LPEE growth of *GaAs* and *InGaAs* single crystals under a static magnetic field was carried out by *Sheibani et al.* [27]. In their experiment, various magnetic field levels were used. The results showed that at the 4.5 kG field level, convection was suppressed, and the growth was satisfactory. At higher levels of magnetic field, the experiments were not successful due to strong convection and interface instability.

A 3- D numerical simulation study was conducted by *S. Dost et al.* [28] to observe the effect of an axial magnetic field on the LPEE growth of *GaAs* crystals. Various levels of magnetic field and electric current densities were used in the simulations. Their study showed that at Ha=150, the flow field is stable, and suppressed. Between Ha=150 and Ha=220 levels, the flow patterns exhibits a transitional behavior. The flow intensity increases significantly with the increase in the magnetic field strength. Above Ha=220, the flow is unstable.

A numerical study was carried out by *C Stelian* and *Th. Duffor* [33] to investigate the effect of a static axial magnetic field on thermosolutal convection and segregation during Vertical Bridgman solidification of *GaInSb*. They showed that melt convection was

damped with the application of 0.5 Tesla axial magnetic field; however, they also observed an increase in the radial segregations. They concluded that the axial magnetic field alone is not beneficial for their system. A rotating magnetic field is also needed to create controlled mixing and decrease the radial segregations.

In the Czochralski (Cz) growth technique, strong temperature fluctuations and segregations occur due to the large melt volume used. Different types of magnetic fields have been used in Cz growth to control the transport structures in the melt. *J.Virbulis et al.* [34] studied flow in the silicon melt under the influence of static and dynamic (rotating, traveling) magnetic fields. Their numerical study showed that without a magnetic field, a strong vortex exists in the melt under the crystal, and a weak vortex in the outer part of the melt. With the application of a static magnetic field, the flow was suppressed and vortices merged to a single vortex. However, the static magnetic field alone was not sufficient to control the melt flow. In addition, cusp and alternating magnetic fields were also added to obtain a beneficial result [34]. The experimental study on the melt flow instability in Czochralski growth under static magnetic fields by L. Gorbunov [35] yielded similar results. Even though it was possible to control the velocity, temperature and concentration fluctuations in the melt using a static vertical magnetic field, concentration of oxygen, which is an important impurity penetrating from the crucible wall, increases significantly. Results showed that in Cz growth the use of a static vertical magnetic field alone was not sufficient.

2.2.2 Application of a Rotating Magnetic Field (RMF) in Crystal Growth

Rotating magnetic fields have been used in crystal growth to improve mixing and also to control heat and mass transport in the melt as well as the growth interface shape. A controlled fluid flow leads to more homogenous temperature and concentration distributions in the melt, thus improving the growth process and quality of crystals.

Another advantage of RMF is that an RMF system is simpler and inexpensive compared with static magnetic field systems.

A rotating magnetic field (RMF) can be produced by inductors (fed by an AC power source) spaced circumferentially at equal distances around a melt (or solution) zone. The induced magnetic field and the electric current in the conducting melt exert an electromagnetic force on the particles of the melt. The azimuthal component of this force, being the dominant one, creates stirring in the melt. The secondary flow due to the radial and axial body force components affects the heat and mass transfer characteristics of the melt.

In general, RMF has been used in the Traveling Heater Method (THM) for better mixing, in Bridgman and the Floating Zone method for reducing segregation of species, and in Czhochralski for controlling the oxygen concentration. In addition, RMF was also used to suppress natural convection in the microgravity environment.

Efficiency of RMF has been studied experimentally by *Gelfgat* and *Grobunov* [36] on the Sn-Bi and Sn-Pb melts. They showed that in the absence of RMF, the homogenization is very slow even though natural convection is present in the melt. However, with the application of RMF around 0.03 T, the melt becomes uniform in a short period of time (1 hour).

The effect of RMF on the growth interface and crystal composition uniformity was investigated experimentally by *I. V. Barmin et al.* [37] Their results showed that in the absence of rotating magnetic field, interface shape bows into the melt; however, with the application of RMF, the interface becomes convex to the melt and as a result radial homogeneity of the crystal composition can be achieved. They measured the composition of the *CdHgTe* crystals by energy- dispersive X-ray micro-analysis (EDX). The initial parts of the crystals, which were grown without magnetic field, exhibited a composition

of varying distribution (concave) whereas the later sections, which were grown under a rotating magnetic field, showed almost uniform composition distribution.

As stated earlier, high temperature gradients used in the THM results in strong convection in the solution thus affect the quality of crystals. The use of a strong stationary magnetic field may suppress convection; however it may also sometimes lead to non –uniformities in the crystals. The desired homogenous mixing in the solution can be realized using a rotating magnetic field. *Dost et al.* [30] carried out a numerical simulation to observe the effect of magnetic field in the growth of *CdTe* single crystals by THM. Their results showed that rotating magnetic field enhances mixing in the solution and increases the crystal uniformity.

Another study investigating the influence of rotating magnetic field on flow patterns and compositional uniformity in the solution zone of THM for the growth of *CdTe* was conducted by *Ghaddar et al.* [32]. They found that under microgravity conditions, RMF could be used to suppress the buoyancy-induced convection and to control the uniformity of the solution-zone composition. The same study revealed that at high-gravity levels rotating magnetic field could not totally suppress the buoyancy–induced convection.

The experimental and numerical study carried out for the growth of *GaAs* by vertical gradient freezing showed that the concave shape of the growth interface was improved considerably under the effect of RMF [38].

The numerical simulation study by *C. Stelian et al.* [39] on the growth of *GaInSb* by Vertical Bridgman showed that by the use of a rotating magnetic field intensity of 3.0 mT and frequency 5 kHz, radial segregations are maintained at lower values compared to those under no magnetic field. In addition, it was also shown that the application of RMF reduces the interface deflection.

The FZ process requires delicate control of the melt to minimize the instabilities associated with thermocapillary and buoyancy convections. Therefore, in the FZ, the application of magnetic field has become a part of the process to control heat and mass transport during the growth. The magnetic field applied to the system acts like an electromagnetic crucible and stabilizes the liquid bridge. Otherwise, the thermocapillary convection due to a large radial gradient of the axial velocity near the free surface leads to instabilities in the melt, which produces undesirable striations in the crystals. *Walker et al.* [22] investigated the effect of rotating magnetic field on the thermocapillary instability in the floating zone process. The results revealed that RMF adds an azimuthal velocity to the melt and stabilizes the instability due to thermocapillary convection.

A study by *Dold et al.* [23] has also shown that a rotating magnetic field in FZ growth of doped-silicon has significant effects on radial segregation and interface shape. RMF decreases the fluctuations of the dopant concentration and flattens the liquid/solid interfaces.

In the Czochralski growth process, a significant amount of oxygen diffuses into the silicon melt from the quartz crucible. This is an important problem in Cz technique and affects the quality of grown crystals. The use of RMF in Cz growth is common to enhance the transport of oxygen towards the growth interface and decreases the oxygen concentration in the crystal [40].

CHAPTER 3

LIQUID PHASE DIFFUSION (LPD) TECHNIQUE

Liquid Phase Diffusion is a solution growth technique that has been recently developed and used in the UVic crystal growth laboratory to grow Si_xGe_{1-x} single crystal seeds of 25 mm in diameter from the Ge-rich side of the binary phase diagram [7]. This chapter is devoted to the introduction of the LPD technique and its principles. First, the growth system will be briefly introduced, and then the growth steps and principles will be described.

3.1 LPD Growth System

The LPD growth system consists of the following: a three- zone solid tubular furnace operating at temperatures up to 1250 ^{0}C, the growth reactor which consists of a quartz crucible and pedestal, and an annular insulator (see Figure 3.1). The quartz crucible (growth zone) is loaded with three layers of charge materials namely *Si-source*, *Ge-solvent* and *Ge-seed*, and positioned in the middle zone of the furnace. To obtain a steep temperature gradient along the growth zone, an annular insulator is placed in the furnace, which covers the quartz crucible. The insulator material extends from slightly above the substrate to the bottom of the source material [7].

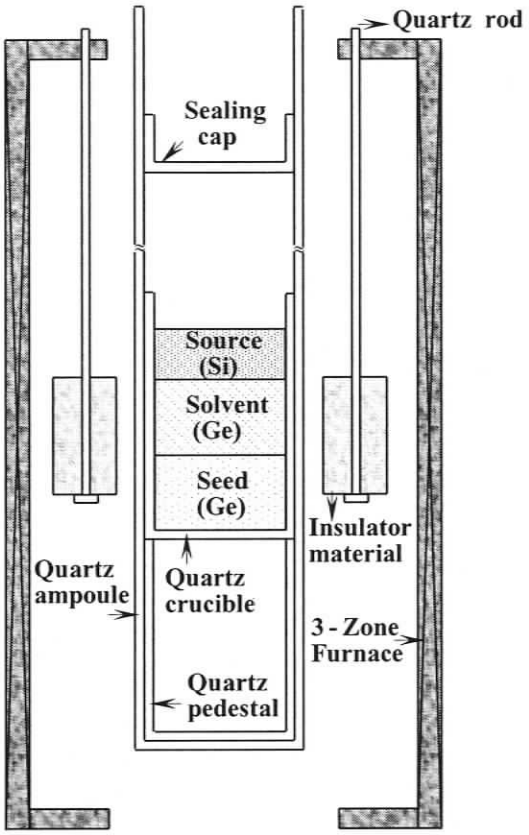

Figure 3.1- LPD growth set up

3.2 LPD Growth Steps and Principles

In LPD, the development of the desired steep and stable temperature profile is the first required step to achieve successful growth. This involves a great deal of measurement to find the temperatures of each zone of the furnace. Figure 3.2 shows thermal profiles measured along the quartz reactor, and also along the axis of the dummy silicon load [7].

After obtaining the appropriate thermal profile, the second step is the preparation of the charge materials, growth reactor and crucible. In this step, the charge materials are cut, cleaned and etched chemically to reduce the risk of contamination.

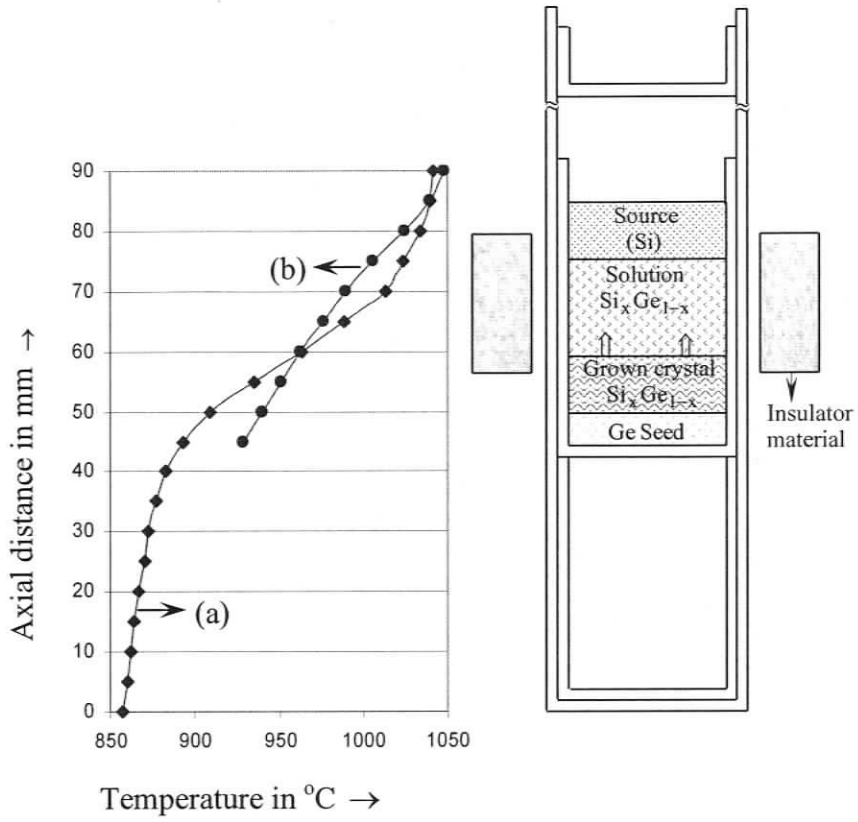

Figure 3. 2- LPD thermal profile along the quartz reactor (a) and the axis of the silicon dummy load (b) [7].

Following the chemical treatment, the charge materials are loaded into the growth reactor and the reactor is vacuumed to reduce the oxidizing molecules in it. Subsequently, the reactor tube is placed into the furnace and the growth process is initiated.

The growth mechanism of the LPD growth of Si_xGe_{1-x} is as follows. The solvent material (*Ge*) is placed between a single-crystal seed (*Ge*) and a polycrystalline source material (*Si*). These three vertically stacked solid charge materials held in a quartz crucible form the LPD growth cell, as illustrated in Fig.3.2. When the growth cell is located in a temperature gradient as seen in Figure 3.3, the solvent (*Ge*) and some part of the seed (*Ge*) melts. However, the source (*Si*) remains in the solid state due to its higher melting temperature. The germanium solvent (formed upon melting) dissolves silicon in accordance with the thermodynamic equilibrium and then silicon species are transported

into the liquid. As a result, a binary *Si-Ge* liquid mixture (solution) is formed. Subsequently, silicon species in the solution are transported towards the growth interface by diffusion and also by natural convection, and the solution near the growth interface becomes supersaturated in silicon. Then, solidification on the seed takes place due to constitutional supercooling, leading to crystal growth (see Figure 3.3). The growth mechanism of SiGe by LPD can be better understood by considering the Ge-rich side of the equilibrium phase diagram of SiGe alloy system as shown in Fig. 3.3. Assuming that the silicon concentration of the first supersaturated liquid is x_1^L, and the corresponding liquidus temperature of the supersaturated solution is T_1^L. Since T_1^L is higher than the liquid temperature of the solution near the interface indicated by a dashed line, the solution must be constitutionally supercooled, and consequently the solidification takes place. The growth interface then moves to a new position and this growth process repeats itself until the entire solution is consumed. For the detailed description of the LPD growth system and experiments, the reader is referred to [7, 8].

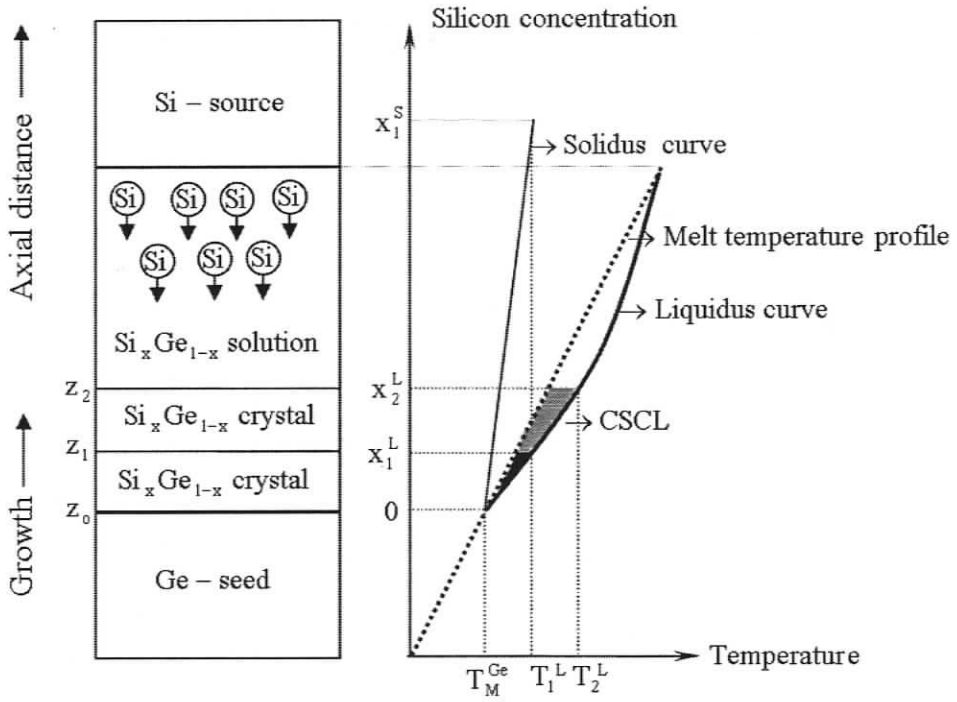

Figure 3.3- LPD growth principles

CHAPTER 4

MATHEMATICAL MODEL

This chapter presents a mathematical model for the Liquid Phase Diffusion growth of Si_xGe_{1-x} single crystals under applied static vertical and rotating magnetic fields. First, the model assumptions are introduced. Then, the transport equations governing heat, mass and momentum transfer are presented along with the boundary and interface conditions. The externally applied magnetic fields are incorporated into the model through body force terms in the momentum equation. The detailed derivations of magnetic body force terms for static and rotating magnetic fields are also presented.

4.1 Model Assumptions

In the present model, the liquid phase represents the *Ge*-rich *Si-Ge solution,* which is modeled as a binary mixture of Silicon and Germanium. In the solution, *Ge* is the *solvent*, while *Si* is the *solute* and *the solution* is assumed to be a heat and electric conducting incompressible Newtonian fluid. The solid phase, which represents the single crystal *Ge –seed* (*substrate*), polycrystalline *Si-source* and the quartz crucible, is considered as a heat conducting rigid material. The interface between the seed and the solution is referred to as *the growth interface* and the one between the solution and the source as *the dissolution interface*. The following assumptions are made in the model:

- All field variables (temperature T, velocity v, and concentration of solute c) are function of spatial coordinates and time.

- All solid phases are heat conducting rigid materials.
- The solution zone is a binary mixture of *heat and electric conducting incompressible Newtonian fluid.*
- Newton's law of viscosity, Fourier's law and Fick's law are the constitutive equations for stress, heat flux, and mass flux, respectively.
- *Boussinesq* approximation is assumed to be valid for the liquid mixture.

4.2 Governing Equations and Boundary Conditions

In this section, the governing equations for heat, mass and momentum transfers and the associated boundary and interface conditions are presented for the LPD system. The vertical cross section of the LPD growth system is shown in Figure 4.1. System dimensions and the physical properties of materials used in this numerical work are given in Tables (4.1) and (4.2).

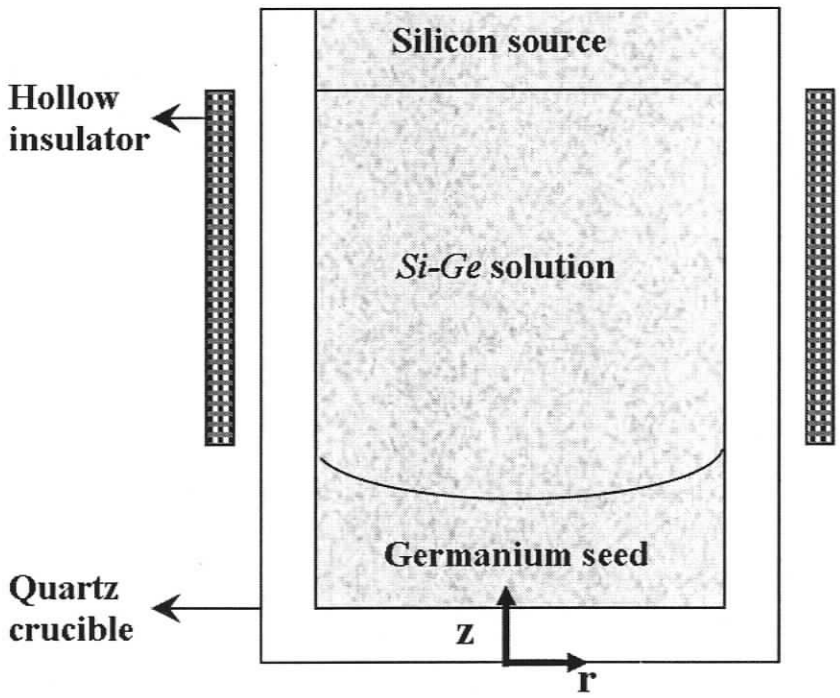

Figure 4.1- The vertical cross section of the LPD growth crucible.

Table 4.1- The dimensions of the LPD growth system [7]

Total length of the growth zone	40 mm
Initial height of the source	3 mm
Initial height of the seed	10 mm
Crystal diameter	25 mm
Total wall thickness of quartz reactor and crucible	4 mm

Table 4.2- Physical properties of growth materials and quartz crucible [7]

Physical parameter	***Si-source***	***Ge-substrate***	***$Si_x Ge_{1-x}$ growing crystal***	***$Si_x Ge_{1-x}$ Liquid solution***	***Quartz crucible***
Specific heat γ (J/kg K)	976 at 1300K 1037 (liquid)	396,1 at 1210K 380 (liquid)	391-487	380-406	1200 at 1300K
Thermal conductivity k (W/m K)	23.7 at 1273K	10.6 at 1210 K	10.6	42.8	2 at 1300 K
Mass diffusivity D (m^2/s)	N/A	N/A	10^{-20}	$2.5x10^{-8}$	N/A
Mass density ρ (kg/m^3)	2301,6 at 1300 K	5323 at 1210 K	4839-5323	5633	2200 at 1300 K
Thermal expansion β_T (1/K)	N/A	N/A	N/A	$1.2x10^{-4}$	N/A
Solutal expansion β_C (1/mol%Si)	N/A	N/A	N/A	0.0053	N/A
Enthalpy of fusion ΔH^F (kJ/kg)	1807.9	466.5	----------	----------	----------
Viscosity μ (kg/m s)	N/A	N/A	N/A	$7.35x10^{-4}$	N/A

4.2.1 Governing Equations and Boundary Conditions of the Liquid Phase

Under the above assumptions, the conservation of mass, balance of momentum, balance of energy and balance of mass for solute species yield respectively the well known field equations of continuity, momentum, energy and mass transport in the liquid phase [41, 42]. These three-dimensional time dependent governing equations are written in cylindrical coordinates (r, φ, z) as

Continuity

$$\frac{1}{r}\frac{\partial}{\partial r}(rv_r)+\frac{1}{r}\frac{\partial v_\varphi}{\partial \varphi}+\frac{\partial v_z}{\partial z}=0 \tag{4.1}$$

Momentum

$$\frac{\partial v_r}{\partial t}+v_r\frac{\partial v_r}{\partial r}+\frac{v_\varphi}{r}\frac{\partial v_r}{\partial \varphi}+v_z\frac{\partial v_r}{\partial z}-\frac{v_\varphi^2}{r}=-\frac{1}{\rho_L}\frac{\partial p}{\partial r}+\upsilon(\nabla^2 v_r-\frac{v_r}{r^2}-\frac{2}{r^2}\frac{\partial v_\varphi}{\partial \varphi})+\frac{F_r^M}{\rho_L} \tag{4.2}$$

$$\frac{\partial v_\varphi}{\partial t}+v_r\frac{\partial v_\varphi}{\partial r}+\frac{v_\varphi}{r}\frac{\partial v_\varphi}{\partial \varphi}+v_z\frac{\partial v_\varphi}{\partial z}+\frac{v_r v_\varphi}{r}=-\frac{1}{r\rho_L}\frac{\partial p}{\partial \varphi}+\upsilon(\nabla^2 v_\varphi-\frac{v_\varphi}{r^2}+\frac{2}{r^2}\frac{\partial v_r}{\partial \varphi})+\frac{F_\varphi^M}{\rho_L} \tag{4.3}$$

$$\frac{\partial v_z}{\partial t}+v_r\frac{\partial v_z}{\partial r}+\frac{v_\varphi}{r}\frac{\partial v_z}{\partial \varphi}+v_z\frac{\partial v_z}{\partial z}=-\frac{1}{\rho_L}\frac{\partial p}{\partial z}+\upsilon\nabla^2 v_z+\frac{F_z^M}{\rho_L}+\beta_T(T-T_o)g+\beta_C(c-c_o)g \tag{4.4}$$

where v_r, v_φ, and v_z are, respectively, the velocity components in the radial (r), circumferential (φ) and vertical (z) directions. ρ_L is the reference density of the solution, υ is the kinematic viscosity of the solution, T is the absolute temperature at a point in the liquid, c is the mass fraction of silicon, and T_o and c_o denote the reference temperature and mass fraction, respectively. p is the pressure. F_r^M, F_φ^M, F_z^M are the magnetic body force components including the contribution of both static and rotating

magnetic fields. β_T and β_C are the thermal and solutal expansion coefficient, respectively.

Energy

$$\left(\frac{\partial T}{\partial t}+v_r\frac{\partial T}{\partial r}+\frac{v_\varphi}{r}\frac{\partial T}{\partial \varphi}+v_z\frac{\partial T}{\partial z}\right)=\frac{k_L}{\rho_L\gamma_L}\nabla^2 T \tag{4.5}$$

where k_L and γ_L represent the thermal conductivity and specific heat capacity of the liquid solution, respectively.

Mass transport for the solute (silicon)

$$\left(\frac{\partial c}{\partial t}+v_r\frac{\partial c}{\partial r}+\frac{v_\varphi}{r}\frac{\partial c}{\partial \varphi}+v_z\frac{\partial c}{\partial z}\right)=D_{L,Si}\nabla^2 c \tag{4.6}$$

where $\nabla^2=\frac{1}{r}\frac{\partial}{\partial r}\left(r\frac{\partial}{\partial r}\right)+\frac{1}{r^2}\frac{\partial^2}{\partial \varphi^2}+\frac{\partial^2}{\partial z^2}$ is the Laplacian operator and $D_{L,Si}$ represents the diffusion coefficient of silicon in the liquid solution.

Boundary and interface conditions

In the liquid phase, we employed the following boundary conditions.

At the vertical wall:

No-slip boundary condition is assumed for the velocity field at the vertical wall (boundary between the liquid and quartz crucible). In other words, the fluid velocity is taken equal to the velocity of the solid surface. For the mass balance of solute (silicon), the vertical wall is assumed impermeable to the species in the solution. Thus we write,

$$v_r=0,\ v_\varphi=0, v_z=0,\ \frac{\partial c}{\partial r}=0 \tag{4.7}$$

At the growth interface:

For the treatment of the growth interface, the following assumptions are made.

- Mass fraction of silicon in the liquid and solid phases near the growth interface can be obtained from the *Si-Ge* binary phase diagram by assuming a local thermodynamic equilibrium. In order to find the liquid and solid equilibrium compositions of silicon, equations (4.8) and (4.9) are obtained by curve fitting the data collected from the liquidus and solidus curves of the phase diagram in the compositional range of interest (indicated in Figure 4. 2 left)[7].

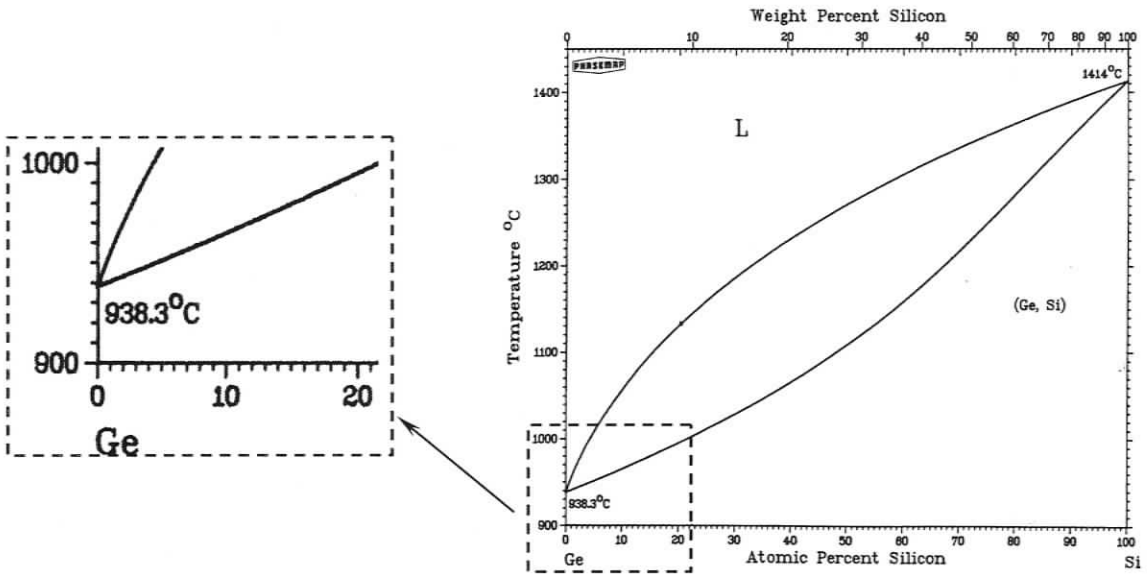

Figure 4.2- Equilibrium phase diagram of *SiGe* alloys (right) and the compositional range of interest (left)

$$c_{eq}^{L} = a_L T^3 + b_L T^2 + c_L T + d_L, \tag{4.8}$$

$$c_{eq}^{S} = \left(T - a_S\right)/b_S \tag{4.9}$$

Table 4.3- Coefficients for equations (4.8) and (4.9)

a_L (1/K^3)	b_L (1/K^2)	c_L (1/K)	d_L	a_S (K)	b^s (K)
2.5984*10^{-9}	-8.7189*10^{-6}	0.0099041	-3.822	1211.45	639.63

- The growth rate in LPD is about 10^{-8} m/s, which is smaller than the velocities of the fluid particles ($\cong 10^{-3}$ m/s); therefore, velocity components of fluid particles at the growth interface are assumed zero [7,41].
- Due to the small growth rate, the latent heat dissipates without disturbing the continuity of the heat flux at the interface, so it is neglected.
- The diffusion of silicon species through the crystal is neglected due to the very small value of the solid-state diffusion coefficient of silicon.

Under these assumptions, we have,

$$c = c_{gi}^{L}, \quad v_r = 0, \quad v_\varphi = 0, \quad v_z = 0$$

$$k_S \frac{\partial T_S}{\partial n} - k_L \frac{\partial T_L}{\partial n} = 0 \tag{4.10}$$

$$\rho_S u_g \left(c_{gi}^{S} - c_{gi}^{L}\right) = \rho_L D_{L,Si} \frac{\partial c}{\partial n}$$

where c_{gi}^{S} and c_{gi}^{L}, the mass fraction of silicon in the solid and liquid phases on the growth interface("*gi*"), respectively, are calculated from the Si-Ge binary phase diagram. k_S and k_L denote the thermal conductivity of the solid and liquid phases, respectively. T_L and T_S are the liquid and solid temperatures at the growth interface, $\partial / \partial n$ is the normal derivative operator, and u_g is the growth velocity.

At the dissolution interface:

For the treatment of the dissolution interface, the following assumptions are made:

- Dissolution rate of the silicon source material was reported very small (approximately 0.3 mm/day); therefore, the velocity components of fluid particles at the dissolution interface can be set to zero [7, 41].
- Between the liquid and the dissolution interface, heat flux is assumed continuous.
- The mass balance equation at the dissolution interface is excluded, due to the very small dissolution rate.

Thus, we write

$$c = c_{di}^{L}, \quad v_r = 0, v_\varphi = 0, v_z = 0 \tag{4.11}$$

$$k_S \frac{\partial T_S}{\partial n} - k_L \frac{\partial T_L}{\partial n} = 0 \tag{4.12}$$

where c_{di}^{L} is the mass fractions of the solute (silicon) at the dissolution interface ("*di*"), which is calculated from the phase diagram.

4.2.2 Governing Equations and Boundary Conditions for the Solid Phase

The species mass balance equation in the substrate and the growing crystal is excluded because of the very slow solid state diffusion. Due to the assumption of rigidity, the momentum balance equations are also excluded from the list of governing equations for the solid phase. The only governing equation left for the solid phase is therefore the energy balance.

Energy Balance

$$\frac{\partial T}{\partial t} = \frac{k_T}{\rho_S \gamma_S}\left(\frac{1}{r}\frac{\partial T}{\partial r} + \frac{\partial^2 T}{\partial r^2} + \frac{\partial^2 T}{\partial \varphi^2} + \frac{\partial^2 T}{\partial z^2}\right) \tag{4.13}$$

Boundary conditions

Thermal boundary conditions for the vertical wall, top and bottom surfaces of the quartz crucible are modeled by

$$-k_s \frac{\partial T}{\partial n} = h\left[T - T_f(z)\right] \tag{4.14}$$

where $T_f(z)$ is the experimentally obtained ambient temperature inside the furnace along the quartz ampoule wall or on top and bottom surfaces (see Figure 3.2, curve (a)), h is the modified heat transfer coefficient, including the contribution of convection and radiation effect on heat loss. The modified heat transfer coefficient is approximated using preliminary experimental results (such as the measured thermal profile, solute distribution in a grown crystal, and the position of the initial growth interface) [7, 8]. A perfect thermal contact is also assumed at the melt-ampoule, crystal -ampoule and inner-outer crucible boundaries. Therefore, at these boundaries, the heat flux is assumed continuous.

Initial conditions at t = 0

$$c = c_o, \;\; v_r = 0, v_\varphi = 0, \;\; v_z = 0 \tag{4.15}$$

4.3 Magnetic Body Forces

In this section, the magnetic body force components appearing in the momentum balance equations (4.2-4.4) are derived.

$$F_r^M = f_{st,r}^M + f_{rot,r}^M \qquad F_\varphi^M = f_{st,\varphi}^M + f_{rot,\varphi}^M \qquad F_z^M = f_{st,z}^M + f_{rot,z}^M \tag{4.16}$$

In the derivation of above components, Maxwell equations governing the electromagnetic field are used as a starting point. A summary of the Maxwell equations used in this chapter is given in table 4.4

Table 4.4- Summary of the Maxwell equations [43, 44]

MAXWELL EQUATIONS	
Gauss' law of magnetism	$\nabla \cdot \mathbf{B} = 0$
Faraday's law of induction	$\nabla \times \mathbf{E} = -\partial \mathbf{B}/\partial t$
Ampere's law	$\nabla \times \mathbf{B} = \mu_o \mathbf{j}$

Before beginning the detailed derivations of the body forces due to static and rotating magnetic fields, it will be helpful to review some definitions and concepts of the electromagnetic theory of MHD.

A charged particle experiences three types of forces:

i) The particle repelled or attracted by other charged particles, and suffers an electrostatic field, $\mathbf{E}_s$,

ii) The charged particles in motion produce a magnetic field **B**. Due to the interaction of the induced magnetic field with a charged particle, a magnetic force ($\mathbf{v} \times \mathbf{B}$) is created,

iii) According to Faraday law of magnetism, if the magnetic field is changing with time, a particle is subjected to an induced electric field ($\mathbf{E}_i$). the total force on the particle can be defined as $\mathbf{E} + \mathbf{v} \times \mathbf{B}$,where $\mathbf{E}$ is $\mathbf{E}_s + \mathbf{E}_i$

4.3.1 Static Vertical Magnetic Field

Here, we introduce the interaction of a vertically applied static magnetic field with the liquid phase in motion (in our case, the *Si-Ge* solution). The liquid phase is assumed a heat- and electric-conducting but non-magnetizable and non-polarizable material. Under these assumptions, the motion of such a liquid under the effect of an externally applied magnetic field induces an electric current which is given by Ohm's law as,

$$\mathbf{j} = \sigma_L (\mathbf{E} + \mathbf{v} \times \mathbf{B}) \tag{4.17}$$

where $\mathbf{j}$ is the electric current density, σ_L is the electric conductivity of the liquid, $\mathbf{E}$ is the static electric field vector due to the electric charges, $\mathbf{v} = (v_r \mathbf{e}_r + v_\varphi \mathbf{e}_\varphi + v_z \mathbf{e}_z)$ is the mass averaged velocity of the liquid particles at a point in the mixture, and $\mathbf{B}$ is the magnetic field vector (sometimes called the magnetic induction or magnetic flux density). In the present model the magnetic field is assumed uniform, static, and perfectly aligned with the symmetry axis of the liquid. Hence,

$$\mathbf{B} = B\mathbf{e}_z \tag{4.18}$$

where B is the field intensity.

For a static magnetic field, Faraday law of induction ($\nabla \times \mathbf{E} = -\partial \mathbf{B} / \partial t$) becomes $\nabla \times \mathbf{E} = 0$. This equation is satisfied by introducing the electric potential function ϕ, where $\mathbf{E} = -\nabla \phi$ [*]. Thus, equation (4.17) takes the following form,

---

[*] Due to the products rule of $\nabla \times (\nabla \phi) = 0$

$$\mathbf{j} = \sigma_L\left(-\nabla\phi + \mathbf{v}\times\mathbf{B}\right) \tag{4.19}$$

where ∇ is the gradient operator defined as $\nabla = \frac{\partial}{\partial r}\mathbf{e}_r + \frac{1}{r}\frac{\partial}{\partial \varphi}\mathbf{e}_\varphi + \frac{\partial}{\partial z}\mathbf{e}_z$ in cylindrical coordinates. According to Ampere's law ($\nabla\times\mathbf{B} = \mu_o\mathbf{j}$), the induced electric current $\sigma_L(\mathbf{v}\times\mathbf{B})$ produces its own magnetic field (induced magnetic field) in the liquid, where μ_o is the magnetic permeability of the vacuum. This induced magnetic field interacts with the externally applied magnetic field, thereby changing the magnetic field distribution in the liquid. To evaluate the significance of the induced magnetic field, Ampere's law is made dimensionless using the variables defined as $\hat{\nabla} = l_o\nabla$, $\hat{\mathbf{B}} = \mathbf{B}/B_o$ and $\hat{\mathbf{j}} = \mathbf{j}/\sigma_L v_o B_o$.

$$\hat{\nabla}\times\hat{\mathbf{B}} = \mathrm{Re}_m\,\hat{\mathbf{j}} \tag{4.20}$$

where l_o, B_o and v_o are the characteristic (reference) length, magnetic field intensity and velocity. Here, $\mathrm{Re}_m = \mu_o\sigma_L v_o l_o$ is the magnetic Reynolds number. The magnetic Reynolds number is analogues to the well-known Reynolds number. As we can see, the magnetic Reynolds number is the ratio of the convective term, $v_o B_o / l_o$ to the diffusive term $B_o / \mu_o\sigma_L l_o^2$. Therefore, it characterizes the effect of flow on the magnetic field. In the calculation of Re_m, v_o (the maximum buoyancy velocity ($\cong 10^{-3}$ m/s)) and l_o (the radius of the melt (12.5 * 10^{-3} m)) are used. Since the value of Re_m ($\cong 10^{-5}$) is far smaller than unity, the right hand side of the equation (4.20) can be set to zero. This implies that the induced magnetic field in the liquid solution can be neglected and hence the applied magnetic field is uniform.

The interaction of the applied static magnetic field with the induced electric current produces a Lorentz force $\mathbf{f}_{st}^{M}$, which acts on the points of the liquid. Again, under the assumptions mentioned earlier (no polarization, no magnetization, etc), the Lorentz force per unit volume may be written as

$$\mathbf{f}^{M} = \mathbf{j} \times \mathbf{B} \tag{4.21}$$

This is a good assumption in metallic liquids [34]. On combining equations (4.19) and (4.21), the following is obtained:

$$\mathbf{f}_{st}^{M} = \begin{Bmatrix} f_{st,r}^{M}\mathbf{e}_r \\ f_{st,\varphi}^{M}\mathbf{e}_\varphi \end{Bmatrix} = \begin{Bmatrix} -\sigma_L B \dfrac{1}{r}\dfrac{\partial \phi}{\partial \varphi}\mathbf{e}_r - \sigma_L B^2 v_r \mathbf{e}_r \\ \sigma_L B \dfrac{\partial \phi}{\partial r}\mathbf{e}_\varphi - \sigma_L B^2 v_\varphi \mathbf{e}_\varphi \end{Bmatrix} \tag{4.22}$$

where $f_{st,r}^{M}$ and $f_{st,\varphi}^{M}$ are the magnetic body force components in the radial (r) and azimuthal (φ) directions (see Figure 4.3).

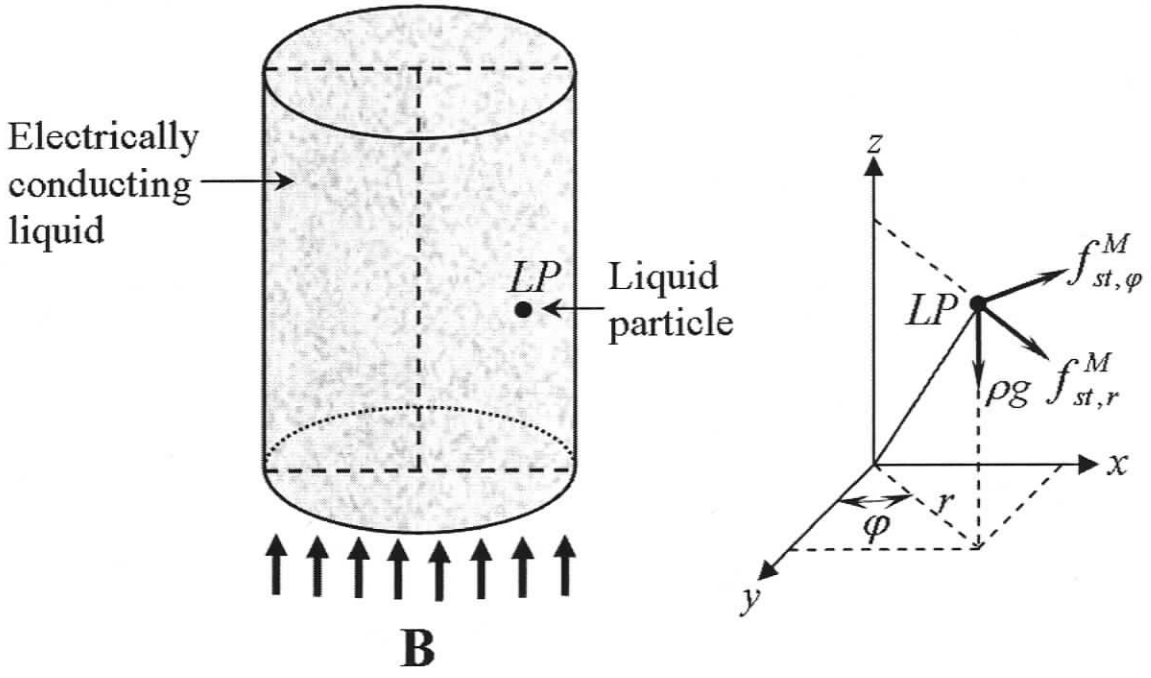

Figure 4.3- Schematic representation of the application of static vertical magnetic field and body force components acting on a liquid particle

The electric potential (ϕ) terms in magnetic body force components can be obtained using the conservation of charge, which requires that the divergence of the current density vector is zero, namely $\nabla \cdot \mathbf{j} = \sigma_L \nabla \cdot \left(-\nabla\phi + \mathbf{v} \times \mathbf{B}\right) = 0$.

$$\nabla^2 \phi = \nabla \cdot \left(\mathbf{v} \times \mathbf{B}\right) \; or \; \nabla^2 \phi = B\mathbf{e}_z \cdot \boldsymbol{\omega} \qquad (4.23)$$

$$\nabla^2 \phi = B\left(\frac{\partial v_\varphi}{\partial r} + \frac{v_\varphi}{r} - \frac{1}{r}\frac{\partial v_r}{\partial \varphi}\right)$$

where $\nabla \cdot \left(\mathbf{v} \times \mathbf{B}\right) = B\mathbf{e}_z \cdot \left(\nabla \times \mathbf{v}\right) - B\mathbf{v} \cdot \overbrace{\left(\nabla \times \mathbf{e}_z\right)}^{=0}$ is used and the curl of velocity vector is defined as vorticity vector, $\boldsymbol{\omega} = \left(\nabla \times \mathbf{v}\right)$.

As can be seen from equation (4.23), the vorticity vector is parallel to the externally applied static vertical magnetic field. Equation (4.23) also shows that in the vorticity regions, electrical potential differences exist. Therefore, an electric charge distribution is produced within the liquid solution that gives rise to a static electric field. In this work, we have considered both cases (i.e, Lorentz forces with and without the contribution of electric potential) to see the significance of the electric potential on the flow field.

Since the electrical conductivity of the liquid solution ($\sigma_L = 1.7 \times 10^6$ 1/Ω.m) is greater than that of the substrate ($\sigma_{Ge} = 6.06 \times 10^5$ 1/Ω.m), the source ($\sigma_{Si} = 4.25 \times 10^4$ 1/Ω.m) and the crucible ($\cong 10^{-7}$ 1/Ω.m), all boundaries surrounding the solution are assumed to be electrically insulated. This means that no electric current passage is allowed through the insulating wall. Therefore, the normal components of the electric current j_n have to be zero. In what follows, the boundary condition for equation (4.23) can be written as $\partial\phi / \partial n = 0$.

4.3.2 Rotating Magnetic Field (RMF)

In this section, we formulate the interaction of a rotating magnetic field with the liquid *Si-Ge* solution. Thus, we consider a horizontal (transverse) magnetic field rotating at a given angular frequency, $\omega_B = 2\pi f$ where f is frequency. Hereafter, this transverse magnetic field will be referred to as Rotating Magnetic Field, (RMF). Before starting to the derivation of Lorentz force components, we will briefly discuss the principle of a rotating magnetic field.

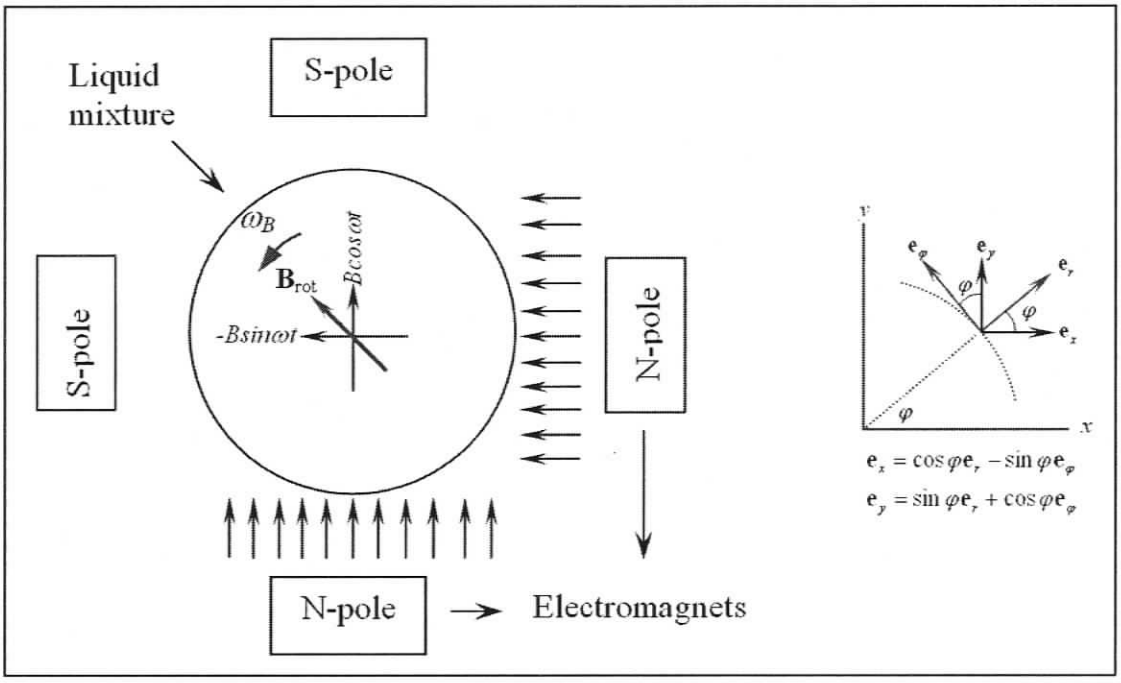

Figure 4.4- A representative figure for generating rotating magnetic field

A rotating magnetic field might be imposed on the liquid melt in two ways. The first method is to locate at least two electro-magnets at right angle around the liquid zone. When both of these electro-magnets are fed by out of phase alternating currents (AC), two sinusoidally varying magnetic field components are generated (see Figure 4.4). The created magnetic field components are perpendicular to each other and have a phase difference. Vector summation of these alternating magnetic field components gives a

resultant magnetic field that rotates on a horizontal plane perpendicular to the centerline of the growth cell. The second method might be locating several electro-magnets circumferentially around the liquid zone at equal distance, which are powered by a direct current (DC). Switching electro-magnets on and off sequentially at a given frequency will be equivalent to the rotation of the magnetic field lines. Both ways have been used in material processing such as crystal growth or solidification to induce controlled stirring action or forced convection on the liquid solution.

The externally applied rotating magnetic field interacts with the induced electric current, thus producing a Lorentz force with the components in radial (r), azimuthal (φ) and axial (z) directions (see Figure 4.5).

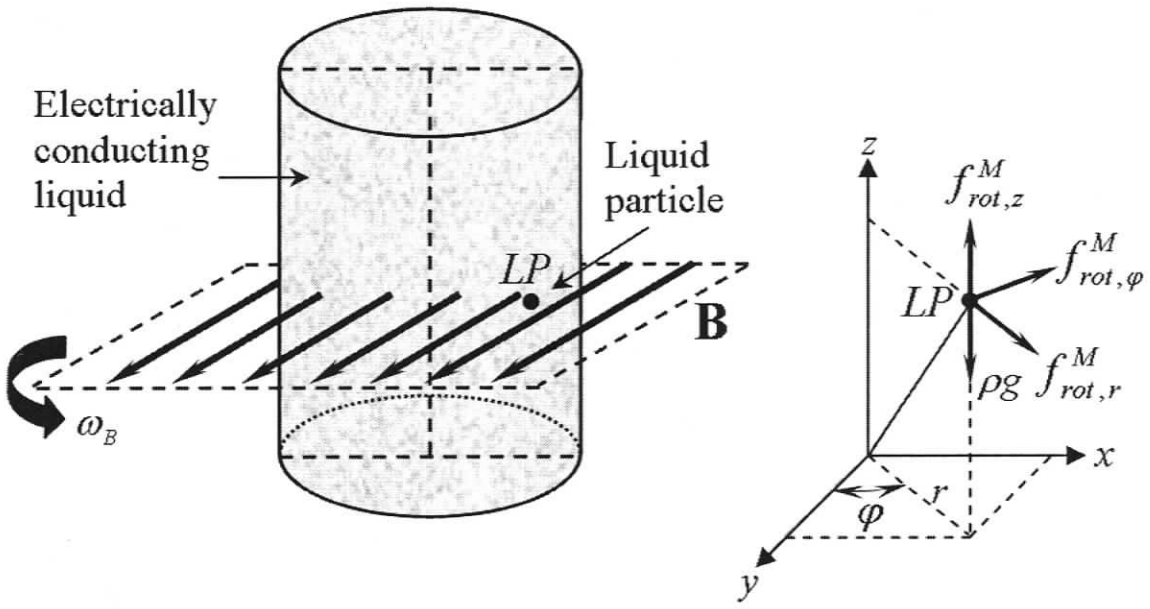

Figure 4.5- Schematic representation of the application of RMF and body force components acting on a liquid particle

In the following is given the derivation of equations for a rotating magnetic field. In these derivations, it is assumed that the height of the magnetic field generator is far greater than that of the liquid domain. Therefore, the externally applied rotating magnetic field (RMF) vector **B** is independent of the z (axial)-direction, meaning that $B_z = 0$. On decomposing

the $\mathbf{B}$ into its Cartesian components B_x and B_y in x- and y- directions, respectively, $\mathbf{B} = \mathbf{B}(B_x, B_y, t)$ can be written in the following form,

$$\mathbf{B} = -B\sin\omega_B t\,\mathbf{e}_x + B\cos\omega_B t\,\mathbf{e}_y \tag{4.24}$$

In cylindrical coordinate system, equation (4.24) becomes

$$\mathbf{B} = B\sin(\varphi - \omega_B t)\,\mathbf{e}_r + B\cos(\varphi - \omega_B t)\,\mathbf{e}_\varphi \tag{4.25}$$

where the relations $\mathbf{e}_x = \cos\varphi\,\mathbf{e}_r - \sin\varphi\,\mathbf{e}_\varphi$, and $\mathbf{e}_y = \sin\varphi\,\mathbf{e}_r + \cos\varphi\,\mathbf{e}_\varphi$ are used.

The equation (4.25) defines the magnetic field flux produced by a magnetic field generator or inductor. It is important to note that the interaction of an applied magnetic field with a conducting liquid in motion changes the magnetic field distribution in the melt, which is governed by the well-known induction (or advection-diffusion type) equation.

$$\frac{\partial \mathbf{B}}{\partial t} = \frac{1}{\mu_o \sigma_L}\nabla^2\mathbf{B} + \nabla\times(\mathbf{v}\times\mathbf{B}) \tag{4.26}$$

This advection-diffusion type equation can be obtained as follows; on combining Amper's law ($\nabla\times\mathbf{B} = \mu_o\mathbf{j}$) and Ohm's law $\mathbf{j} = \sigma_L(\mathbf{E} + \mathbf{v}\times\mathbf{B})$, one can write

$$\nabla\times\mathbf{B} = \mu_o\sigma_L(\mathbf{E} + \mathbf{v}\times\mathbf{B}) \tag{4.27}$$

Then, taking the curl of equation (4.27) and with the help of the identity $\nabla\times(\nabla\times\mathbf{B}) = \nabla(\nabla\cdot\mathbf{B}) - \nabla^2\mathbf{B}$, we eliminate the electric field using Faraday's law of induction, $\nabla\times\mathbf{E} = -\partial\mathbf{B}/\partial t$, and arrive at equation (4.26). Here, note that $\nabla\cdot\mathbf{B} = \mathbf{0}$ due to

Gauss' law of magnetism. To determine the effect of fluid flow on magnetic field distribution in the liquid solution, equation (4.26) is expressed in a dimensionless form by employing the following dimensionless parameters ($\hat{\nabla} = l_o \nabla$, $\hat{\mathbf{v}} = \mathbf{v}/v_o$, $\partial / \partial \hat{t} = (l_o / v_o)\partial / \partial t$, $\hat{\mathbf{B}} = \mathbf{B} / B_o$) as

$$\frac{\partial \hat{\mathbf{B}}}{\partial \hat{t}} = \frac{1}{Re_m} \hat{\nabla}^2 \hat{\mathbf{B}} + \hat{\nabla} \times \left(\hat{\mathbf{v}} \times \hat{\mathbf{B}} \right) \tag{4.28}$$

where $\mathrm{Re}_m = v_o l_o \mu_o \sigma_L$ is the magnetic Reynolds number. If the magnetic Reynolds number is very small compared to unity, i.e., $\mathrm{Re}_m << 1$, we can safely ignore the advection term, $\nabla \times (\mathbf{v} \times \mathbf{B})$. For the present example, the value of the magnetic Reynolds number is $\cong 10^{-5}$. This approximation states that the fluid is treated as a stationary solid conductor. This corresponds to the case where the influence of fluid flow on the magnetic field distribution in the liquid can be ignored. Hence, we may obtain the diffusion equation as

$$\frac{\partial \mathbf{B}}{\partial t} = \frac{1}{\mu_o \sigma_L} \nabla^2 \mathbf{B} \tag{4.29}$$

It is also assumed that the magnetic field penetrates over the solution volume without experiencing any change. To satisfy this assumption the skin depth ($\delta = \sqrt{2/\sigma_L \mu_o \omega_B}$), which is the distance that the magnetic field travels through a conducting liquid without being changed or modified, has to be much greater than the radius of the liquid domain ($\delta >> l_o$). The *skin depth* and the *shielding* parameter are usually used interchangeably. If the characteristic velocity, v_o in the magnetic Reynolds number is replaced by $\omega_B l_o$, the so-called shielding parameter (S) can be obtained as $S = \mu_o \sigma_L \omega_B l_o^2$ or $S = 2\left(l_o^2 / \delta^2\right)$. The condition where $\delta >> l_o$ or $S << 1$ refers to the fact that magnetic field distribution is

not affected by the presence of a conducting liquid [45]. The opposite scenario ($\delta << l_o$ or $S >> 1$) implies that the magnetic field can slightly penetrates into the solution because it is expelled due to the high conductivity of the solution, large angular frequency of the magnetic field or combination of the both. In the present work, the low frequency approximation is adopted; $\delta >> l_o$ or $S << 1$. For the present LPD system, the penetration depth δ is approximately 12 cm, which is calculated using the characteristic length l_o (radius of liquid) of 1.25 cm and magnetic field frequency of 10 Hz. The low frequency assumption is a very important simplification in the treatment of the present problem since the computation of magnetic field distribution within the liquid mixture is not required.

Analogous to the definition of the electric field $\mathbf{E}$ in terms of electric scalar potential ϕ we can also define the magnetic field $\mathbf{B}$ in terms of a vector potential $\mathbf{A}$ that satisfies Gauss' law of magnetism ($\nabla \cdot \mathbf{B} = 0$):

$$\mathbf{B} = \nabla \times \mathbf{A} \tag{4.30}$$

where the identity $\nabla \cdot (\nabla \times \mathbf{A}) = 0$ is used.

Using equation (4.30), we can present Faraday's law of induction in terms of magnetic vector potential as

$$\nabla \times \left(\mathbf{E} + \frac{\partial \mathbf{A}}{\partial t} \right) = 0 \tag{4.31}$$

The quantity with vanishing curl in equation (4.31) can be written as a gradient of a scalar function or scalar potential Φ (note that scalar potential for rotating magnetic field is denoted with upper case psi) with the help of $\nabla \times (-\nabla \Phi) = 0$. In what follows is

$$-\nabla \Phi = \mathbf{E} + \frac{\partial \mathbf{A}}{\partial t} \Rightarrow \mathbf{E} = -\left(\nabla \Phi + \frac{\partial \mathbf{A}}{\partial t} \right) \tag{4.32}$$

Comparison of equations (4.25) with (4.30) defines the vector potential in the form of

$$\mathbf{A} = -Br\cos(\varphi - \omega_B t)\,\mathbf{e}_z \tag{4.33}$$

Casting equation (4.31) into equation (4.32) yields the electric field vector as

$$\mathbf{E} = -\nabla\Phi + \omega_B Br\sin(\varphi - \omega_B t)\mathbf{e}_z \tag{4.34}$$

Since the applied magnetic field rotates with the frequency of ω_B, the electric field **E**, current density **j** and scalar electric potential Φ will also change with the same frequency. Therefore, the scalar potential (Φ) can be split into two parts, namely $\Phi_1(r,z)$ and $\Phi_2(r,z)$, in order to put it in the same form as the rotating magnetic field;

$$\Phi(r,\varphi,z,t) = \Phi_1(r,z)\sin(\varphi - \omega_B t) + \Phi_2(r,z)\cos(\varphi - \omega_B t) \tag{4.35}$$

Substituting equation (4.25), (4.34) and (4.35) into Ohm's law $\mathbf{j} = \sigma(\mathbf{E} + \mathbf{v}\times\mathbf{B})$, we can write the current flux as

$$\begin{aligned}
\mathbf{j} = {} & \sigma_L\left[-\sin(\varphi-\omega_B t)\frac{\partial\Phi_1}{\partial r} - B\cos(\varphi-\omega_B t)v_z - \cos(\varphi-\omega_B t)\frac{\partial\Phi_2}{\partial r}\right]\mathbf{e}_r \\
& + \sigma_L\left[-\frac{1}{r}\Phi_1\cos(\varphi-\omega_B t) + \frac{1}{r}\Phi_2\sin(\varphi-\omega_B t) + B\sin(\varphi-\omega_B t)v_z\right]\mathbf{e}_\varphi \\
& + \sigma_L\left[\begin{array}{l} -\sin(\varphi-\omega_B t)\dfrac{\partial\Phi_1}{\partial z} - \cos(\varphi-\omega_B t)\dfrac{\partial\Phi_2}{\partial z} + \omega_B Br\sin(\varphi-\omega_B t) \\ + v_r B_{rot}\cos(\theta-\omega_B t) - v_\varphi B\sin(\varphi-\omega_B t)\end{array}\right]\mathbf{e}_z
\end{aligned} \tag{4.36}$$

The magnetic body force components per unit volume, ($\mathbf{f}_{rot}^M = f_{rot,r}^M\mathbf{e}_r + f_{rot,\varphi}^M\mathbf{e}_\varphi + f_{rot,z}^M\mathbf{e}_z$) on a point within the liquid solution due to the application of a rotating magnetic field can be obtained by combining equations (4.25) and (4.36) using $\mathbf{f}_{rot}^M = \mathbf{j}\times\mathbf{B}$.

$$f_{rot,r}^{M} = \frac{\sigma_L B}{2}\sin 2(\varphi-\omega_B t)\frac{\partial \Phi_1}{\partial z} + \sigma_L B\left(\frac{1+\cos 2(\varphi-\omega_B t)}{2}\right)\frac{\partial \Phi_2}{\partial z}$$
$$-\frac{\sigma_L B^2 \omega_B r}{2}\sin 2(\varphi-\omega_B t) - v_r \sigma_L B^2\left(\frac{1+\cos 2(\varphi-\omega_B t)}{2}\right) \tag{4.37a}$$
$$+\frac{v_\varphi \sigma_L B^2}{2}\sin 2(\varphi-\omega_B t)$$

$$f_{rot,\varphi}^{M} = -\sigma_L B\left(\frac{1-\cos 2(\varphi-\omega_B t)}{2}\right)\frac{\partial \Phi_1}{\partial z} - \frac{\sigma_L B}{2}\sin 2(\varphi-\omega_B t)\frac{\partial \Phi_2}{\partial z}$$
$$+\omega\sigma_L B^2 r\left(\frac{1-\cos 2(\varphi-\omega_B t)}{2}\right) + \frac{v_r \sigma_L B}{2}\sin 2(\varphi-\omega_B t) \tag{4.37b}$$
$$-v_\varphi \sigma_L B^2\left(\frac{1-\cos 2(\varphi-\omega_B t)}{2}\right)$$

$$f_{rot,z}^{M} = -\frac{\sigma_L B}{2}\sin 2(\varphi-\omega_B t)\frac{\partial \Phi_1}{\partial r} - \sigma_L v_z B^2\left(\frac{1+\cos 2(\varphi-\omega_B t)}{2}\right)$$
$$-\sigma_L B\left(\frac{1+\cos 2(\varphi-\omega_B t)}{2}\right)\frac{\partial \Phi_2}{\partial r} + \frac{\sigma_L B}{2r}\Phi_1 \sin 2(\varphi-\omega_B t) \tag{4.37c}$$
$$-\frac{\sigma_L B}{r}\Phi_2\left(\frac{1-\cos 2(\varphi-\omega_B t)}{2}\right) - \sigma_L v_z B^2\left(\frac{1-\cos 2(\varphi-\omega_B t)}{2}\right)$$

where the following trigonometric relations are used.

$$\sin 2\alpha = 2\sin\alpha\cos\alpha,\quad \cos^2\alpha = \left(\frac{1+\cos 2\alpha}{2}\right),\quad \sin^2\alpha = \left(\frac{1-\cos 2\alpha}{2}\right) \tag{4.38}$$

As can be seen from equation (4.37), the body force components have time independent and oscillating parts with double frequency ($2\omega_B$). Therefore, to simplify these equations, time averaging is employed.

$$\left\langle f_{rot,r,\varphi,z}^{M}\right\rangle = \frac{1}{2\pi}\int_0^{2\pi} f_{rot,r,\varphi,z}^{M}\, d\omega t \tag{4.39}$$

Since $\int_0^{2\pi} \sin 2(\varphi - \omega t)\, d\omega t = 0$ and $\int_0^{2\pi} \cos 2(\varphi - \omega t)\, d\omega t = 0$, the time dependent parts that oscillate with double frequency drop out and the body force components reduce to mean forces as

$$\left\langle f_{rot,r}^{M} \right\rangle = \frac{B\sigma_L}{2}\left\{ \frac{\partial \Phi_2}{\partial z} - v_r B \right\} \tag{4.40a}$$

$$\left\langle f_{rot,\varphi}^{M} \right\rangle = \frac{1}{2}\sigma_L B\left(-\frac{\partial \Phi_1}{\partial z} + (\omega_B r - v_\varphi)B \right) \tag{4.40b}$$

$$\left\langle f_{rot,z}^{M} \right\rangle = \sigma_L B\left(-Bv_z - \frac{1}{2}\frac{1}{r}\frac{\partial (r\Phi_2)}{\partial r} \right) \tag{4.40c}$$

To determine the dominant Lorentz force component, equation (4.40a-c) can be expressed in dimensionless form using following scaling factors; $f_{rot,\varphi}^{L} = \hat{f}_{rot,\varphi}^{L}\sigma_L l_o \omega_B B^2$, $B = \hat{B}B_o$, $\Phi_1 = \hat{\Phi}_1 v_o l_o B$, $\Phi_2 = \hat{\Phi}_2 v_o l_o B$, $z = \hat{z} l_o$, $r = \hat{r} l_o$, $v_o = \sqrt{\beta_T \Delta T g l_o}$, $v_{(i)} = \hat{v}_{(i)} v_o$ where $i = r, \varphi, z$.

$$\left\langle \hat{f}_{rot,r}^{M} \right\rangle = \frac{\sqrt{Gr_T}}{2\,\mathrm{Re}_\omega}\left(\frac{\partial \hat{\Phi}_2}{\partial \hat{z}} - \hat{v}_r \right) \tag{4.41a}$$

$$\left\langle \hat{f}_{rot,\varphi}^{M} \right\rangle = \frac{\hat{r}}{2} - \frac{\sqrt{Gr_T}}{2\,\mathrm{Re}_\omega}\left(\frac{\partial \hat{\Phi}_1}{\partial \hat{z}} + \hat{v}_\varphi \right) \tag{4.41 b}$$

$$\left\langle \hat{f}_{rot,z}^{M} \right\rangle = -\frac{\sqrt{Gr_T}}{2\,\mathrm{Re}_\omega}\left(2\hat{v}_z + \frac{1}{\hat{r}}\hat{\Phi}_2 + \frac{\partial \hat{\Phi}_2}{\partial \hat{r}} \right) \tag{4.41 c}$$

where $Gr_T = g\beta_T \Delta T l_o^3 / \upsilon^2$ is the thermal Grashof number and $\mathrm{Re}_\omega = \omega_B l_0^2 / \upsilon$ is the rotating magnetic Reynolds number. The thermal Grashof number can be defined as the ratio of buoyancy forces to the viscous forces and it characterizes the buoyancy-induced

convection [43]. The rotating Reynolds number is the dimensionless quantity associated with rotating viscous fluid [43]. Here, g is gravitational body force, β_T is the thermal expansion coefficient, ΔT is the characteristic temperature difference, l_o is the characteristic length, υ is the kinematic viscosity and ω_B is the angular velocity of the magnetic field. For the LPD growth system under consideration, the characteristic value of the Grashof number calculated for the growth of germanium-rich Si_xGe_{1-x} single crystals is approximately 5.41 $\times 10^5$ while the rotating magnetic Reynolds number is 1.2×10^4. Since the term $\sqrt{Gr_T}/2\,\mathrm{Re}_\omega$ is 3.07×10^{-2}, it is obvious that the azimuthal force component of the rotating Lorentz force is the most dominant compared to the other two components. This is the reason most studies in the literature neglect the radial and axial force components for simplicity. However, in this present work, all three components are included in order to obtain more accurate numerical results for the LPD system.

For the calculation of the body force components, the electrical potential terms are needed. Combining Ohm's law $\mathbf{j}=\sigma_L\left(\mathbf{E}+\mathbf{v}\times\mathbf{B}\right)$ with the conservation of charge $\nabla\cdot\mathbf{j}=0$ yields the following equation for the electric potentials Φ_1 and Φ_2

$$\begin{aligned}&\sin\left(\varphi-\omega_B t\right)\left(-\frac{1}{r}\frac{\partial\Phi_1}{\partial r}-\frac{\partial^2\Phi_1}{\partial r^2}-\frac{\partial^2\Phi_1}{\partial z^2}+\frac{1}{r^2}\Phi_1-\frac{\partial v_\varphi}{\partial z}B+\frac{B}{r}\frac{\partial v_z}{\partial\varphi}\right)\\&+\cos\left(\varphi-\omega_B t\right)\left(-\frac{1}{r}\frac{\partial\Phi_2}{\partial r}-\frac{\partial^2\Phi_2}{\partial r^2}-\frac{\partial^2\Phi_2}{\partial z^2}+\frac{1}{r^2}\Phi_2-B\frac{\partial v_z}{\partial r}+\frac{\partial v_r}{\partial z}B\right)=0\end{aligned}\tag{4.42}$$

Note that both $\sin\left(\varphi-\omega_B t\right)$ and $\cos\left(\varphi-\omega_B t\right)$ cannot be zero at the same time, the only condition to satisfy the above equation is to set the terms inside the parentheses to zero. Therefore, the equation takes the following form,

$$\left(\nabla^2-\frac{1}{r^2}\right)\Phi_1=\left(\frac{1}{r}\frac{\partial v_z}{\partial\varphi}-\frac{\partial v_\varphi}{\partial z}\right)B\tag{4.43a}$$

$$\left(\nabla^2 - \frac{1}{r^2}\right)\Phi_2 = \left(\frac{\partial v_r}{\partial z} - \frac{\partial v_z}{\partial r}\right)B \tag{4.43b}$$

where the potentials are independent of the azimuthal coordinate. These equations are subject to boundary conditions which are obtained by setting the normal components of electric current to zero (the wall is an electric insulator). Setting each electric current components zero in equation (4.36), we can obtain the following boundary conditions:

For vertical side walls: $\partial\Phi_1 / \partial r = 0, \partial\Phi_2 / \partial r = 0,$

For dissolution and growth interfaces: $\partial\Phi_2 / \partial z = 0, \partial\Phi_1 / \partial z = \omega_B Br.$

4.4 Dimensionless Analysis

It is a common practice to express the transport equations in dimensionless forms to determine the sensitivity of the system to changes in the transport modes (such as, conduction, convection and diffusion). Dimensionless analysis for the application of magnetic field in crystal growth is also used to develope a general understanding of the relation between flow parameters and the applied magnetic field. The non-dimensionalization was done using the following "dimensionless quantities"

$$\hat{x} = \frac{x_i}{l_o},\ (i = r,\varphi,z),\ \hat{\mathbf{v}} = \frac{\mathbf{v}}{v_o},\ \hat{t} = t\frac{v_o}{l_o},\ v_o = \frac{\upsilon}{l_o}, or\ v_o = \sqrt{\beta_T \Delta T g l_o}$$

$$\hat{p} = \frac{p - p_o}{l_o v_o^2}, or\ \hat{p} = \frac{(p - p_o)}{\mu v_o / l_o},\ \hat{\nabla} = l_o\nabla,\ \frac{\partial}{\partial\hat{t}} = \frac{l_o}{v_o}\frac{\partial}{\partial t},\ \hat{T} = \frac{T - T_o}{T_1 - T_o}, \tag{4.44}$$

$$\hat{c} = \frac{c - c_o}{c_1 - c_o},\ v_{(i)} = \hat{v}_{(i)} v_o,\ i = r,\varphi,z,\ \hat{\mathbf{B}} = \frac{\mathbf{B}}{B_o},\ \hat{\mathbf{f}}_{st}^M = \frac{\mathbf{f}_{st}^M}{\sigma B_o^2 v_o},\ \hat{\mathbf{f}}_{rot}^M = \frac{\mathbf{f}_{rot}^M}{\sigma\omega_o l_o B_o^2}$$

The dimensionless forms of field equations are obtained as follows:

Mass Balance

$$\left(\nabla \cdot \mathbf{v}\right) = 0 \tag{4.45}$$

$$\left(\hat{\nabla} \cdot \hat{\mathbf{v}}\right) = 0 \tag{4.46}$$

Momentum Balance

$$\rho\left(\frac{\partial \mathbf{v}}{\partial t} + \left(\mathbf{v} \cdot \nabla\right)\mathbf{v}\right) = -\nabla p + \nabla \cdot \left(\mu \nabla \mathbf{v}\right) + \mathbf{f}^{B} + \mathbf{f}_{st}^{M} + \mathbf{f}_{rot}^{M} \tag{4.47}$$

where $\mathbf{f}^{B}$ is the body force per unit volume and defined through using the well known Boussinesq approximation ($\mathbf{f}^{B} = -\rho g\left[1 - \beta_{T}\left(T - T_{o}\right) - \beta_{c}\left(c - c_{o}\right)\right]\mathbf{e}_{z}$), and $\mathbf{f}_{st}^{M}$ and $\mathbf{f}_{rot}^{M}$ are the magnetic body forces per unit volume due to a static vertical and rotating magnetic fields, respectively.

$$\begin{aligned}\rho\left(\frac{\partial \mathbf{v}}{\partial t} + \left(\mathbf{v} \cdot \nabla\right)\mathbf{v}\right) = &-\nabla p + \nabla \cdot \left(\mu \nabla \mathbf{v}\right) \\ &+ \rho g \beta_{T}\left(T - T_{o}\right)\mathbf{e}_{z} + \rho g \beta_{c}\left(c - c_{o}\right)\mathbf{e}_{z} + \mathbf{f}_{st}^{M} + \mathbf{f}_{rot}^{M}\end{aligned} \tag{4.48}$$

Substituting associated scaling factors in equation (4.48) yields,

$$\begin{aligned}\left(\frac{\partial \hat{\mathbf{v}}}{\partial t} + \left(\hat{\mathbf{v}} \cdot \hat{\nabla}\right)\hat{\mathbf{v}}\right) = &-\hat{\nabla}\hat{p} + \left(\frac{\mu}{l_{o}\left(g\beta\Delta T l_{o}\right)^{1/2}\rho}\hat{\nabla}^{2}\hat{\mathbf{v}}\right) + \frac{g\beta_{T}l_{o}\left(T_{1} - T_{o}\right)}{\left(g\beta_{T}\Delta T l_{o}\right)}\hat{T}\,\mathbf{e}_{z} \\ &+ \frac{g\beta_{c}l_{o}\left(c_{1} - c_{o}\right)}{\left(g\beta\Delta T l_{o}\right)}\hat{c}\,\mathbf{e}_{z} + \sigma B_{o,st}^{2}\frac{l_{o}}{l_{o}}\frac{\upsilon}{\upsilon}\frac{l_{o}}{\rho\sqrt{\beta_{T}\Delta T g l_{o}}}\hat{\mathbf{f}}_{st}^{M} + \frac{l_{o}}{\rho v_{0}^{2}}\frac{\sigma}{2}B_{o,rot}^{2}\omega_{o}l_{o}\hat{\mathbf{f}}_{rot}^{M}\end{aligned} \tag{4.49}$$

The multiplication factors in front of dimensionless quantities in equation (4.49) are identified as thermal Grashof number ($Gr_{T} = g\beta_{T}\Delta T l_{o}^{3}/\upsilon^{2}$), solutal Grashof number

($Gr_c = g\beta_T \Delta c l_o^3 / \upsilon^2$), Hartman number ($Ha = B_o l_o \sqrt{\sigma_L / \rho\upsilon}$) and magnetic Taylor number ($Ta_m = \sigma_L \omega_B B_o^2 l_o^4 / 2\rho\upsilon^2$). Therefore, equation (4.49) becomes,

$$\left(\frac{\partial \hat{\mathbf{v}}}{\partial t} + \left(\hat{\mathbf{v}} \cdot \hat{\nabla}\right)\hat{\mathbf{v}}\right) = -\hat{\nabla}\hat{p} + \sqrt{\frac{1}{Gr}}\hat{\nabla}^2\hat{\mathbf{v}} + \hat{T}\mathbf{e}_z + \frac{Gr_c}{Gr_T}\hat{c}\mathbf{e}_z + Ha^2\frac{1}{\sqrt{Gr_T}}\hat{\mathbf{f}}_{st}^M + \frac{2Ta_m}{Gr_T}\hat{\mathbf{f}}_{rot}^M \tag{4.50}$$

Energy Balance

$$\frac{\partial T}{\partial t} + (\mathbf{v} \cdot \nabla)T = \frac{k_L}{\rho_L \gamma_L}\nabla \cdot (\nabla T) \tag{4.51}$$

Following the same procedure used above with the usage of dimensionless parameters, equation (4.51) can be expressed in its dimensionless form as,

$$\left(\frac{\partial \hat{T}}{\partial \hat{t}} + \left(\hat{\mathbf{v}} \cdot \hat{\nabla}\right)\hat{T}\right) = \frac{1}{\sqrt{Ra_T \,\mathrm{Pr}}}\hat{\nabla}^2\hat{T} \tag{4.52}$$

where $Ra_T = g\beta_T \Delta T l_o^3 / \upsilon\kappa$ is the thermal Rayleigh number, $\mathrm{Pr} = \upsilon / \kappa$ is the Prandtl number and $\kappa = \dfrac{k_L}{\rho_L \gamma_L}$ is thermal diffusivity,.

Mass Transport

$$\frac{\partial c}{\partial t} + \left(\mathbf{v} \cdot \nabla\right) c = D_{L,Si}\nabla \cdot (\nabla c) \tag{4.53}$$

$$\left(\frac{\partial \hat{c}}{\partial \hat{t}} + \left(\hat{\mathbf{v}} \cdot \hat{\nabla}\right)\hat{c}\right) = \frac{1}{Sc\sqrt{Gr_T}}\hat{\nabla}^2\hat{c} \tag{4.54}$$

where $Sc = \upsilon / D$ is the Schmidt number.

In table 4.3, the formulations of dimensionless numbers used in this work are presented along with their physical meaning.

Table 4.5- Summary of Dimensionless numbers used in this work and their definition [43, 44].

Dimensionless numbers	**Definition**	**Formulation**
Thermal Grashof Number	A measure of the strength of the buoyancy convection driven by thermal gradients	$Gr_T = g\beta_T \Delta T l_o^3 / \upsilon^2$
Solutal Grashof Number	A measure of the strength of the buoyancy convection driven by solutal gradients	$Gr_c = g\beta_C \Delta c l_o^3 / \upsilon^2$
Hartmann Number	The ratio of the magnetic force to the viscous force. (Characterizes the steady magnetic field).	$Ha = B_{st} l_o \sqrt{\sigma_L / \rho\upsilon}$
Prandtl Number	The ratio of momentum diffusivity to thermal diffusivity.	$\mathrm{Pr} = \upsilon / \kappa$
Thermal Rayleigh Number	The ratio of buoyant energy release to viscous and thermal energy dissipation.	$Ra_T = g\beta_T \Delta T l_o^3 / \upsilon\kappa$
Schmidt Number	The ratio of momentum diffusivity to solutal diffusivity.	$Sc = \upsilon / D$
Magnetic Taylor Number	The ratio of Lorentz force to viscous force. Describes the Lorentz-force amplitude of the rotating magnetic field action.	$Ta_m = \sigma_L B_{rot}^2 \omega_B l_0^4 / 2\rho\upsilon^2$
Magnetic Reynolds Number	Ratio of the fluid flux to the magnetic diffusivity. It is the measure of the effect of the flow on the magnetic field.	$Re_m = \eta_0 \sigma_L v_0 l_0$
Rotating Reynolds Number	The dimensionless quantity associated with rotating viscous fluid	$Re_\omega = \omega_B l_o^2 / \upsilon$

CHAPTER 5

NUMERICAL SIMULATION MODEL

In this chapter, a three-dimensional numerical simulation model for the growth of Si_xGe_{1-x} single crystals by Liquid Phase Diffusion under static vertical and rotating magnetic fields is presented. In this study, the governing equations describing the fluid flow, heat and mass transport are numerically solved using the finite volume-based CFX-4.4 software package of AEA Technology [46]. In the numerical simulation, several user-defined subroutines have been developed to move the grid in time, to implement complex thermal boundary conditions and magnetic body force terms in the momentum balance equation, and to solve additional scalar transport equations for calculating electric potential distribution in the melt. In addition, a command file is produced to define the physical properties of the fluid and surrounding solids, numerical methods used, model topology, convergence criteria, and equation solvers.

In the present simulation, first the effect of a static vertical magnetic field is investigated. The application of a rotating magnetic field on the present system is then simulated to study the effect of forced convection in the liquid solution.

5.1 Computational Procedure

The computational procedure starts with creation of a 3D geometry for the present LPD system. The 3D geometry is constructed using CFX multi-block features. A Multi-block grid consists of several blocks glued together in such a way that no unmatched nodes are allowed [31]. With the multi-block structure, very complex geometries can be

successfully treated. As can be seen from the Figure 5.1, the solution domain is divided into sub-domains, and each sub-domain is divided into blocks. The computational domain for the present model consists of 3 sub-domains and 15 blocks. Figure 5.1 shows the block structure of the computational domain.

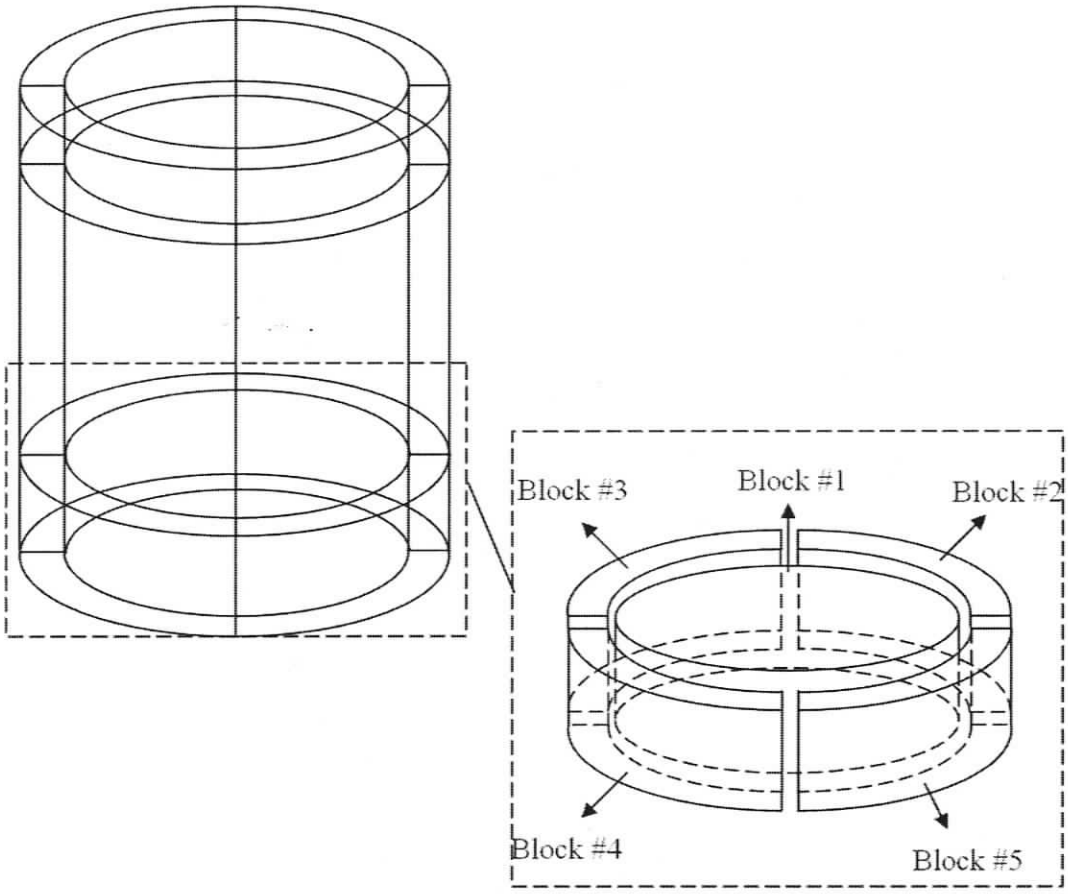

Figure 5.1- Computational domain and its block structure

After creating the 3-D geometry, the appropriate grid type and mesh size are defined. The discretization of the computational domain is chosen as the body-fitted grid. The computational mesh sizes are selected for the substrate, liquid domain, source and the quartz ampoule, respectively, as 18,000, 54,000, 7200 and 42,240. The selected number of grid nodes were tested and we found that simulation results are no longer mesh size dependent.

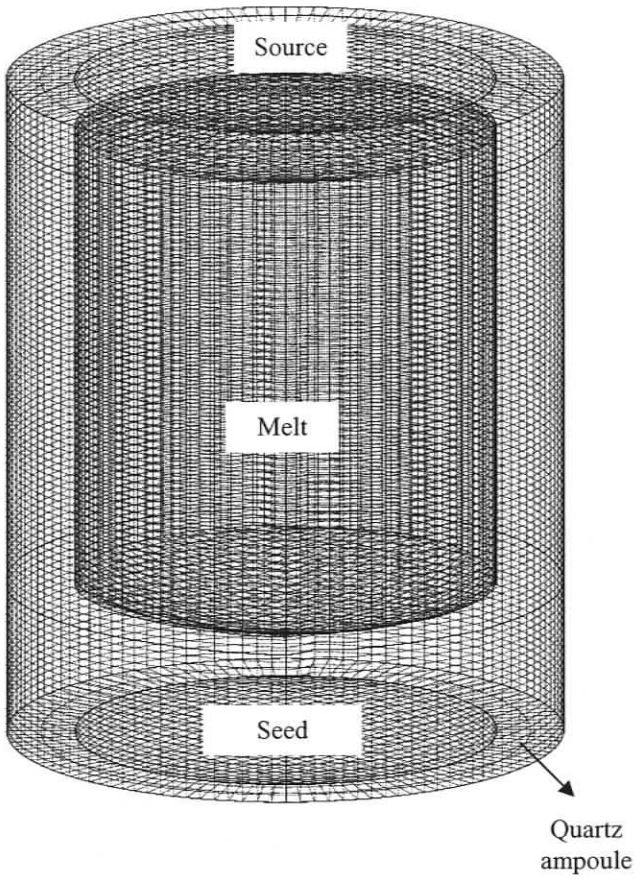

Figure 5.2- Mesh used in 3-D simulation

Next, a command file was created to define the physical properties (heat and mass transfer, and scalar parameters etc.), transient parameters (time steps and time values etc.) and solver parameters (discretization scheme, under relaxation factors, equation solvers etc.).

After forming the command file, several user defined subroutines such as USRBCS, USRBF, USRGRD, and USRSRC were produced in order to implement complex boundary conditions and body force terms, to move the grid in time, and to solve the electric potential terms in the liquid domain.

Then, the computational procedure can be applied to solve the discretized governing equations for several time steps. The user can specify the time steps as either fixed or

adaptive time stepping. In the present model, the fixed time stepping option is chosen. Next, the simulation results are post processed. Figure 5.3 illustrates the computational procedure steps for the present numerical simulation.

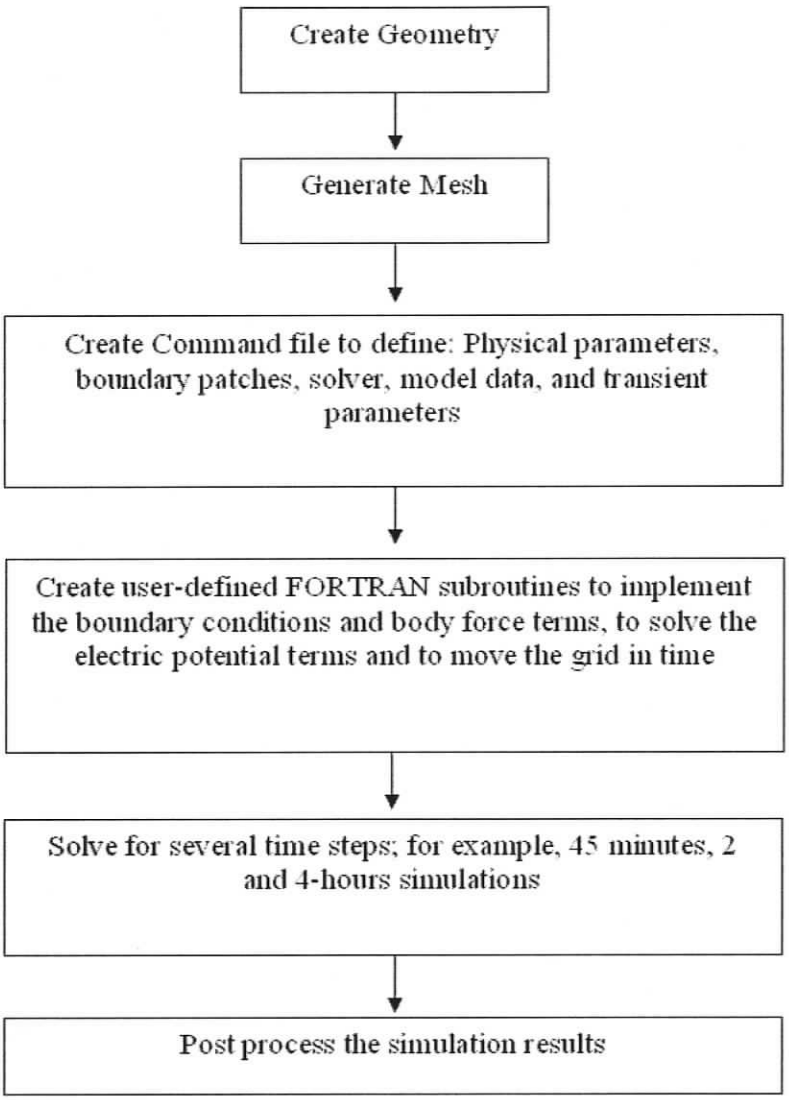

Figure 5.3- Flow chart of computational procedure

5.2 Solution Algorithm

In this simulation, the three-dimensional time dependent governing equations are numerically solved using the CFX-4.4 equation solver. Since CFX is a finite volume based program, all transport equations are discretized based on finite volume method into a system of algebraic equations. In the finite volume method, the domain is divided into a number of control volumes, and then each partial differential transport equation is integrated over each control volume, which gives their linear forms. Then, these equations are solved by an iterative algorithm. The iteration process is divided into two levels: inner iteration to solve for spatial coupling for each variable, and outer iteration to solve for couplings between variables. Thus, each variable is taken in sequence by keeping the rest fixed. A discrete transport equation for a particular variable is generated for every finite volume cell within the computational domain. Then the linear transport equation for that variable is handed over to a linear equation solver, which is set by the user or by default [46].

The solution of the field equations starts with defining initial guesses and boundary conditions. First the momentum equations are solved. The momentum equations are treated differently due to the unknown pressure terms in them. If the pressure terms are known, the velocity field can be computed to satisfy the continuity equation. Therefore, the pressure and velocity coupling are treated using the default SIMPLEC (semi implicit method for pressure linked equations-corrected) pressure correction algorithm. In this algorithm, an initial pressure value is assumed for all grid points. Using the temporary pressure value, the discretized momentum equations are solved, which gives a temporary velocity field. This velocity profile will not satisfy the continuity equation since the pressure term is arbitrarily chosen. Therefore, using the residual and continuity equation, the pressure term will be corrected until the solution converges. The computed velocity fields are then used to calculate the thermal and concentration profiles in the liquid zone, which are coupled with the linear momentum equations through the flow field.

For the case of treating the advection terms in the governing equations, the Finite Difference scheme has to be selected properly in order to obtain an accurate solution procedure. Therefore, in this numerical simulation all advection terms are treated using the *HYBRID* differencing scheme. Hybrid differencing is a combination of central and upwind differencing. If the Peclet number is less than 2 the central differencing is used otherwise upwind differencing is used. The HYBRID differencing scheme is first- order accurate; however it is better than more accurate schemes because it is faster and more robust.

The time dependent parts of the field equations are treated by employing a fully implicit *backward difference time stepping* procedure [46]. If the equations have the form of

$$\frac{\partial \phi}{\partial t} = F(\phi) \tag{5.1}$$

then, the discretised form by backward time stepping is

$$\frac{\phi^n - \phi^{n-1}}{\Delta t} = F(\phi^n) \tag{5.2}$$

The electric potential terms in the magnetic body force terms of linear momentum equations have the form of a diffusion transport equation with the source term being the spatial derivatives of velocity components. It is therefore possible to describe these equations in CFX-4.4 as a scalar transport equation under the steady state and no convection conditions. The source term in this scalar transport equation is treated by developing a user-defined subroutine. Regarding the implementation of magnetic body force terms in CFX, they can be included in either body force or source term subroutines. The latter way is used with special care by properly linearizing the source terms since the former one created serious convergence problems.

In CFX-4.4, there are a number of ways in which the solution process may be stopped either completely or for the current time step of transient problem. The stopping or convergence criteria can be set in several ways. One of the ways is to set a fixed number of iteration. The number of iterations required might be from a few hundred to several thousands. The number of iterations can be adjusted, depending on the accuracy desired and in turn reduction in mass source residuals, by using a user-defined FORTRAN subroutine. The user can set a tolerance for the mass residual. The mass residual is the sum of the absolute values of the net mass fluxes into or out of every cell in the flow. CFX tests the error to see if the mass residual has fallen below some limit set by the user. In this work, after a number of trial runs, the number of iterations (700-800) for each time step of the transient calculations are selected. The summary of the solution procedure for the present numerical simulation is given in Figure 5.4.

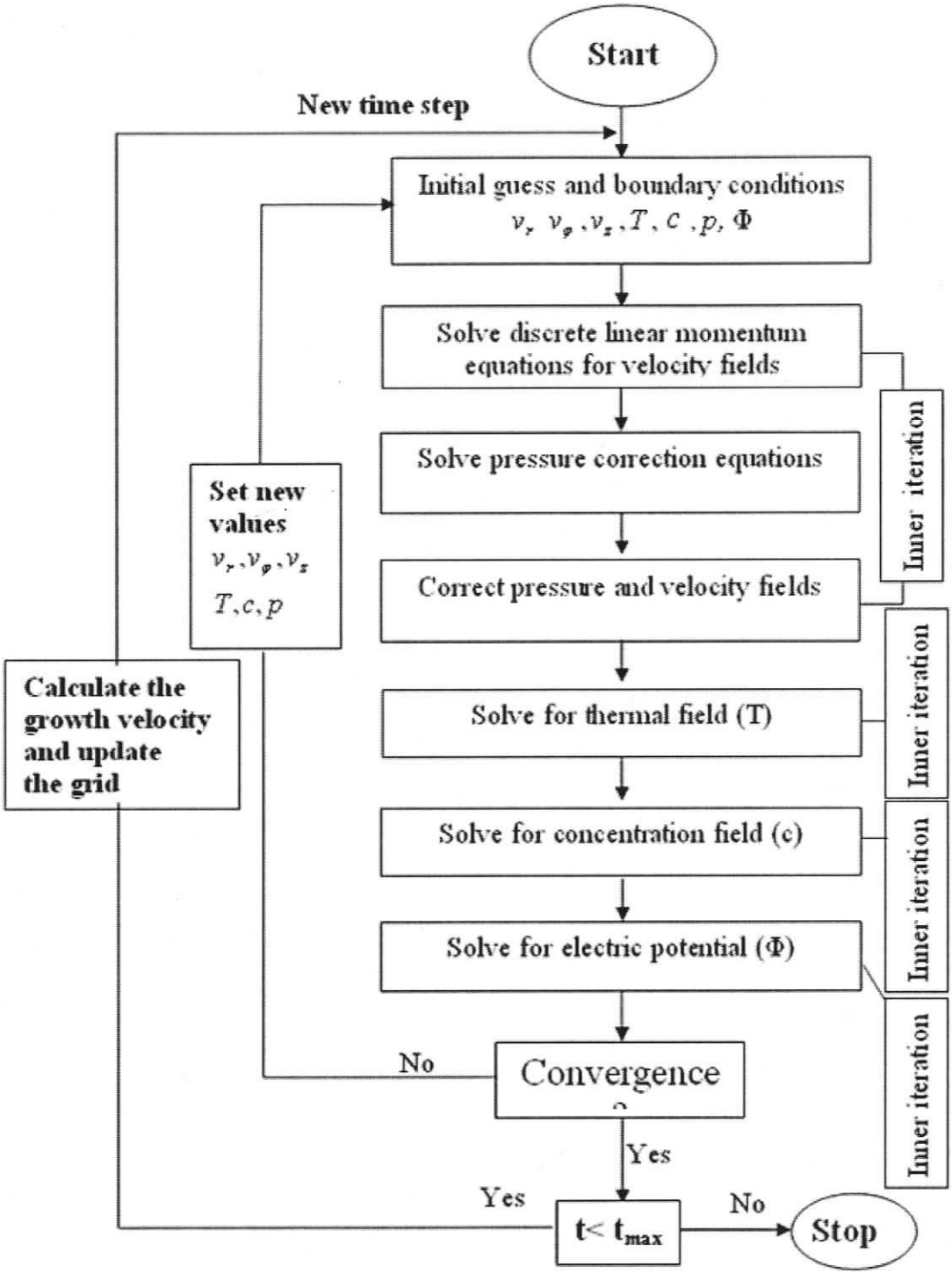

Figure 5.4- Flow chart of solution algorithm

CHAPTER 6

RESULTS AND DISCUSSIONS

In this section, we present our simulation results under both static vertical and rotating magnetic fields. In both cases, we conducted simulations with and without the contribution of electric potential to account for the effect of electric potential on the flow field. The effect of magnetic field on the temperature field was not presented because the comparison of the simulated temperature profiles in the liquid for different magnetic field strengths (for both static vertical and rotating magnetic fields) revealed that the flow field does not have a strong influence on the thermal field. This can be attributed to the very small Prandtl number (≈ 0.0075) for the Ge-rich *Si-Ge* mixture, which indicates that heat transport within the liquid domain is mainly due to conduction with very little contribution of convection.

6.1 Numerical Simulation Results for a Static Vertical Magnetic Field

6.1.1 Effect of a Static Magnetic Field on the Flow Field

Figure 6.1 presents the computed velocity profile without magnetic field at 1 hour of growth on the vertical plane ($\varphi = \pi$) of the computational domain. The flow field is given in terms of the strength of the velocity vector, i.e. $U = \sqrt{v_r^2 + v_\varphi^2 + v_z^2}\ (m/s)$. As can be seen from Figure 6.1, the flow field has two main convection cells near the growth

interface. In the rest of the liquid domain, convection is very weak and not noticeable numerically. This is mainly because the addition of solute (*Si*) species into the solution gives rise to a density gradient that acts like a stabilizer and consequently suppresses the convection [41]. The convective cell on the right circulates in the clockwise direction, thereby pushing the solution downward along the crucible wall and upward along the axis of symmetry, while the other cell on the left rotates anti-clockwise direction. These toroidal convective cells cause mixing in the liquid solution, resulting in the accumulation of fluid particles near the crucible wall (vertical boundaries), and in turn lead to the formation of large vertical concentration gradients in this region. Therefore, such an uncontrolled mixing is not desirable since it may produce local non-uniformities in concentration and growth velocity along the radial direction. Drastic variations in growth velocity due to inhomogeneous mass transport to the growth interface may facilitate interface break down and in extreme cases, multi grain growth.

The computed flow strengths under four magnetic field levels are presented in Figures (6.2-6.5). As seen, the magnetic field strength of 0.05 T (relatively weak) decreases the strength of the convection, yet the cellular form of the convective cells is not broken down completely. As the magnetic field strength increases, the convection cells expand along the radial direction and shrink in the vertical direction. Simulation results show that approximately a field of 0.2-0.3 Tesla is sufficient to suppress convection significantly.

Figure 6.6 (a-b) shows the computed velocity field at the magnetic field intensity level of 0 T and 0.2 T, respectively. In order to see the effect of vertically applied static magnetic field on the flow field quantitatively, the radial-meridional velocity vector components are plotted on the left side of Figure 6.6 (a-b) while the azimuthal velocity component (contour) is presented on the right. As seen from the figures the azimuthal velocity is very weak and the meridional flow is dominant in the solution. Besides, comparison of the meridional flow in those two figures clearly shows the suppression of convection. The flow strength for different levels of static magnetic strengths at a horizontal plane near the growth interface is given in Figures (6.7-a-f). These figures show that with the

application of a vertical magnetic field, more uniform flow field is obtained along the centre line since the flow fluctuation is suppressed.

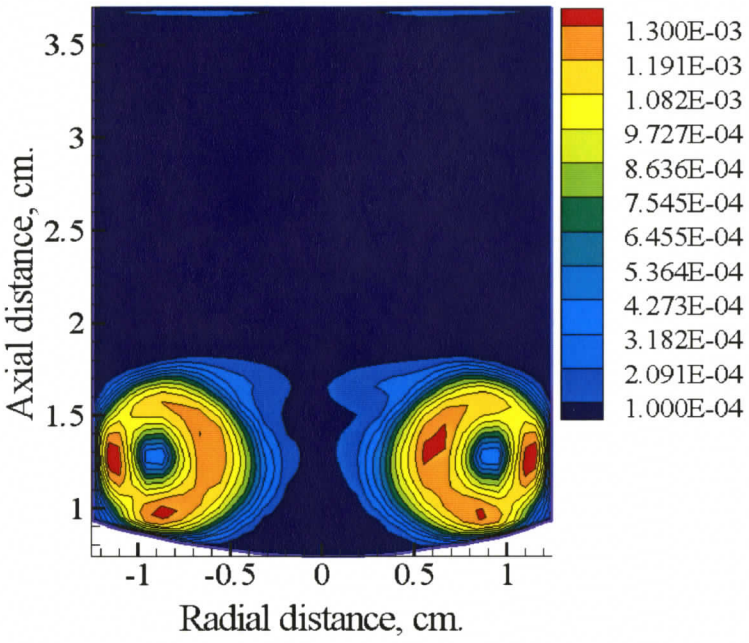

Figure 6.1- Computed flow strength ($U = \sqrt{v_x^2 + v_r^2}\ m/s$) on the vertical plane without magnetic field at 1 hour of growth

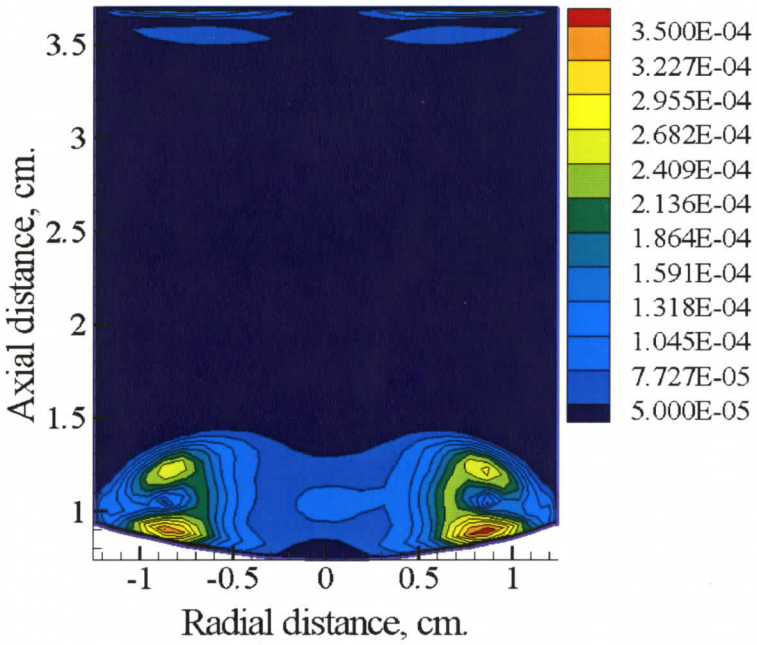

Figure 6.2- Computed flow strength ($U = \sqrt{v_x^2 + v_r^2}\ m/s$) on the vertical plane ($\varphi = \pi$) with 0.05 T static magnetic field intensity at 1 hour of growth

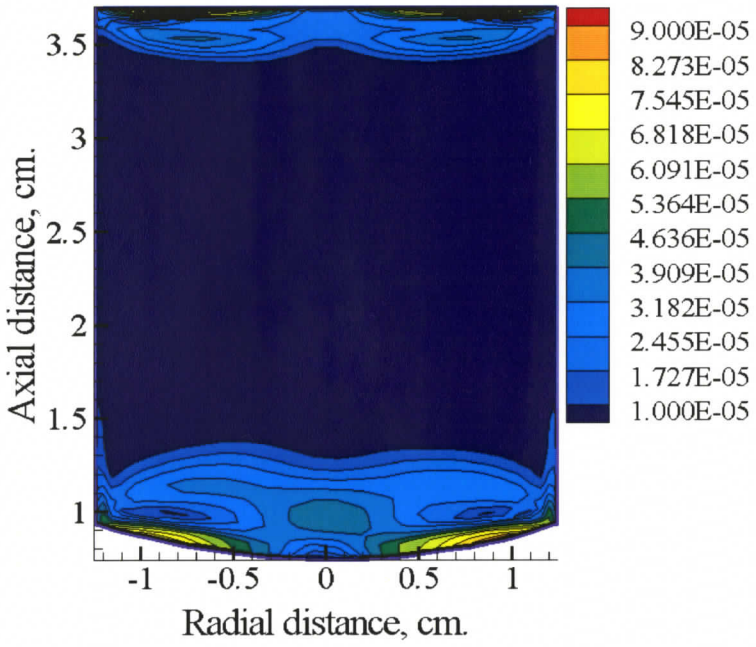

Figure 6.3- Computed flow strength ($U = \sqrt{v_x^2 + v_r^2}\ m/s$) on the vertical plane ($\varphi = \pi$) with 0.1 T static magnetic field intensity at 1 hour of growth

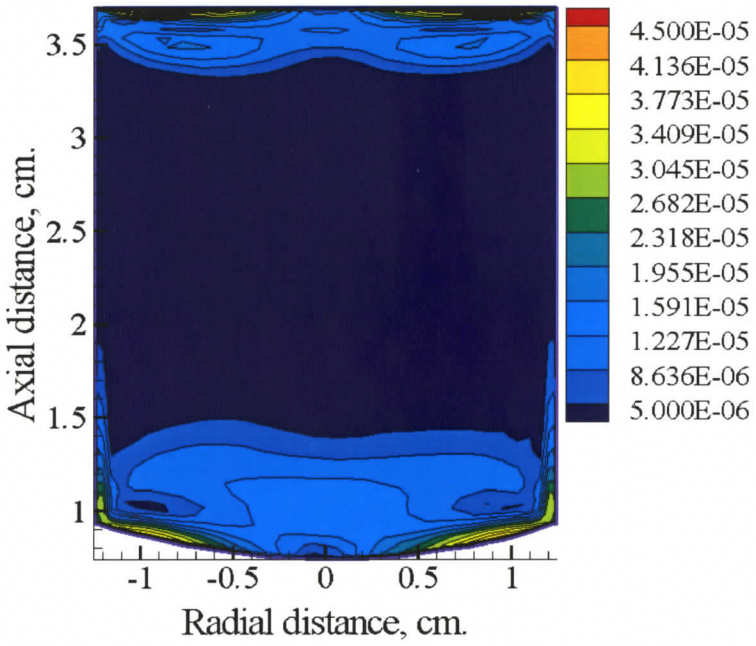

Figure 6.4- Computed flow strength ($U = \sqrt{v_x^2 + v_r^2}\ m/s$) on the vertical plane ($\varphi = \pi$) with 0.2 T static magnetic field intensity at 1 hour of growth

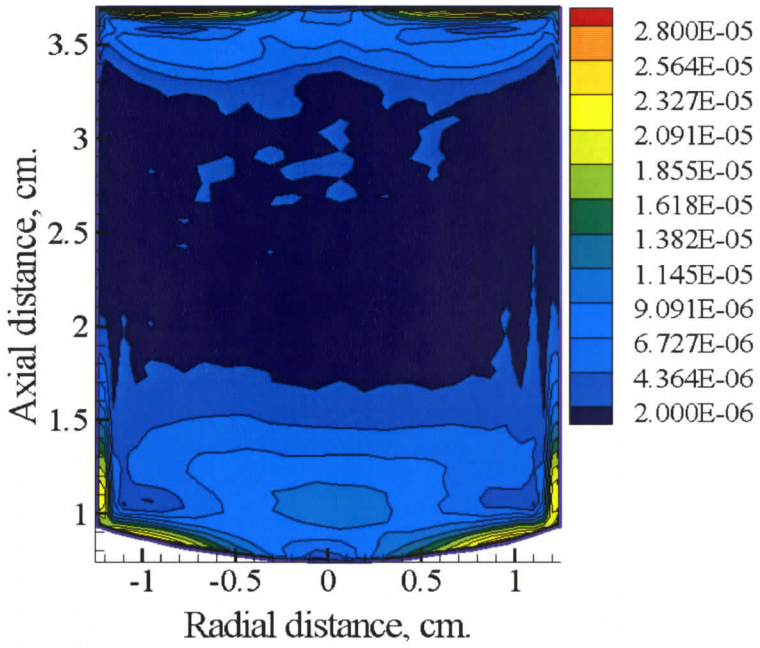

Figure 6.5- Computed flow strength ($U = \sqrt{v_x^2 + v_r^2}\ m/s$) on the vertical plane ($\varphi = \pi$) with 0.3 T static magnetic field intensity at 1 hour of growth

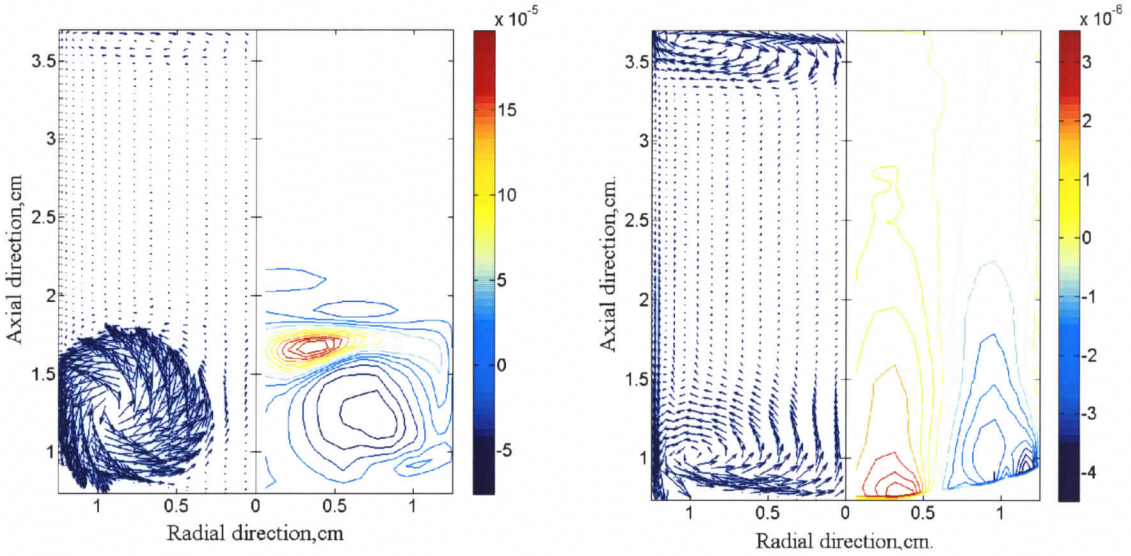

(a)(B=0 T) (b)(B=0.2 T)

Figure 6.6 (a-b) - Radial-meridional velocity field vector (left) and azimuthal velocity field (right) on the vertical plane ($\varphi = \pi$) at B=0 T and B=0.2 T, and t=1h.

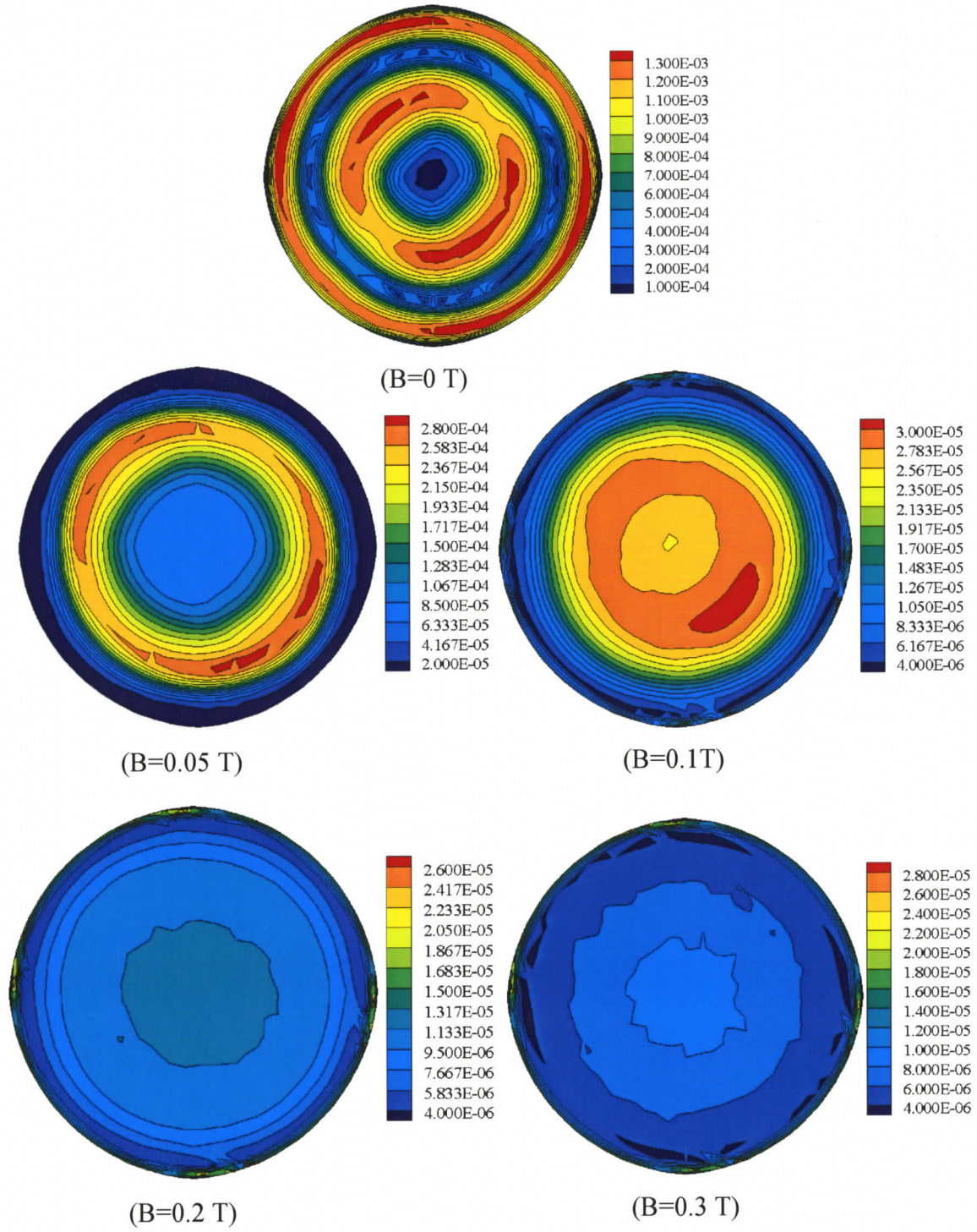

Figure 6.7- Computed flow fields from a horizontal plane at a distance of 6 mm from the growth interface at t=1h with the application of different static magnetic field intensities.

In this numerical simulation, the effect of electric potential is also investigated. It was found that for the case of a vertical magnetic field there is no considerable potential built up in the liquid solution, in other words, the effect of electric potential on the flow structure is insignificant (see Figure 6.8). The figure also shows the variation of maximum flow strength versus the Hartmann number. The maximum flow strength in the liquid solution decreases with the increasing value of the Hartmann number. For the present study, the flow is stable up to *Ha*=60. As the Hartmann number increases further, the flow becomes unstable; however, the maximum velocity of the flow still decreases. Since the Hartman number appears squared in the dimensionless form of the momentum equation, the flow strength will be scaled with the square of the applied magnetic field. As can be seen from the figure the flow velocity decreases nearly in accordance with Ha^{-2}

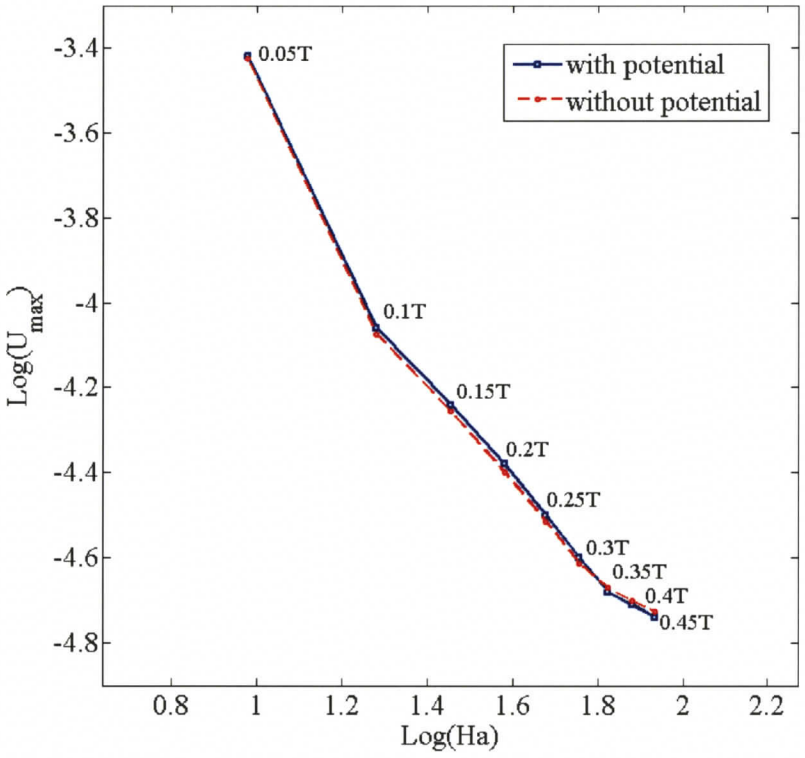

Figure 6.8- Variation of maximum flow strength with the Hartman number with and without electric potential contribution

6.1.2 Effect of a Static Magnetic Field on the Concentration Field

Concentration distributions in silicon mass fraction are presented in Figures (6.9-6.14). Figure 6.9 represents the concentration profile without magnetic field at 1 hour of the growth. As can be seen from the figure, the region with weak convection (upper region) exhibits diffusion like solute distribution while the region where the convection is strong (lower region) shows a totally distinct concentration profile as compared to the upper region. With the application of a static vertical magnetic field, one would expect to see more diffusion-like solute distribution near the growth interface since the magnetic field suppresses the convection hence reduces the convective mass transport. In Figures (6.12-6.13), iso-concentration lines near the growth interface are showing diffusion-like solute distribution, which means that the growth process becomes diffusion dominant.

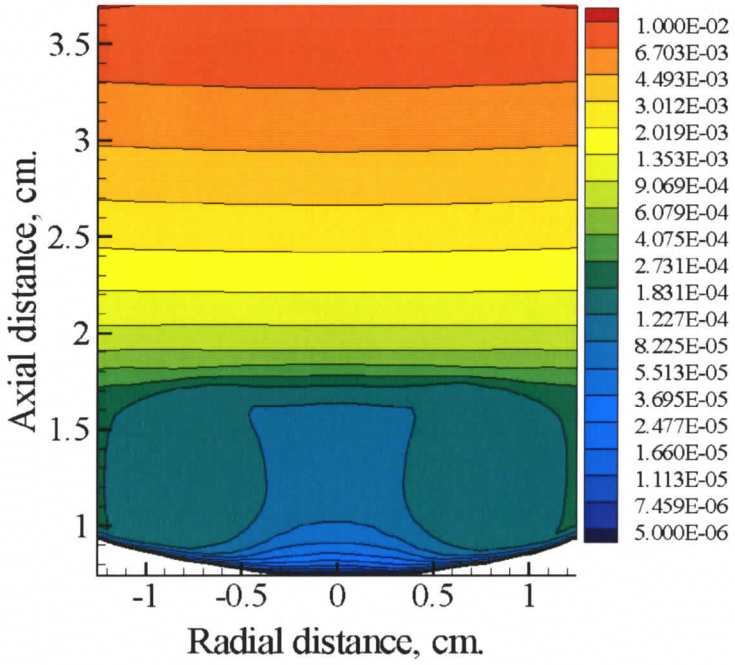

Figure 6.9- (a) Silicon concentration distribution (in mass fraction) on the vertical plane ($\varphi = \pi$) without magnetic field at 1 hour of the growth.

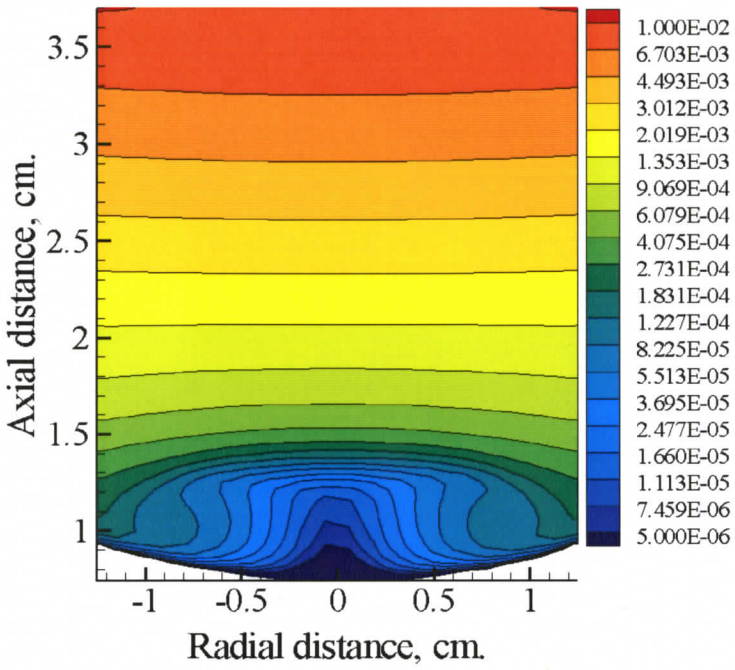

Figure 6.10- Silicon concentration distribution (in mass fraction) on the vertical plane ($\varphi = \pi$) at B=0.05 T and t=1h.

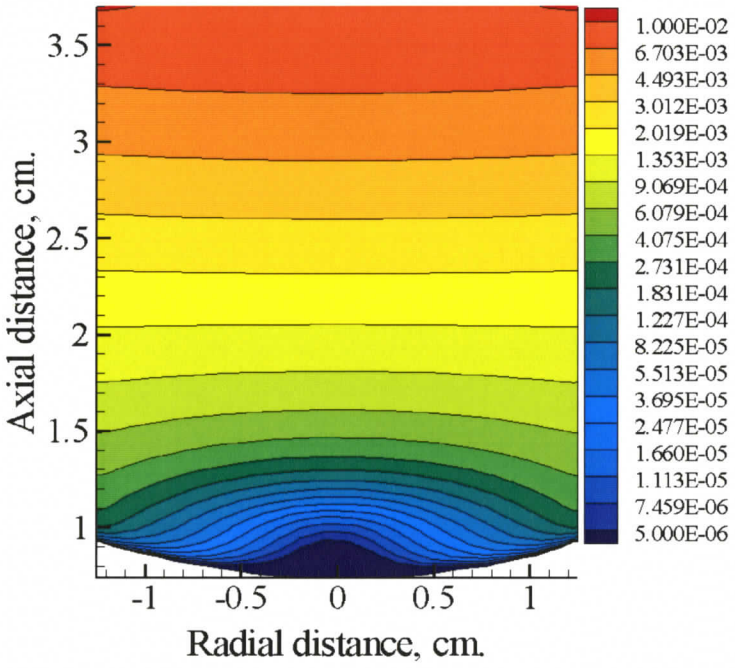

Figure 6.11- Silicon concentration distribution (in mass fraction) on the vertical plane ($\varphi = \pi$) at B=0.1 T and t=1h.

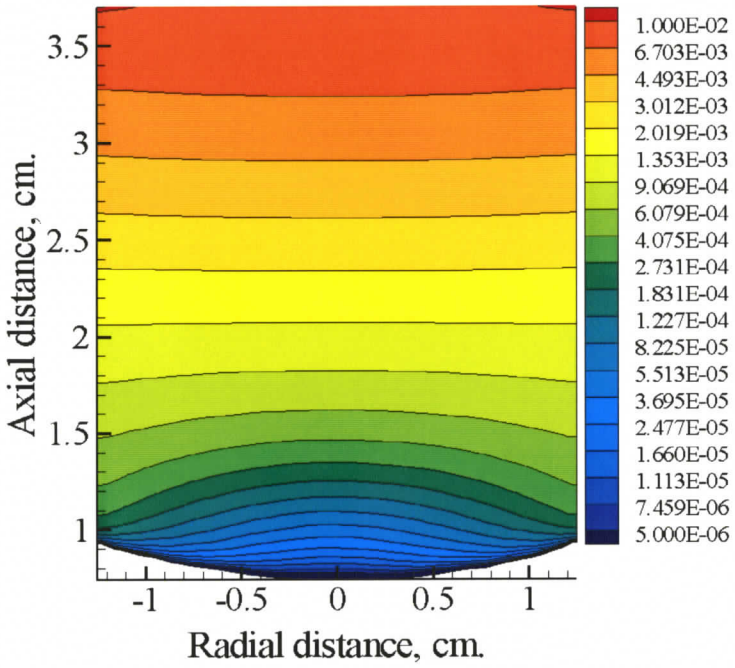

Figure 6.12- Silicon concentration distribution (in mass fraction) on the vertical plane ($\varphi = \pi$) at B=0.2 T and t=1h.

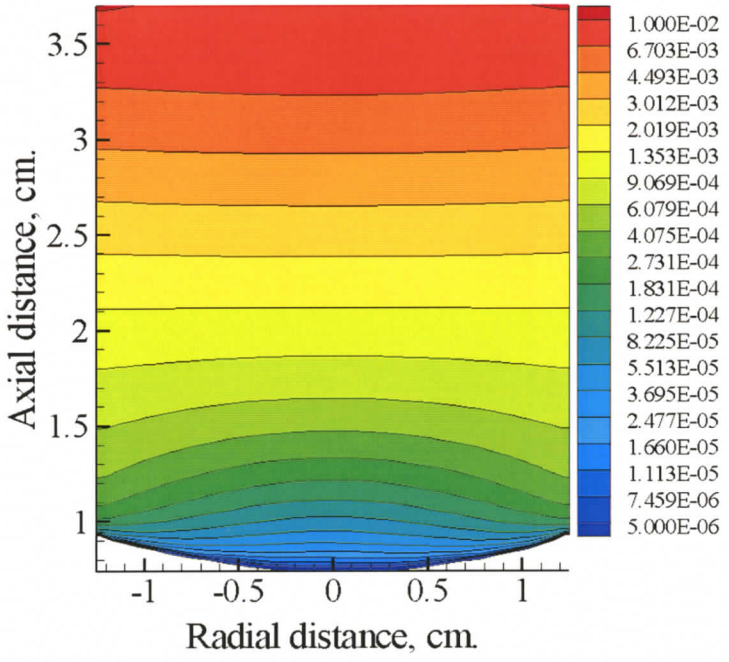

Figure 6.13- Silicon concentration distribution (in mass fraction) on the vertical plane ($\varphi = \pi$) at B=0.3 T and t=1h.

6.1.3 Effect of a Static Magnetic Field on the Growth Interface Shape

In LPD growth of $Si_x\ Ge_{1-x}$, the crystal growth velocity (see Eqs. (4.10)[3]), consequently, the shape of the growth interface is controlled mainly by the solute gradient normal to the growth interface along the radial direction. To account for the effect of a static vertical magnetic field on the interface shape, one may look at the variation of the solute gradient at the growth interface as shown in Figure 6.14.

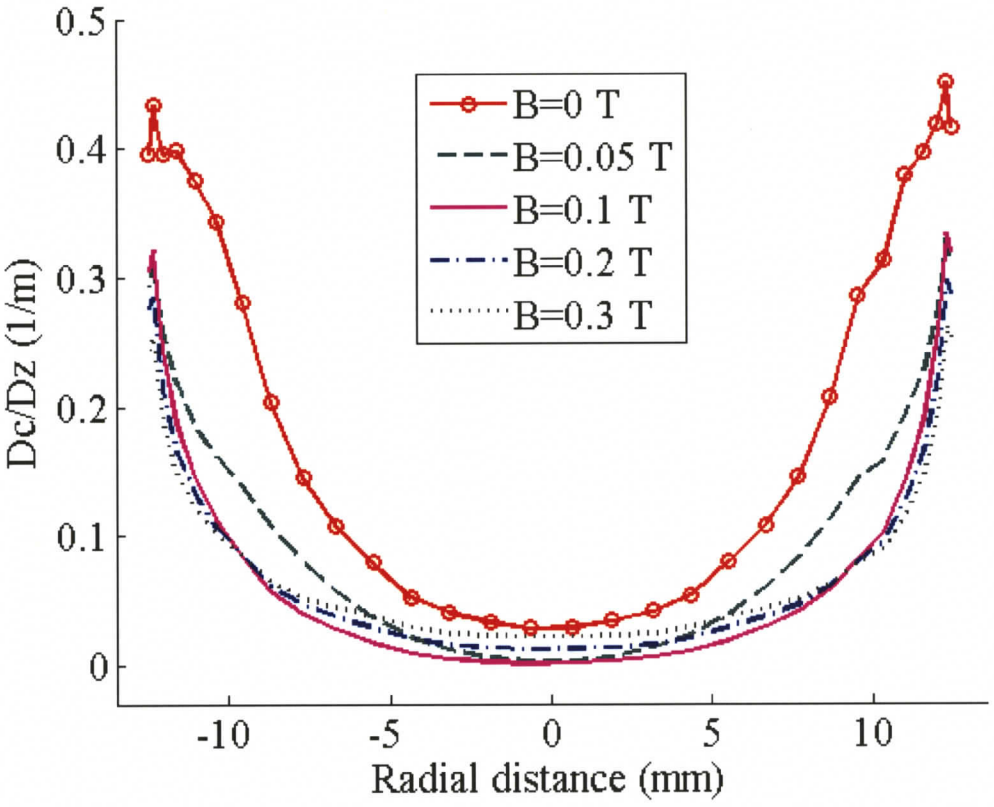

Figure 6.14- Radial variation of solute (*Si*) gradient at the growth interface in the growth direction with various static magnetic field intensities.

In the case of no magnetic field, we see a very steep variation from the crucible walls towards the centre (symmetry axis) of the liquid domain. This can be attributed to transport patterns of fluid particles by convection cells (see Figure 6.1). The application of a static vertical magnetic field affects these patterns. As the natural convection is

suppressed further with the increase of the magnetic field intensity, the radial solute gradient decreases leading to slight flattening of the interface shape as the growth progresses. However, static vertical magnetic field does not provide the desired effect to obtain a radially uniform solute gradient. One may therefore conclude that the application of the static vertical magnetic field for the present LPD system is not sufficient to achieve a flat growth interface for a prolonged growth.

6.2. Numerical Simulation Results for a Rotating Magnetic Field

6.2.1 Effect of an RMF on the Flow Field

The effect of electromagnetic stirring on fluid flow can easily be seen from the velocity profile of the liquid solution presented under different rotating magnetic field strengths. In Figure 6.15, we see the evaluation of the fluid flow at 2 hours of the growth without magnetic field. With the application of RMF, the flow patterns change since the azimuthal body force component of the applied rotating magnetic field creates a stirring effect in the solution. Figures (6.16-6.22) show the stirring action of RMF in the liquid solution. With the application of a 0.5 mT (millitesla) RMF (Figure 6.16), we see that two new large convection cells (due to forced convection) emerge in the upper part of the liquid zone. These cells circulate in the opposite directions; the left one anti-clockwise while the right one clockwise. They gain strength with the increasing RMF intensity and begin to merge with those of the natural convection (buoyancy induced cells near the growth interface) as seen in Figures (6.17-6.20). At B=2 mT level, the flow cells almost become two new cells that span across the entire solution domain. This new flow structure under the effect of a rotating magnetic field improves mixing in the liquid significantly. The computed flow structure is stable up to about 3 mT. However, starting at the level of 3 mT, a series of local vortex formation near the vertical crucible wall takes place. Above the 4 mT level, the flow becomes unstable.

Figure 6.21 shows the effect of RMF on the flow field more quantitatively. The radial-meridional velocity vector components are plotted on the left side, while the azimuthal velocity components (contours) are plotted on the right side. Results show that the azimuthal velocity component is dominant since the comparison of the flow strength and the azimuthal velocity contours show similar outputs. Comparison of Figure 6.6a and Figure 6.21 also reveals that with the application of RMF, flow structure becomes more uniform. The flow strength with different RMF intensities at a horizontal plane near the interface is given in Figures (6.22b-f). The improvement in mixing obtained in the liquid zone under the effect of a rotating magnetic field can clearly be seen in these figures.

Results of the present study suggest that rotating magnetic field levels between 2 and 3 mT appear to be optimum for the present LPD growth system. Field levels up to this optimum values may provide the desired mixing in the solution. However, above 3 mT, the application of RMF may not be very beneficial for the Si_xGe_{1-x} system under consideration.

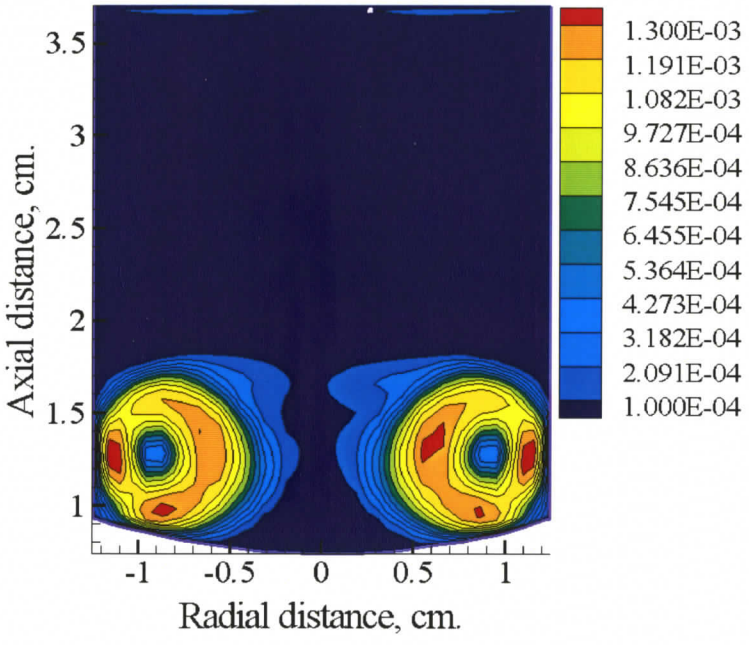

Figure 6.15- Computed flow strength ($U = \sqrt{v_x^2 + v_r^2}\ m/s$) on the vertical plane ($\varphi = \pi$) without magnetic field at t=2 h.

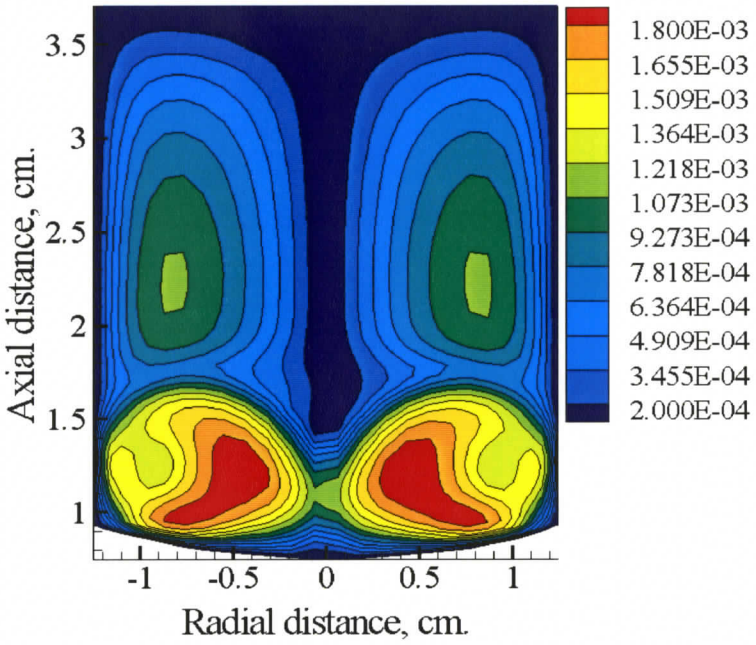

Figure 6.16- Computed flow strength ($U = \sqrt{v_x^2 + v_r^2}\ m/s$) on the vertical plane ($\varphi = \pi$) at B=0.5 mT, f=10 Hz. and t=2 h.

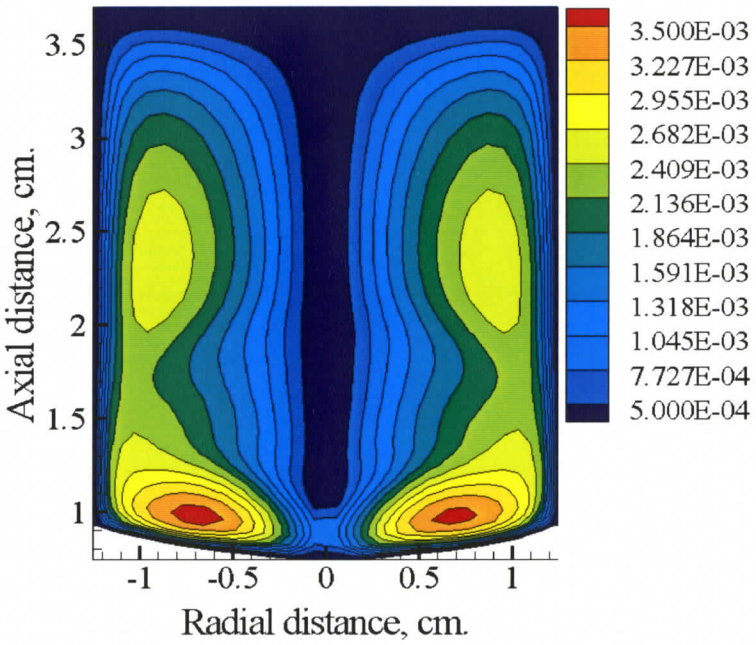

Figure 6.17- Computed flow strength ($U = \sqrt{v_x^2 + v_r^2}\ m/s$) on the vertical plane ($\varphi = \pi$) at B=1 mT, f =10 Hz and t =2 h.

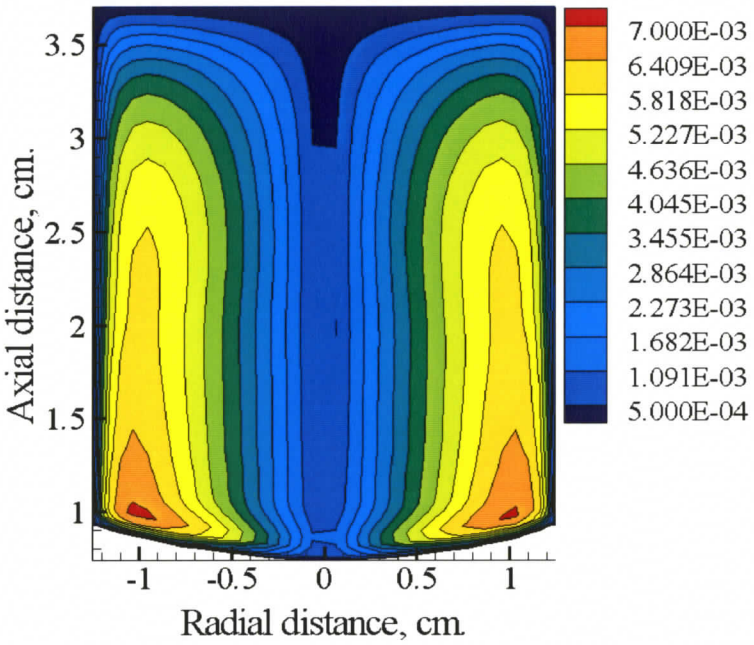

Figure 6.18- Computed flow strength ($U = \sqrt{v_x^2 + v_r^2}\ m/s$) on the vertical plane ($\varphi = \pi$) at B=2 mT, f =10Hz and t=2 h.

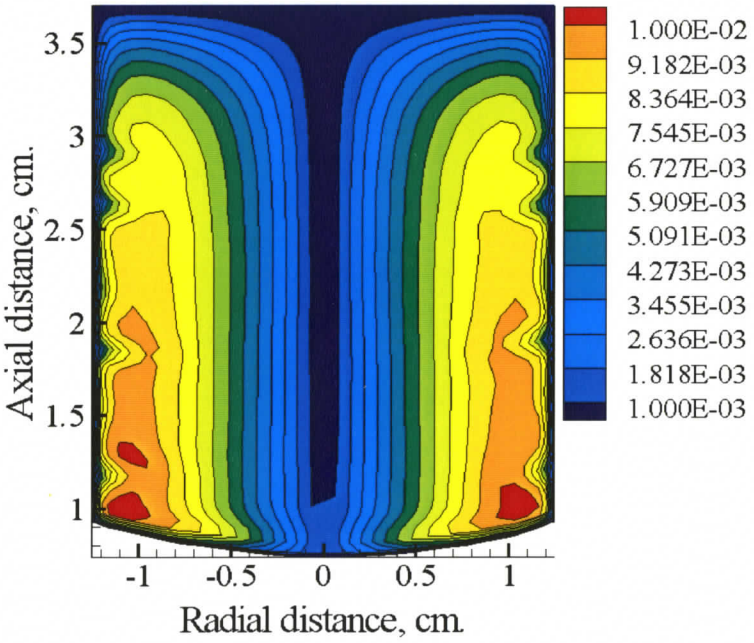

Figure 6.19- Computed flow strength ($U = \sqrt{v_x^2 + v_r^2}\ m/s$) on the vertical plane ($\varphi = \pi$) at B=3 mT, f =10Hz and t = 2h.

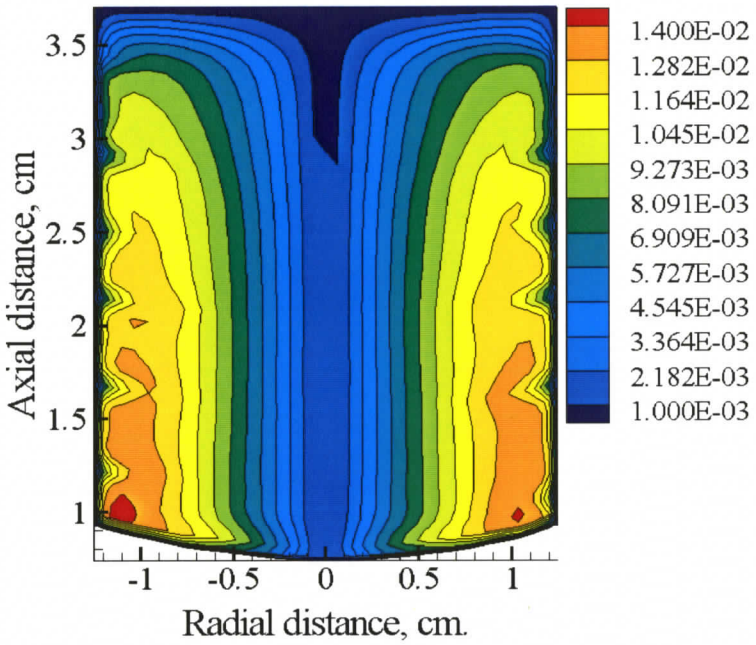

Figure 6.20- Computed flow strength ($U = \sqrt{v_x^2 + v_r^2}\ m/s$) on the vertical plane ($\varphi = \pi$) at B=4 mT, f =10 Hz and t =2 h.

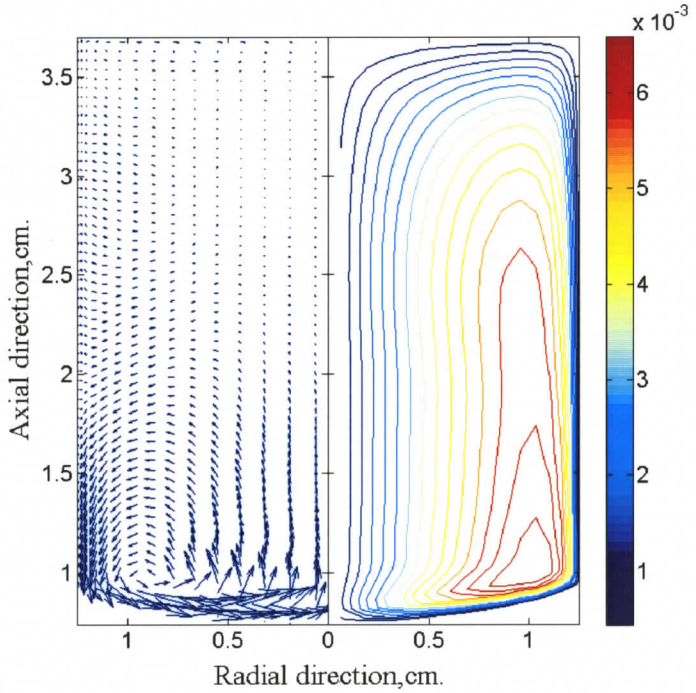

Figure 6.21- Radial-meridional velocity field vector (left) and azimuthal velocity field (right) on the vertical plane ($\varphi = \pi$) at B=2mT, f =10 Hz. and t =2h.

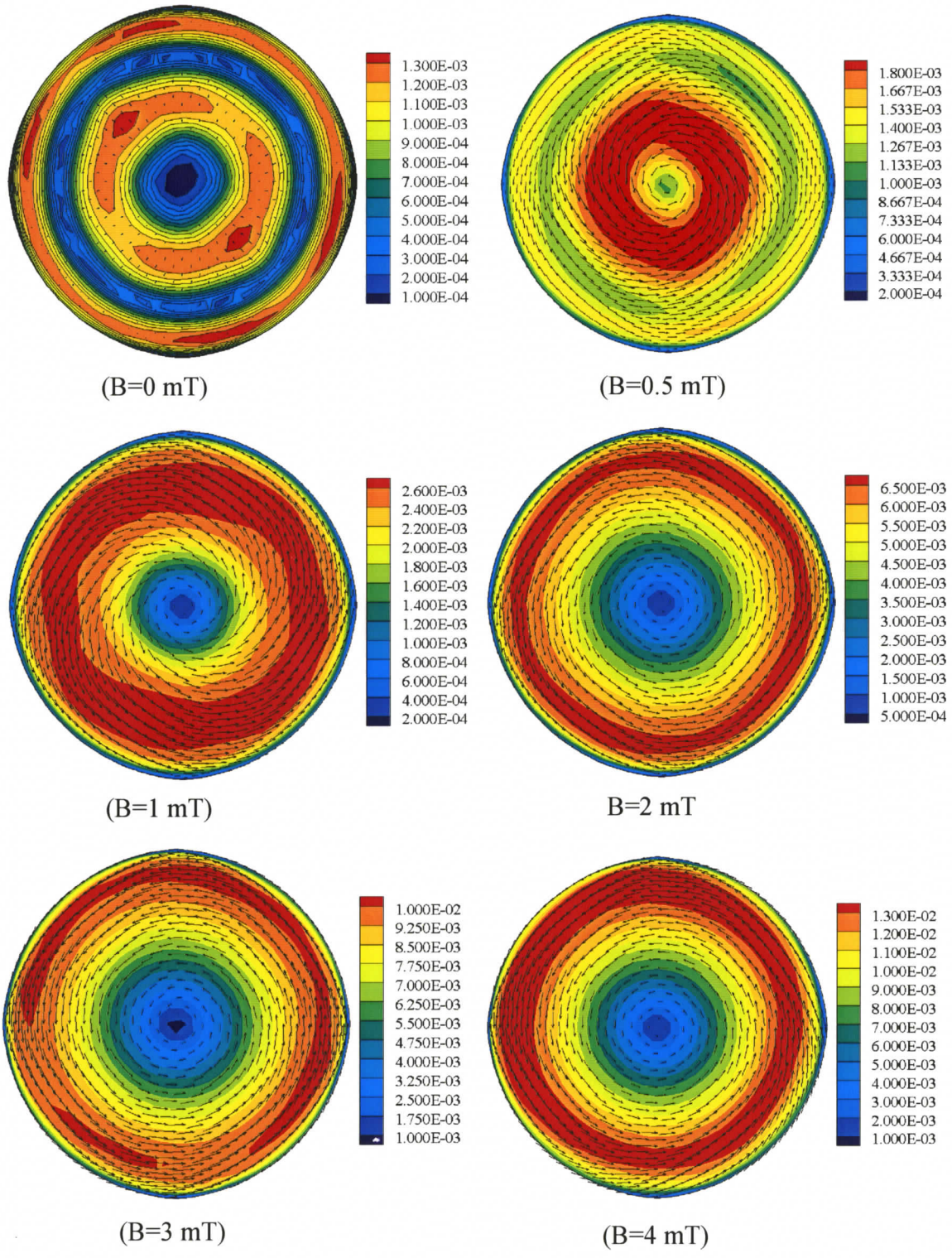

Figure 6.22-Computed flow strengths from a horizontal plane at a distance 6 mm at t =2 h. and f =10 Hz. with the application of different RMF intensities

The maximum flow strength at various RMF intensities and at three different frequency levels is plotted in Figure 6.23. This figure shows the effect of frequency of a rotating magnetic field on the flow in the solution.

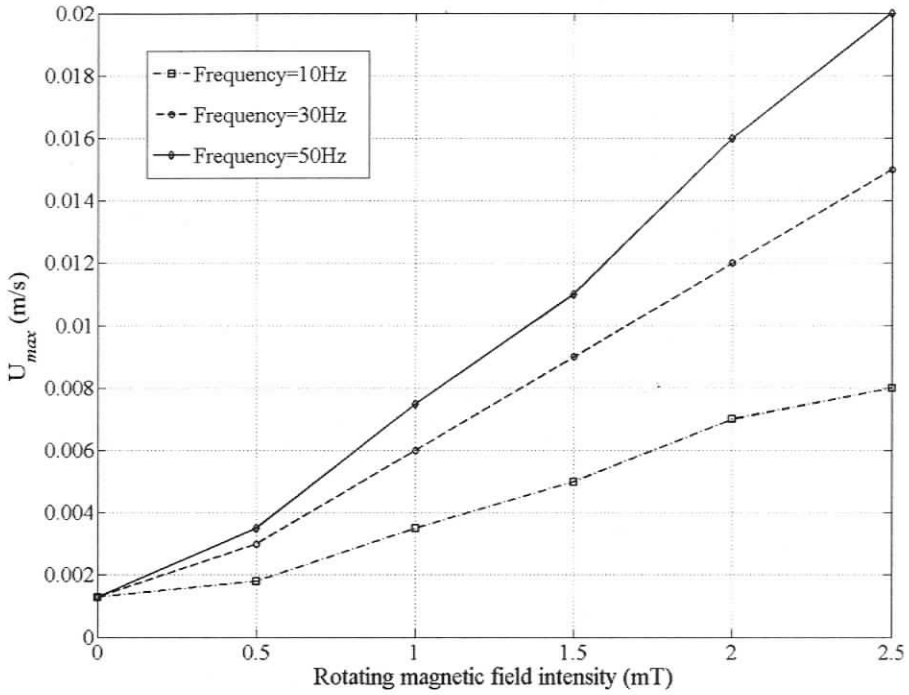

Figure 6.23- Variation of maximum flow strength with increasing rotating magnetic field intensity at different frequencies

It would be desirable to know whether the contribution of induced electric field (potential) is significant in the case of a rotating magnetic field. To answer this question, we have also computed the velocity field with and without the contribution of electric potential. Figure 6.24 and 6.25 show the computed maximum azimuthal velocity strength and flow strength at different RMF intensities with and without the contribution of electric potential. The results indicate that for the case of RMF, the contribution of electric potential to the flow field is significant, contrary to what we observed in the case of static vertical magnetic field. The error analysis shows that omitting the contribution of electric potential leads to an average error in the order of almost 14 %. This finding suggests that electric potential must be included in the analysis to obtain accurate results.

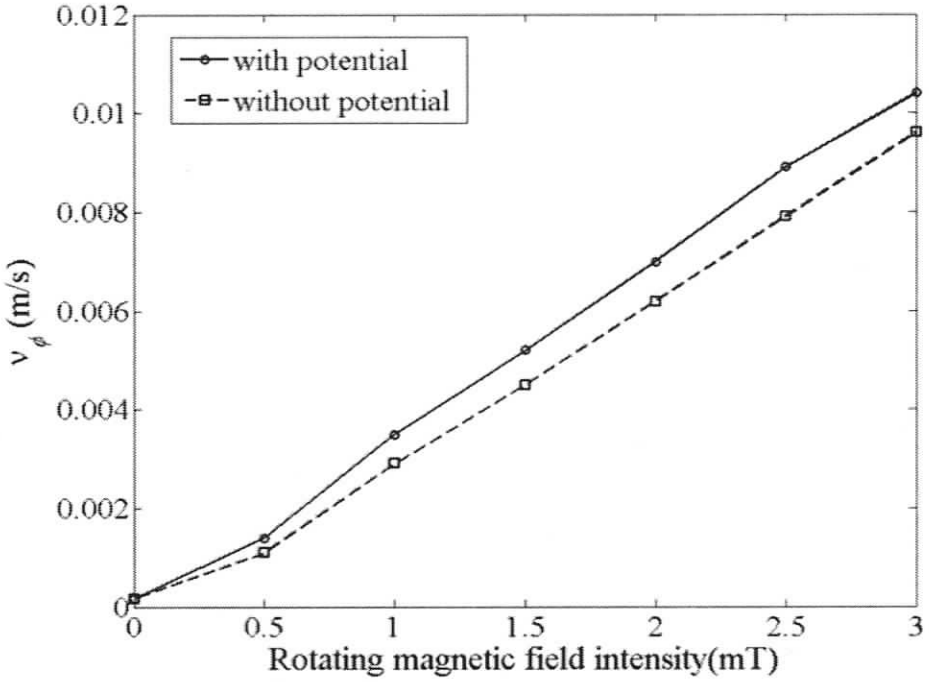

Figure 6.24- The maximum value of azimuthal velocity versus the rotating magnetic field intensity with and without electrical potential.

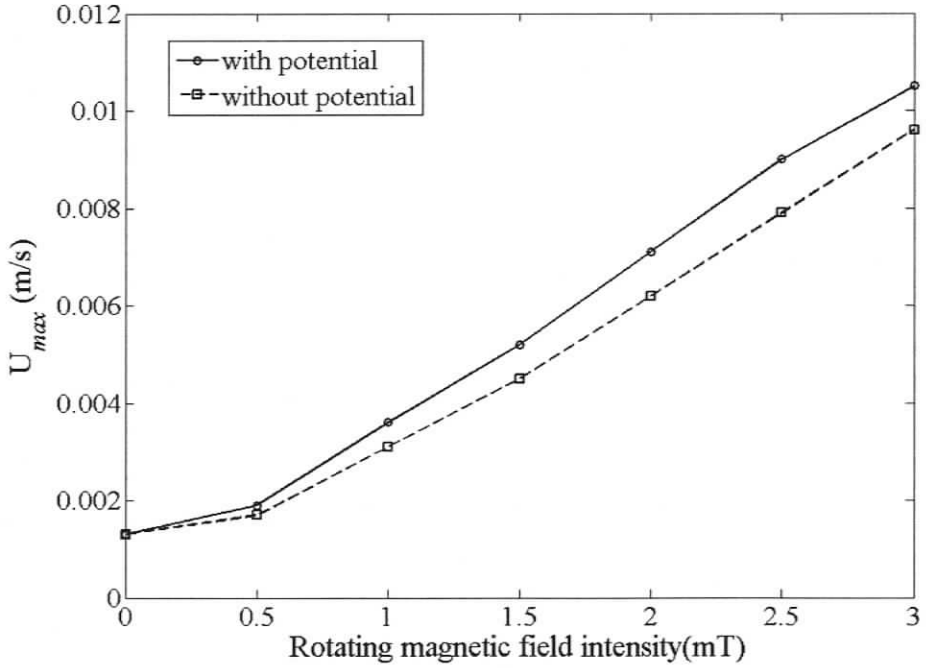

Figure 6.25- The maximum value of velocity strength versus the rotating magnetic field intensity with and without electrical potential.

6.2.2 Effect of an RMF on the Concentration Field

The concentration profile of Si in the *Si-Ge* solution during the first 2 hours of the growth at various magnetic field strengths is shown in Figures (6.27-6.31). In the absence of a rotating magnetic field, the computed concentration profiles exhibit a diffusion-like pattern throughout the liquid domain except the lower region near the interface where convection occurs (see Figure 6.26). Under a rotating magnetic field, the concentration profiles are also influenced by the force convection due to RMF as can be seen from Figures (6.27-6.31). Close examination of figures indicates that unlike static vertical magnetic field, the rotating magnetic field considerably reduces the variation of the concentration gradient normal to the growth interface along the radial direction, thereby forming uniform radial solute gradient. The computed large Schmidt number (≅5.22) supports the above results indicating that the new convection structure under the effect of applied RMF has a significant influence on the transport of the solute in the solution.

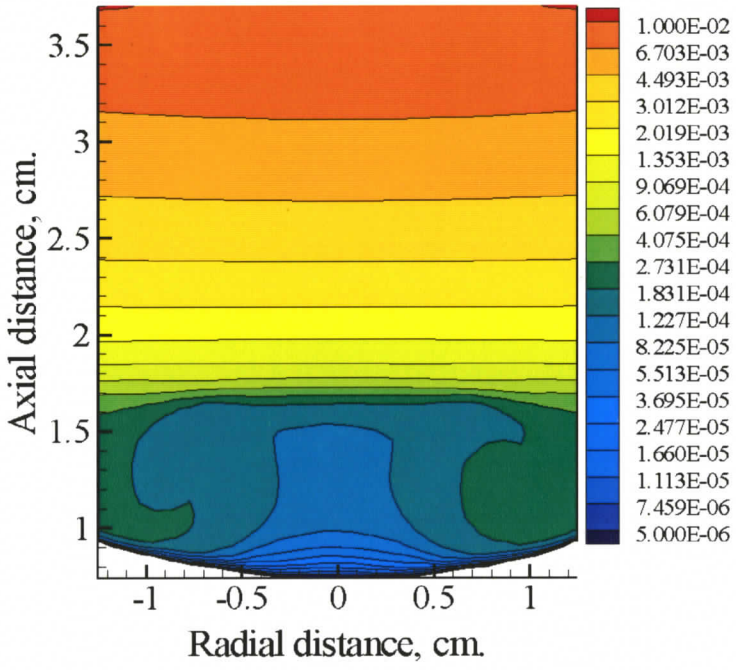

Figure 6.26- Silicon concentration distribution (in mass fraction) on the vertical plane ($\varphi = \pi$) without magnetic field at t=2h.

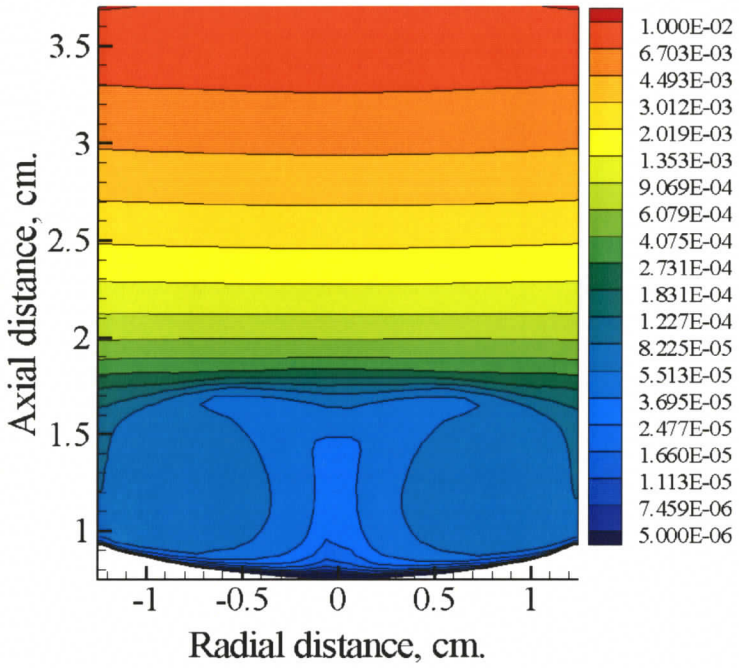

Figure 6.27- Silicon concentration distribution (in mass fraction) on the vertical plane ($\varphi = \pi$) at B= 0.5 mT, f =10 Hz and t =2 h.

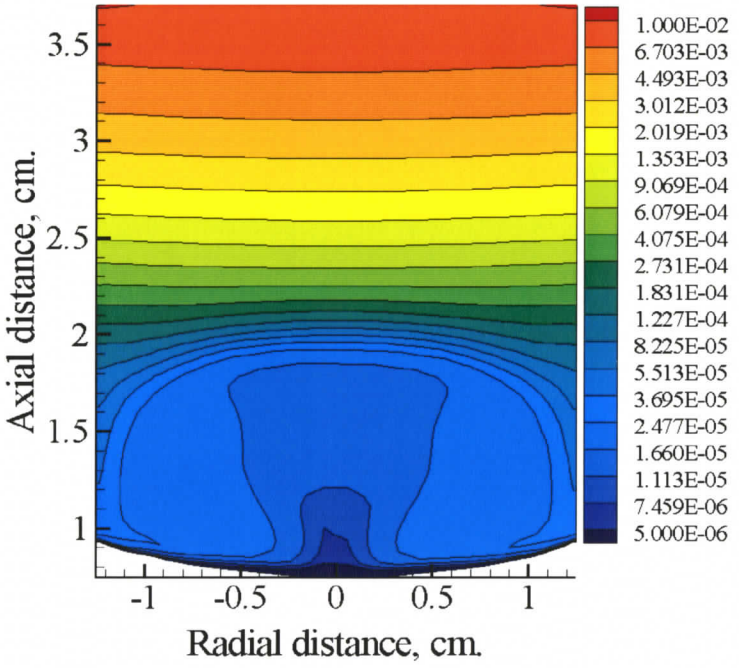

Figure 6.28- Silicon concentration distribution (in mass fraction) on the vertical plane ($\varphi = \pi$) at B= 1 mT, f =10 Hz and t =2 h.

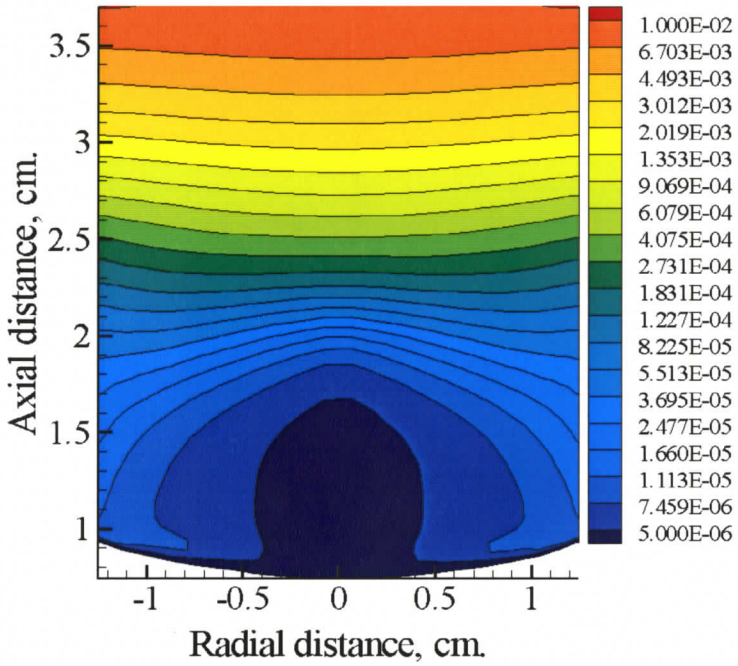

Figure 6.29- Silicon concentration distribution (in mass fraction) on the vertical plane ($\varphi = \pi$) at B= 2 mT, f =10 Hz and t =2 h.

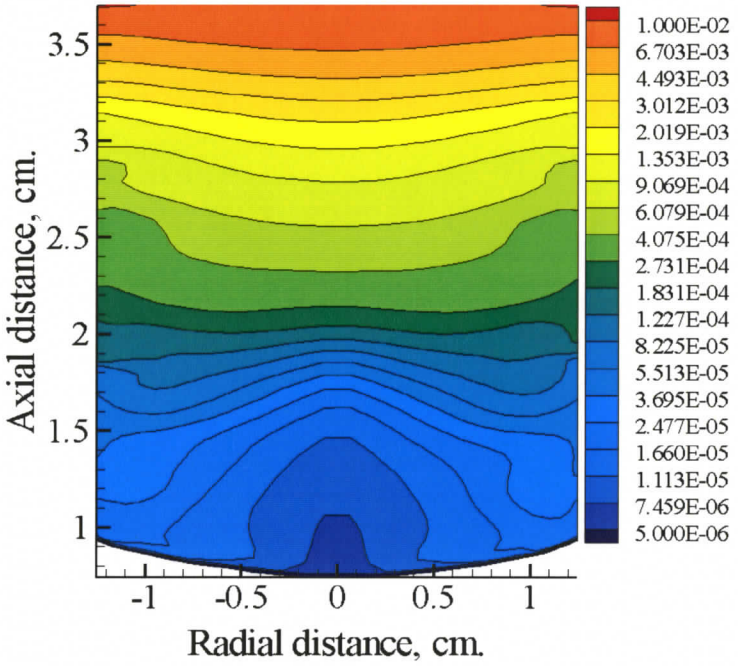

Figure 6.30- Silicon concentration distribution (in mass fraction) on the vertical plane ($\varphi = \pi$) at B=3 mT, f =10 Hz and t =2 h.

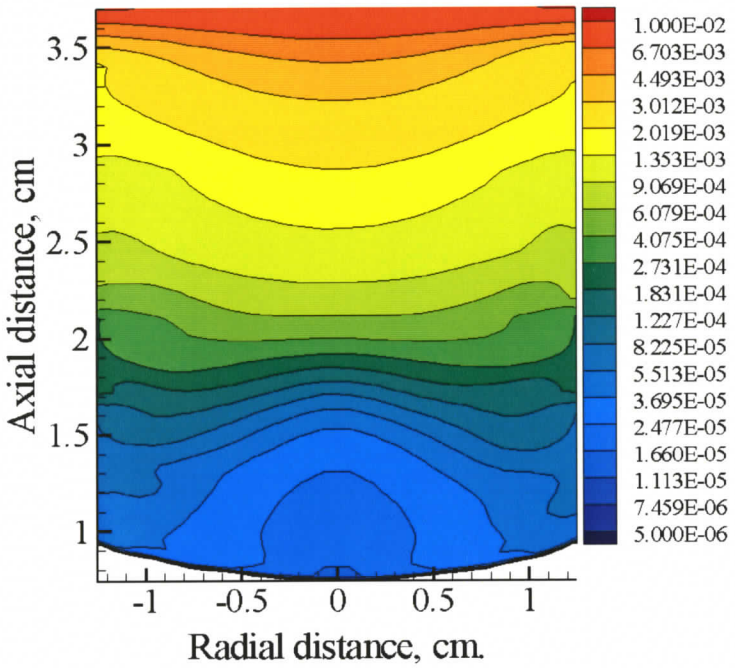

Figure 6.31- Silicon concentration distribution (in mass fraction) on the vertical plane ($\varphi = \pi$) at B=4 mT, f =10 Hz and t =2 h.

6.2.3. Effect of an RMF on the Growth Interface Shape

In crystal growth a planar growth interface shape is favorable; however, due to the flow and temperature oscillations in the liquid solution, the uniformity of the solute distribution in the radial direction is disturbed. Therefore, it is difficult to achieve a flat interface shape. The present simulation results under an applied rotating magnetic field have shown that even very small values of rotating magnetic field are sufficient to decrease the radial solute gradient (see Figure 6.32). As can be seen from figure, a field intensity of 2 and 3 mT is adequate to obtain a radially uniform solute gradient. This finding suggests RFM can improve the interface shape significantly.

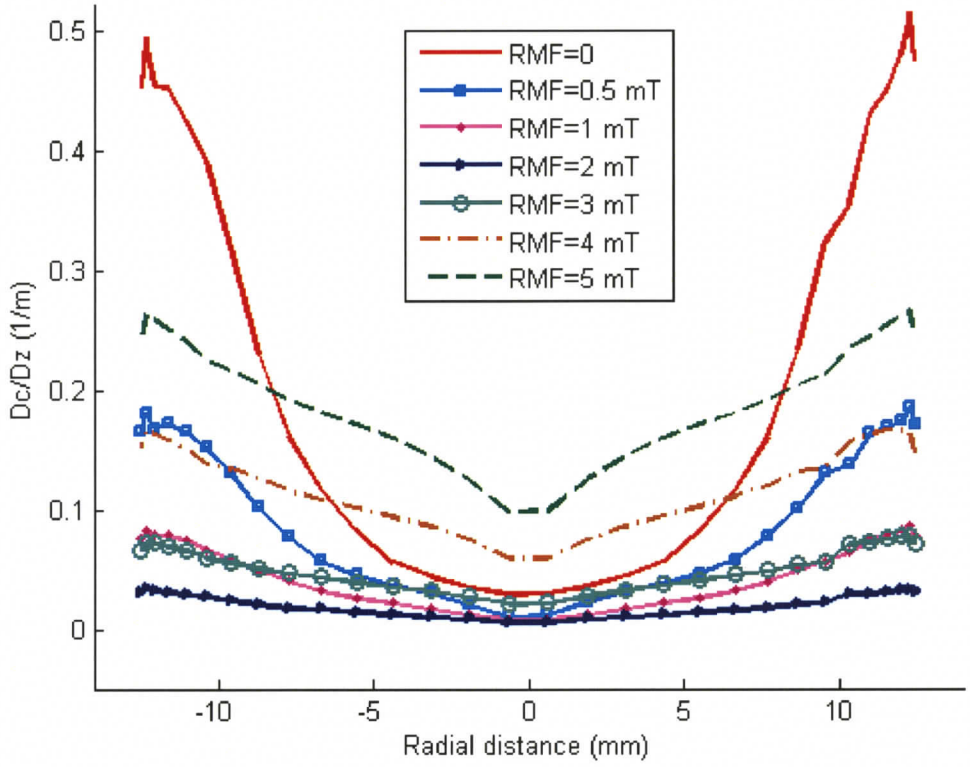

Figure 6.32- Radial variation of solute (Si) gradient in the growth direction at the growth interface with various rotating magnetic field intensities.

The radial variation of the solute distribution (radial nonuniformities) in the solution adjacent to the growth interface can also be characterized using the following formulation, $\delta c = (c_{\max} - c_{\min}) / c_{av}$ where δc, $c_{\max}$, $c_{\min}$ and c_{av} are the radial segregation, the maximum , minimum and radially- averaged interfacial concentrations, respectively. Radial segregation for different level of RMF intensities is given in Figure 6.33. With the increase of the RFM level, the decrease in the radial segregation is observed. This result indicates that the application of RMF creates the desired mixing in the solution, thus reducing the radial nonuniformities in solute distribution.

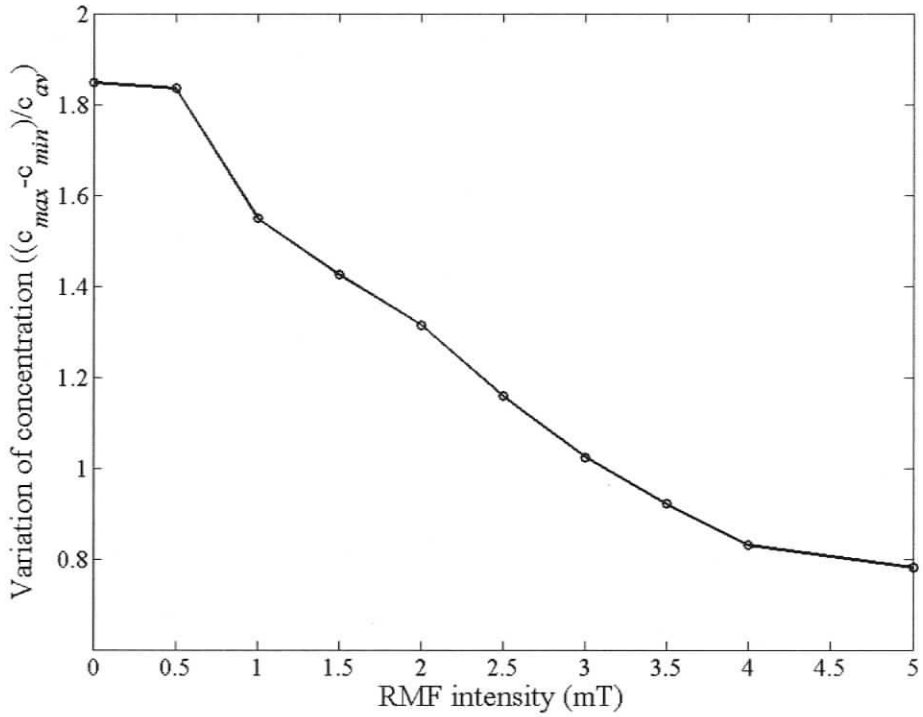

Figure 6.33- Radial segregation as a function of applied RMF intensity at 10 Hz.

CHAPTER 7

CONCLUSION

The control of fluid flow in the melt during crystal growth is very important for obtaining homogeneous concentration and temperature distribution and thus for the quality of crystals. For decades, different types of magnetic fields have been used to provide an effective means to control the flow field in the melt during crystal growth. For instance, a static vertical magnetic field gives rise to a Lorentz force that suppresses convection while a rotating magnetic field induces a Lorentz force that generates a stirring action and homogenizes the melt. These favorable effects of magnetic fields in crystal growth have led to the improvement of growth processes and consequently the quality of the grown crystals.

The primary objective of this thesis was to investigate the feasibility of using static vertical and rotating magnetic fields in the LPD growth of $Si_x\ Ge_{1-x}$ single crystals. The second goal was to find the appropriate magnetic field type and induction value to improve the LPD growth process conditions for better quality $Si_x\ Ge_{1-x}$ crystals. To this end, a three-dimensional numerical simulation study was conducted to examine the influence of a static vertical and rotating magnetic field on the fluid flow and, heat and mass transfer characteristics in the *Si-Ge* liquid solution. The numerical simulation results for the flow and concentration fields in the liquid domain helped us understand the physical phenomena taking place during the early hours of the growth of $Si_x\ Ge_{1-x}$ single crystals by LPD under static vertical and rotating magnetic fields. Results showed that vertical magnetic field suppresses convection but it is not effective in flattening the growth interface. A rotating magnetic field on the other hand is very effective in providing mixing in the solution for uniform mass transport.

The specific results can be summarized as follows;

1. The use of a static vertical magnetic field with the intensity up to 0.3 T was found to be very beneficial for suppressing the convection; yet it was not effective in flattening the growth interface.

2. A Rotating magnetic field is effective in providing mixing up to a critical field intensity of about 3.0 mT. Over this critical value, the computed flow field was unstable. At about this critical value, the growth interface changes its shape from concave to almost flat.

3. Depending on the outcomes of the present study, RMF intensity levels between 2.0 and 3.0 mT can be suggested as the optimum values for the $Si_x\ Ge_{1-x}$ system.

7.1 Contributions

In the course of this study, a 3D transient theoretical model for the simulation of $Si_x\ Ge_{1-x}$ growth by LPD under static and rotating magnetic fields was developed. The outcome of the present study is significant in terms of suggesting a framework for the future experimental studies on the growth of $Si_x\ Ge_{1-x}$ by the LPD technique. This work is also original due to being the first detailed study which considers the application of magnetic fields in LPD growth of $Si_x\ Ge_{1-x}$ single crystals. It also shows the importance of the contribution of electrical potentials to the LPD growth process for accurate predictions.

7.2 Recommendations for Future Works

In the light of the results presented in this thesis we suggest that the experimental study for the growth of $Si_x\ Ge_{1-x}$ single crystals by LPD under rotating magnetic field intensities of 2-3 mT should be performed to improve the quality of $Si_x\ Ge_{1-x}$ single crystals.

Development of a user defined FORTRAN subroutine to move the growth interface in time for modeling the interface evolution is in progress. However, this part of the study requires long computation time due to the nature of 3D modeling and the long growth process. Therefore, the results are not included in this thesis. In this direction, completion of the interface movement is left for future work.

BIBLIOGRAPHY

[1] D. J. Paul, "Silicon germanium heterostructures in electronics:- the present and the future," *Thin solid films*, vol.321, pp.172-180, 1998.

[2] M. Jutsi, and M. Berroth, "SiGe- based photodetectors for optical communications," *Properties of Silicon Germanium and SiGe: carbon*, edited by Eric Kasper and Klara Lyutovich, p.342, 2000.

[3] G. Bremond, A. Daami, A. Laugier, W. Seifert, M. Kittler and et al., " *SiGe* thin films structures for solar cells," *Mat. Res. Soc. Symp. Proc.,* vol.485, pp.43-48,1998.

[4] Y. H. Luo, J. Wan, R. L. Forrest, J. L. Liu, M. S. Goorsky and K. L. Wang, " High quality strained- relaxed *SiGe* films grown with low temperature Si buffer,' *Journal of applied Physics*, vol. 89, pp.8279-8283, 2001.

[5] M. I. Alanso, and E. Bauser, "Growth of Si_{1-x} Ge_x on silicon by Liquid-Phase Epitaxy, *Journal of applied Physics*, vol. 62, pp.4445-4449,1987.

[6] P. Bhattarcharya, J. Singh, and E. Gularl, " Epitaxial growth and characterization of Si_{1-x} Ge_x materials and devices," *Final Technical report*, October 15, 1994-October 14, 1997, Solid State Electronic Laboratory, Department of electrical engineering and computer science, The university of Michigan, December 26, 1997.

[7] Yildiz. M. "A Combined experimental and modeling study for the growth of *SiGe* single crystals by Liquid Phase Diffusion", PhD Thesis, University of Victoria, 2005

[8] M. Yildiz, S. Dost, B. Lent, "Growth of bulk *SiGe* single crystals by Liquid Phase Diffusion", Journal of Crystal Growth, vol. 280 pp.151-160, 2005.

[9] K.W. Benz and P. Dold, "Crystal growth under microgravity: present results and future prospects towards the International Space Station," *Journal of Crystal growth*, vol. 237-239, pp.1638-1645, 2002.

[10] H. Wiedemeier, Y.-R. Ge, M. A Huthcins, "Effect of microgravity on $Hg_{1-x}Cd_xTe$/(1 0 0) CdTe epitaxy by CVT under transient growth conditions," vol. 187, pp.72-80,1998.

[11] B. Lent, S. Dost, R.F. Redden, Y. Liu, "Mathematical simulation of the traveling heater method growth of ternary semiconductor materials under suppressed gravity conditions", *Journal of Crystal Growth,* vol. 237-239, pp. 1876-1880, 2002.

[12] P.A. Davidson, "Magnetohydrodynamics in material processing", *Annual Review of Fluid Mechanics,* vol. 31, pp. 273-300, 1999.

[13] D. Vizman, B Fisher, "3D numerical simulation of melt flow in the presence of a rotating magnetic field", *International Journal of Numerical Methods for Heat and Fluid Flow*, vol. 10, pp. 366-384, 2000.

[14] Handbook of Crystal Growth 2, *Bulk Crystal Growth, part B: Growth mechanism and dynamics,* edited by D. T. J. Hurle,Elsevier Science B.V. Amsterdam, 1994.

[15] N. Ma, J. S. Walker, "A parametric study of segregation effects during vertical Bridgman crystal growth with an axial magnetic field", *Journal of Crystal Growth*, vol. 208, pp. 757-771, 2000.

[16] J.S. Walker, "Bridgman crystal growth with a strong, low frequency, rotating magnetic field", *Journal of Crystal Growth,* vol.192, pp.318-327, 1998.

[17] Th. Duffor, C. Stelian, A.Mitric, "Effect of magnetic field in Bridgman growth of semiconductor alloys", *International Scientific Colloquium*, Hannover, march 24-26, 2003.

[18] K. H. Spitzer, Application of rotating magnetic fields in Czochralski crystal growth, *Progress in Crystal Growth and Characterization of Materials,* pp. 39-58, 1999.

[19] N. G. Ivanov, A. B. Korsakov, E. M. Smirnov, K. V. Khodosevitch, V. V. Kalaev, Yu. N. Makarov, E. Dornberger, J. Virbulis, W. von Ammon, "Analysis of magnetic field effect on 3D melt flow in CZ Si growth", *Journal of Crystal Growth,* vol.250, pp. 183-188, 2003.

[20] J. Virbulis, Th. Wetzel, A Muiznieks, B. Hanna, E. Dornberger, E. Tomzig, A. Muhlbauer, W. v. Ammon, " Numerical investigation of silicon melt flow in large diameter Cz-crsytal growth under the influence of steady and dynamic magnetic fields", *Journal of Crystal Growth*, vol. 230, pp.92-99, 2001.

[21] K. Kakimoto, "Effect of rotating magnetic fields on temperature and oxygen distributions in silicon melt", *Journal of Crystal growth*, vol. 237-239, pp. 1785-1790, 2002.

[22] J. S. Walker, L. M. Witkowski, B. C. Hounchens, "Effects of a rotating magnetic field on the thermocapillary instability in the floating zone process", *Journal of Crystal Growth*, vol. 252, pp. 413-423, 2003

[23] P. Dold, A.Croll, M. Lichtensteiger, Th. Kaiser, and K. W. Benz, "Floating zone growth of silicon in magnetic fields: IV. Rotating magnetic fields", *Journal of Crystal Growth,* vol. 231, pp. 95-106, 2001.

[24] N. Ma, J. S. Walker, A. Ludge, H. Riemann, " Combining a rotating magnetic field and crystal rotation in the floating zone process with needle-eye induction coil", *Journal of Crystal Growth*, vol. 230, pp. 118-124, 2001.

[25] Handbook of Crystal Growth 3, *Thin Films and Epitaxy, Part A: Basic Techniques,* edited by D. T. J. pp. 225-252, Hurle,Elsevier Science B.V. Amsterdam, 1994.

[26] Y. Inatomi, K. Horiuchi, A. Kato and K. Kuribayashi, "Growth kinetics of GaP in LPE", *Journal of Crystal Growth,* vol. 237-239, pp. 1428-1433, 2002.

[27] H. Sheibani, Y. Liu, S. Sakai, B. Lent, S. Dost, "The effect of applied magnetic field on the growth mechanism of liquid phase Electroepitaxy", *International Journal of. Engineering and Science,* vol. 41, pp.401-415, 2003.

[28] S. Dost, Y. Liu, B. Lent, "A numerical study for the effect of applied magnetic field in liquid phase electroepitaxy", Journal of Crystal Growth, vol. 240, pp. 39-51, 2002.

[29] Y. C. Liu, Y. Okano, S. Dost, "The effect of magnetic field on the flow structures in Liquid Phase Electroepitaxy- a three-dimensional simulation model", *Journal of Crystal Growth*, vol. 244, pp. 12-26, 2002.

[30] S. Dost, Y. Liu, B. Lent and R. F. Redden, "A numerical simulation study for the effect of applied magnetic field in the growth of *CdTe* single crystal by the travelling heater method", *International Journal of Applied Electromagnetics and Mechanics,* vol. 17, pp.271-288, 2003.

[31] Y. Wang, K. Kudo, Y. Inatomi, R. Ji, T. Motegi, " Growth and structure of CdZnTe crystals from Te solution with THM technique under static magnetic field", *Journal of Crystal Growth*, vol. 275, pp. el551-el556, 2005.

[32] C. K. Ghaddar, C. K. Lee, S. Motakef, D. C. Gillies, Numerical simulation of THM growth of CdTe in presence of rotating magnetic fields (RMF), *Journal of Crystal Growth*, vol. 205, pp. 97-111, 1999.

[33] C. Stelian, Y. Delannoy, Y. Fautrelle, T. Duffar, "Solute segregation in directional solidification of GaInSb concentrated alloys under alternating magnetic field", *Journal of Crystal Growth*, vol. 266, pp. 207-215, 2004

[34] J. Virbulis, Th. Wetzel, A Muiznieks, B. Hanna, E. Dornberger, E. Tomzig, A. Muhlbauer, W. v. Ammon, " Numerical investigation of silicon melt flow in large diameter Cz-crsytal growth under the influence of steady and dynamic magnetic fields", *Journal of Crystal Growth*, vol. 230, pp.92-99, 2001.

[35] L. Gorbunov, A. Klyukin, A, Pedchenko, A. Feodorov, "Melt flow instability and vortex structures in Czochralski growth under steady magnetic field", *Energy Conversion &Management*, vol. 43, pp. 317-326, 2002.

[36] Yu. M. Gelfgat, " Rotating magnetic field as means to control the hydrodynamics and heat/ mass transfer in the processes of bulk single crystal growth", *Journal of Crystal Growth*, vol. 198/199, pp. 165-169, 1999.

[37] I. V. Barmin, A. S. Senchenkov, I. Ch. Avetisov, E.V. Zharikov, "Low-energy methods of mass transfer control at crystal growth", *Journal of Crystal Growth*, vol. 275, pp. el1487-el1493, 2005.

[38] O. Patzold , I. Grants, U. Wanderwald, K. Jenkner, A. Croll, G. Gerbeth, "Vertical gradient freeze growth of GaAs with rotating magnetic field", *Journal of Crystal Growth,* vol.245, pp. 237-246, 2002.

[39] Th. Duffor, C. Stelian, A.Mitric, "Effect of magnetic field in Bridgman growth of semiconductor alloys", *International Scientific Colloquium*, Hannover, March 24-26, 2003.

[40] K. Kakimoto, "Effect of rotating magnetic fields on temperature and oxygen distributions in silicon melt", *Journal of Crystal growth*, vol. 237-239, pp. 1785-1790, 2002.

[41] M Yildiz, "A continuum model for the Liquid Phase Diffusion growth of bulk SiGe single crystals", *International Journal of Engineering Science,* vol. 43, pp.1059-1080, 2005

[42] Y. C. Liu, S. Dost, H. Sheibani, " A Three Dimensional Numerical Simulation for the Transport Structures in Liquid Phase Electroepitaxy Under Applied Magnetic Field ", *International journal of Transport Phenomena,*vol.6, pp.51-62, 2004.

[43] Kenneth R. Cramer, shih-l Pai, "Magnetofluid Dynamics for Engineers and Applied Physicists", Scripta Publishing Company, Washington D.C., 1973.

[44] J. A. Shercliff, "A textbook of Magnetohydrodynamics", Pergemon Press Ltd., Oxford , 1965.

[45] Rene Moreau, "The Fundamentals of MHD related crystal growth", *Progress in Crystal Growth and Characterization of Materials*, vol.38, pp.161-194, 1999.

[46] CFX 4.4 Flow solver User guide, computational fluid dynamics services, United Kingdom, 1995.